Instrument Proposal of the
Swiss-Danish Instrumentation Consortium
for the European Spallation Source, ESS

Estia

Εστία

a

focusing reflectometer for small samples

based on the

Selene guide concept

March 31, 2014

ESS Swiss-Danish instrumentation consortium

PAUL SCHERRER INSTITUT PSI

UNIVERSITY OF COPENHAGEN

project team

Jochen Stahn	Laboratory for Neutron Scattering Paul Scherrer Institut Switzerland jochen.stahn@psi.ch +41 56 310 2518	senior scientist - project leader - concept - experiements - McStas
Panagiotis Korelis	Laboratory for Neutron Scattering Paul Scherrer Institut Switzerland panagiotis.korelis@psi.ch +41 56 310 5813	post-doc - McStas - experiments
Uwe Filges	Laboratory for Developments and Methods Paul Scherrer Institut Switzerland uwe.filges@psi.ch +41 56 310 4606	senior scientist - McStas, MCNPX
Tobias Panzner	Laboratory for Neutron Scattering Paul Scherrer Institut Switzerland tobias.panzner@psi.ch +41 56 310 4342	scientist - McStas - experiements
Emmanouela Rantsiou	Laboratory for Developments and Methods Paul Scherrer Institut Switzerland emmanouela.rantsiou@psi.ch +41 56 310 4631	scientist - McStas, MCNPX
Marité Cardenas	Nano-Science Center University of Copenhagen Denmark cardenas@nano.ku.dk +45 35 320 431	senior scientist - scientific advice
Ursula Bengaard Hansen	Nano-Science Center University of Copenhagen Denmark uhansen@fys.ku.dk +45 60 478 615 (mobile)	student assistant - McStas - experiements
Beate Klösgen	Department for Physics, Chemistry and Pharmacy University of Southern Denmark Denmark kloesgen@sdu.dk +45 6550 2561	associate professor - scientific advice

Selene

moon, dark side

titan goddess

detail of the ceiling painting
Selene and Endymion
at the
Ny Carlsberg Glyptotek, Copenhagen

Executive summary

Estia — a focusing reflectometer for small samples

The *Swiss-Danish ESS instrumentation consortium* presents *Estia*[1], a focusing reflectometer optimised for small samples. The combination of the high brilliance of the ESS with a truly focusing neutron guide system results in a performance gain of up to two orders of magnitude compared to state-of-the-art reflectometers.

Scientific field Scientific areas of interest for reflectometry include the investigation of novel phenomena resulting from the forced coexistence of conflicting properties on an atomic scale in nanostructures, and the understanding of biological mechanisms at cell membranes. On the technological side there is the improvement of magnetic data storage and processing, and of protective or functional coatings. The resulting variety in sample size, geometry, measurement-range and resolution leads to competing optimisation criteria for a reflectometer.

The scientific focus of *Estia* is the investigation of structural and magnetic depth profiles of solid film structures. But the optimisation for small samples also enables very efficient probing of liquid/solid interfaces in microfluidic chambers, or the determination of lateral correlations. To accommodate the large demand for reflectometry and the diversity of research fields, *Estia* should be complemented by a reflectometer optimised for liquid surfaces and organic samples in general, and possibly another instrument dedicated to high-resolution investigations of lateral structures.

A selection of special and very active areas of research that will profit greatly from *Estia* is:

- The investigation of magnetic heterostructures. These are the basic building blocks for a large number of magneto-electric devices, and increasingly for sensors and switches.
- Time-resolved studies of processes at solid surfaces, such as polymerisation or self-assembly of organic components.
- Multifunctional materials, combining and linking magnetic, electronic and mechanical properties. While the coupling observed so far in bulk is rather weak, the combination of materials coupled via an interface opens a wide and promising field of research and applications.
- Novel electronic phases: Insulating metal-oxide heterostructures that develop mobile electron gases at the interfaces, and which show a rich spectrum of physical properties.
- Processes on functionalised surfaces, e.g. to improve the biocompatibility of scaffolds for bone tissues.
- Diffusion and selfdiffusion of atoms in solids. These play a key role for the design and optimisation of materials as well as for the performance of devices in various branches of technology like energy storage/conversion, electronic devices, sensor technology and design of nanostructured materials.

The performance gain offered by *Estia* will allow a number of breakthroughs in all these areas very soon after start of operation of the ESS.

Selene guide concept The centrepiece of *Estia* is its truly focusing neutron guide, based on the *Selene* concept.[1] A *Selene* guide transports only the useful neutrons, and enables beam manipulation similar to a photographic lens. In optics, point-to-point focusing allows us to define the image size with a lumination field diaphragm located at the initial focal point (here called *virtual source*). The divergence of the beam is controlled by an aperture behind the optical lens, far from the image.

For neutrons the lens has to be replaced by a reflecting device, here a planar-elliptic mirror. Like all focusing optical devices this suffers from aberration, which is largest in this case for reflections close to the focal points. Avoidance of these regions and compensation of the coma aberration by a second, identical reflector results in the optical path as sketched on the right for the vertical plane (red: reflectors, gold: beam). Applied also in the horizontal plane this leads to a device as illustrated in the 3D graphics.

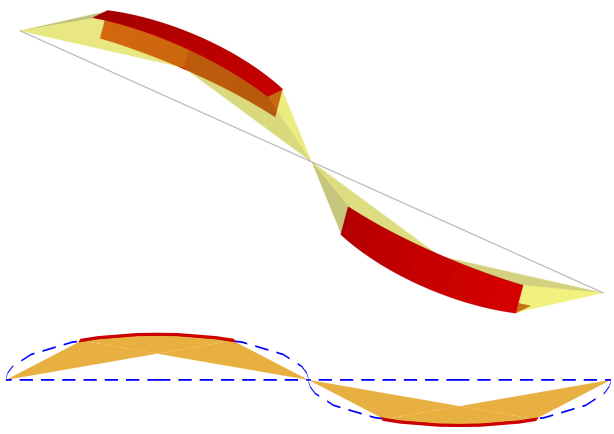

The *Selene* guide is truly focusing in a sense that the phase space density is zero outside a

volume defined by the virtual source and the aperture. Thus the beam footprint on the sample can be tuned and over-illumination can be avoided. This is in contrast to all other elliptic guides discussed nowadays, which suffer from strong coma aberration effects leading to multiple reflections and thus to poor focusing.[2, 3] Also compared to these, the total beam intensity in the *Selene* guide is it drastically reduced, which results in a low background.

The special guide geometry allows for efficient optics to polarise and filter the beam, or to implement constant resolution without using pulse shaping choppers. The convergent beam can be used efficiently on sample surfaces from $1 \times 1\,\mathrm{mm}^2$ to $50 \times 10\,\mathrm{mm}^2$. To allow for high detector angles and to reduce the influence of gravity, the scattering plane of *Estia* is horizontal.

A prototype of the *Selene* guide with a total length of 4 m was built and tested sucessfully at PSI. It is now used to reduce the measuring time on tiny samples (width below 2 mm) by up to two orders of magnitude. It proofs the predicted performance and confirms that it is possible to build and align such a high-precision guide.

Operation modes *Estia* provides several operation modes, where switching from one to the other implies only the insertion of some optical component or the activation of an aperture.

The graph on the right shows the wavelength-angle (λ-θ) space covered within one neutron pulse. The corresponding momentum transfer q_z is encoded by colour. The blue box marks the region used in conventional time-of-flight neutron reflectometry, which is the same as that used on *Estia* in its *almost conventional* mode. This is realised with a divergence-defining aperture behind the *Selene* guide end.

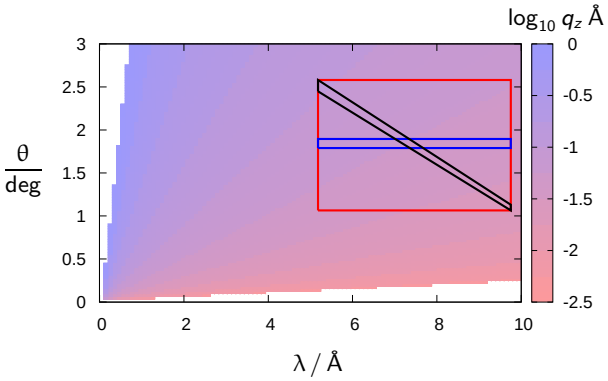

If this aperture is scanned across the beam during the pulse, the region within the black frame is measured, which results in a wider q_z-range. At the same time λ is encoded in θ which opens the possibility to control the resolution without pulse-shaping choppers.

By opening the aperture completely the region framed in red is accessible. This means an increase in the intensity incident on the sample by an order of magnitude. For this *high-intensity mode* (and only for this) off-specular reflectivity can not be measured. But it is possible to investigate dynamic processes on a split-second time-scale, or to track the influence of external conditions e.g. on magnetic properties.

Further options include the generation of a beam focused to the detector, e.g. for GISANS experiments, or the addition of spin echo techniques. The instrument will have a full polarisation and polarisation analysis option. It will be able to host heavy and bulky sample environment, and accept high magnetic fields.

Summary

The combination of the high-brilliance ESS source and the novel *Selene* guide concept, transferring as much of this brilliance as possible to the sample in a fully controlled way, will result in a high-performance reflectometer with outstanding efficiency for small samples. *Estia* uses the full unchopped long pulse provided by the ESS. The gain in comparison to a similar instrument at a continuous source with the same average power is thus a factor 30.
For samples with a width of 10 mm or less this is also the gain factor compared to current state-of-the-art reflectometers. With the high-intensity mode a reduction of measurement time relative to those of more than two orders of magnitude is possible. This extends specular reflectometry to samples with area below $1\,\mathrm{mm}^2$, or to time-resolved measurements on the spilt-second time scale.

[1] *Estia* = Εστία is the Greek goddess of the hearth (Latin *focus*), the family, and architecture. In modern Greek the word means *point of interest or importance* and is used for example when adjusting a telescope or a camera lens.

Contents

Executive summary **III**

Instrument Proposal 1

1 Scientific Case **1**

1.1 Sample size . . . 2
1.2 Measurement time . . . 3
1.3 Resolution . . . 5
1.4 Laterally structured films . . . 6
1.5 Polarisation . . . 7
1.6 Overlap with the liquids reflectometer . . . 8
1.7 Infrastructure & support facilities . . . 8

2 Description of Instrument Concept and Performance **9**

2.1 *Selene* guide . . . 10
2.2 Instrument lay-out . . . 12
2.3 Energy- and time-range . . . 14
2.3.1 Flux and λ_{min} . . . 14
2.3.2 Time regime and λ_{max} . . . 14
2.3.3 Intrinsic λ-resolution . . . 15
2.3.4 Frame-overlap suppression . . . 15
2.3.5 Choppers . . . 15
2.4 Beam manipulation . . . 15
2.4.1 Footprint definition (beam size) . . . 15
2.4.2 Divergence definition and scanning aperture . . . 16
2.4.3 Spin polarisation . . . 16
2.5 Sample stage . . . 17
2.6 Detector . . . 17
2.6.1 Area detector . . . 17
2.6.2 Single detector . . . 18
2.6.3 CCD camera . . . 18
2.7 Shielding . . . 18
2.7.1 Beam extraction . . . 18
2.7.2 First guide section: common and individual instrument shielding . . . 19

2.7.3 Apertures within guides . . . 19
2.7.4 Shutter . . . 19
2.7.5 MCNPX simulations . . . 19
2.8 Operation modes . . . 20
2.8.1 Almost conventional & off-specular reflectivity . . . 20
2.8.2 Angle-energy-encoding . . . 21
2.8.3 High-intensity specular reflectometry . . . 22
2.8.4 Comparison . . . 23
2.8.5 Further options . . . 24
2.9 Simulations . . . 25
2.10 Performance . . . 25
2.11 Design options . . . 27

3 Technical Maturity 29
3.1 Guide system . . . 29
3.2 Optical components, polarisation . . . 30
3.3 Mechanics, sample stage . . . 30
3.4 Scanning aperture . . . 30
3.5 Detector . . . 31
3.6 Computing, data analysis . . . 31

4 Costing 33
4.1 Guide system . . . 34
4.2 Optical components . . . 34
4.3 Chopper / scanning aperture . . . 34
4.4 Mechanics / motion control . . . 34
4.5 Detectors . . . 35
4.6 Shielding . . . 35

Appendices 37

5 List of Abbreviations and Nomenclature 39

6 The Selene Guide System 41
6.1 Geometrical considerations for an elliptic reflector . . . 42
6.2 Angular acceptance . . . 45
6.3 Coma aberration — and correction . . . 45
6.4 Chromatic aberration due to gravity . . . 48
6.5 Transmission . . . 50

7 Optics and Beam Shaping 53
7.1 Frame-overlap and polarisation filter . . . 53
7.2 Condenser . . . 55
7.3 Tele- or wide-angle optics . . . 56

8 Boundary Conditions and Consequences 59

8.1 Space . . . 59

8.2 Shielding and background . . . 60

8.3 Exclusion of proton prompt . . . 60

8.3.1 Intrinsic resolution . . . 60

9 Technical Details 63

9.1 Moving elements . . . 63

9.2 Detector characteristics . . . 64

9.2.1 Cross-talk . . . 65

10 Measurement Schemes and Data Reduction 67

10.1 General aspects . . . 67

10.1.1 Sample alignment . . . 67

10.1.2 Normalisation and reference measurement . . . 67

10.1.3 Data reduction . . . 68

10.2 Almost conventional reflectometry . . . 70

10.2.1 Data acquisition . . . 70

10.2.2 Discussion . . . 71

10.3 λ-θ-encoding reflectometry . . . 71

10.3.1 Data acquisition . . . 72

10.3.2 Normalisation and integration . . . 74

10.3.3 Discussion . . . 74

10.4 High-intensity specular reflectometry . . . 75

10.4.1 Simulation . . . 75

10.4.2 Data acquisition . . . 76

10.4.3 Discussion . . . 76

10.5 Aspects on the data reduction . . . 78

10.5.1 Raw-data and intensity-maps . . . 78

10.5.2 Normalisation . . . 78

10.5.3 Resolution . . . 79

11 McStas Simulations on Reference Sample 81

11.1 Almost conventional mode . . . 85

11.2 λ-θ encoding mode . . . 86

11.3 High-intensity specular reflectivity mode . . . 87

11.3.1 . . . with large q_z-overlap . . . 88

11.4 Discussion . . . 89

12 Prototype **91**
12.1 Design considerations . . . 91
12.2 Devices . . . 91
12.2.1 Pulse chopper . . . 91
12.2.2 Frame-overlap chopper . . . 92
12.2.3 Precision slit . . . 92
12.2.4 Double multilayer monochromator . . . 92
12.2.5 Sample holder . . . 92
12.2.6 Guide support . . . 93
12.2.7 Guide system . . . 93
12.3 Experiment on Amor . . . 95
12.3.1 Set-up on Amor . . . 95
12.3.2 Measurements in the high-intensity specular reflectometry mode . . . 97
12.3.3 Discussion . . . 98

References **101**

1 Scientific Case

Physical, chemical and biological states or processes at interfaces and surfaces become increasingly important in fundamental and applied science. This field extends from improving surface conditioning or understanding biological mechanisms at cell membranes, to the improvement of magnetic data storage and processing, and the investigation of novel phenomena when conflicting properties are forced to coexist on an atomic scale.

One of the best suited methods to investigate interfaces is reflectometry, where the intensity and direction of a beam reflected on a surface is detected as a function of incident energy and orientation. It gives the depth-profile (specular reflectometry) as well as information about lateral inhomogeneities or structure (off-specular reflectivity).

Neutron reflectometry (NR) in particular provides a high penetration depth, sensitivity also for light elements, and it allows for contrast variation by isotope variation — and it probes magnetism. Accordingly, the neutron reflectometry user community and therefore also the demands to the instruments are quite broad. These requirements contain the experimental resolution, the range of length-scales, the sample size, environmental conditions, and measurement time. To serve the broad user community as much as possible it is necessary to build (at least) two reflectometers at the ESS. One has to provide the possibility to measure on horizontal interfaces (liquid / gas or liquid / liquid). Optimising this instrument for typical samples leads to the demand of rather large sample sizes, a wide simultaneous measurement range, and moderate to low resolution. The instrument proposed here, *Estia*, has to complement these features, which leads to the driving design criteria to allow polarised measurements on small samples, often with complex environments. Common to both is the possibility to reach high time-resolution, and to address also surfaces which are structured in two, and to some extend also in three dimensions. To provide full service for the last case, the ESS will need a third instrument, optimised for high resolution also in the sample plane. Building three specialised reflectometers at the ESS is justified by the size of the potential user community and the increasing interest in interfaces. This interest manifests itself in the large and still growing fraction of reflectometers in the instrument suits of existing facilities.

The scientific applications of NR are often separated in *soft* and *hard* matter. Very roughly these used to correspond to the two reflectometer optimisation's mentioned above. This assignment looses more and more its justification, because also organic samples tend to get smaller, or magnetic underlayers are used to give additional phase information for organic samples in combination with polarised neutrons.

In the following sections the special design criteria

- sample size,
- measurement time,
- resolution and q_z-range,
- lateral structure, and
- polarisation

are presented together with scientific examples[1] and a discussion of the performance of *Estia* in this respect.

[1] Input for examples used in this chapter was kindly provided by
a Christian Bernhard, Université de Fribourg, Switzerland
b Jean-Marc Triscone, Université de Genève, Switzerland
c Harald Schmidt, Clausthal University of Technology, Germany
d the ESS scientific and technical advisory panel for reflectometry
e Christof Schneider, Paul Scherrer Institut, Switzerland
f Peter Böni, Technical University Munich, Germany

For clear understanding it is essential to be aware of *Estia*'s unique features: the guide delivers a beam of a wide divergence, strongly focused to the sample. The footprint and the divergence of the beam incident on the sample is defined independently form each other by special diaphragms far before the sample. The focusing limits the maximum footprint width of the beam on the sample to 10 mm. The angular resolution is solely provided by the area-sensitive detector. To allow for a combination of bulky sample environment and high detector angles, the scattering geometry is horizontal. No pulse-shaping is performed.

1.1 Sample size

The driving design criterion for *Estia* was to be able to measure on small samples, or on small selected areas. Small here means below $10 \times 10\,\mathrm{mm}^2$ down to $1 \times 1\,\mathrm{mm}^2$. The maximum footprint of *Estia* is $10 \times 50\,\mathrm{mm}^2$.

Limited sample size

Nowadays many NR experiments on interesting and otherwise suited samples are prohibited by the limited surface area available. The reasons are manifold and include limitations in sample fabrication, the time consumption to provide sufficient amount of material, or the mere costs of the constituents.

single crystals

Bulk materials with interesting surface magnetic properties often can only be grown as relatively small single crystals. Examples are topological insulators in which characteristic magnetic states can be induced by electric currents. There are also ruthenates like $SrRuO_3$ for which a high temperature ferromagnetic surface state has been predicted. [a]

novel electronic phases at interfaces

Thin film samples grown by pulsed laser deposition (PLD) are generally limited in their lateral size. Most materials can be comfortably grown for sizes up to $5 \times 5\,\mathrm{mm}^2$. These limits naturally arise due to the finite size of the laser plume and from the requirement of having a very homogeneous temperature over the entire substrate area. Larger area thin films and multilayers can be grown (for example by toggling) but at the cost of unwanted variations in thickness and structural and chemical homogeneity.
Typical PLD-grown samples are insulating metal-oxide heterostructures which may develop mobile electron gases at the interfaces. These show a rich spectrum of physical properties of increasing scientific and technological interest. A prominent example is the interface $LaSrO_3/SrTiO_3$. It has been established that depending on the number of layers, the interfaces show an integer Quantum Hall Effect, magnetism, or even superconductivity. Gate fields can be used to alter the carrier density to an extent that the electrons are driven to become superconducting. For the investigation of the magnetic and superconducting properties, neutron reflectometry is the method of choice as it is sensitive to buried interfaces. [b]

isotope-labelling, deuteration

One of the strengths of NR is its sensitivity to isotopes. The simplest and cheapest use of this is the contrast variation achieved by using deuterated solvents. Much more effort and costs have to be spent on selective deuteration of groups in molecules to highlight the interesting region, or to sharpen the contrast at interfaces.
To study diffusion processes or to vary the contrast in solid films also other and often very expensive isotopes are needed. [c]

Footprint definition

Estia enables the user to precisely define the footprint on the sample surface independently of the divergence, and without a slit in the vicinity of the sample. The latter feature is important whenever bulky sample environment is used. Furthermore, a defined footprint can be used to select the area of interest on an inhomogeneous sample, to avoid the illumination of uncoated or contacted areas on the surface, or to increase the resolution for measurements on curved samples.

masking of contacts

There are various types of devices based on oxide multilayers in which interesting magnetic effects can be induced by applying a voltage, for example in spintronic or multiferroic devices. In most cases this requires electrodes which need to be contacted on the side of the sample. A small footprint will allow to keep these contacts away from the area that is probed in the PNR experiments. [a]

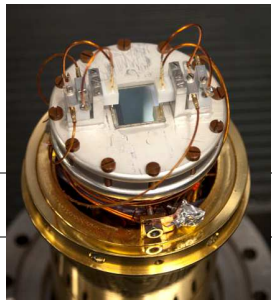

figure: contacted sample as used for MuSR.[4]

solid/liquid interfaces

The adsorption, folding or swelling of proteins and polymers on (coated) silicon make up a large and still growing fraction of NR experiments. For the future it is expected that there will be a shift from these *model systems* towards more complex liquids and substrates, e.g. to the investigation of lubricants or fuel additives on metal surfaces.
In most cases when solid/liquid interfaces are investigated, the liquid phase has to be contained. The required sealing leads to surface regions where the liquid phase is missing, or even a different interface may be present (e.g. viton/silicon). This requires a relatively large but defined beam footprint. The formation of bubbles in solid/liquid cells leads to a laterally inhomogeneous surface on a mm to cm scale. With a small footprint it is possible to select an undisturbed area. [d]

Scanning of samples

The small footprint can also be used to scan sample surfaces with a mm-resolution.

wedge-multilayers

Multilayers with a ramp-type change of the layer thickness in one direction could be used to measure very efficiently the influence of the layer thickness on the magnetic properties, by scanning the neutron beam along the ramp direction. [a]

Measuring over a large sample size implies averaging over the whole surface area and thus details from inhomogeneities are completely lost. Focusing on very small surface areas ($\approx 1\,\mathrm{mm}^2$) will enable scanning the samples therefore detecting inhomogeneities within the sample plane with high detailed structure in the direction perpendicular to the interface. Thus, this reflectometer can be though as a neutron profilometer that probes the density profile perpendicular to the interface on a mm scale, rather than just its outer morphology.

materials science at solid-solid interfaces

A large number of interface-related investigations or developments do not provide the flat and homogeneous samples as known from electronic devices. Examples for demanding substrates are concrete, apatite (bones, teeth), or polymers. Also the various methods for adhesive bonding (gluing, brazing, welding) lead to lateral inhomogeneities on a mm-scale. [d]

Compatibility with other techniques

Techniques complementary to neutron reflectivity such as XRD, XMCD or resonant x-ray reflectometry performed at synchrotron sources, or probes like SQUID or transport measurements often impose a restriction on the sample size of $5 \times 5\,\mathrm{mm}^2$ to $1\,\mathrm{cm}^2$. It is a big advantage if the very same sample can be investigated also by neutron reflectometry.

Restricted space

One advantage of neutrons is their potential to penetrate or pass through material with only moderate losses. This enable studies under extreme conditions. The more extreme these get, the less space is available for the sample. Examples are high and homogeneous magnetic fields, fast and homogeneous heating or cooling, application of high pressure.

1.2 Measurement time

The peak flux gain of the ESS compared to existing neutron sources and its efficient use by *Estia* will reduce the measurement time by at least one order of magnitude. Another order can be gained for moderate size to small samples by using *Estia*'s unique high-intensity secular reflectivity mode.

Reduction of time for normal measurements

For small samples or for measurements up to high momentum transfer the measurement time nowadays can reach up to several hours. A reduction by an order of magnitude enhances the throughput of experiments. The limiting factor then will be the times needed for mounting and aligning the sample, and to reach the required environmental conditions (high magnetic fields, low temperatures).

Screening of the response to multiple varying external conditions

What makes samples interesting is their complex behaviour as a function of one or several parameters as temperature, electric or magnetic fields, shear, or pressure. Fast measurements (eventually on a small q_z-interval, only) will enable the mapping of the phase diagram and the identification of the most interesting parameter combinations for further investigations.

multifunctional materials

The last few years have witnessed tremendous activity in the search for multifunctional materials combining magnetic, charge and orbital degrees of freedom, which may be controllably tuned. These systems combine several *ferroic* properties, i.e. symmetry breaking order parameters such as polarisation, magnetisation, and strain, which are subject to control parameters such as electric and magnetic field, and stress, respectively. The most direct way to engineer the desired functionality at room temperature is the combination of ferroic materials in a heterostructure. For the investigation of the interactions between the magnetic and non-magnetic layers, neutron reflectivity is the only means to directly determine the formation of magnetic order and domains.
One example is the strain-induced ferromagnetism at the film/substrate interface in orthorhombic $LuMnO_3$ thin films. Materials featuring the co-existence of coupled magnetic and ferroelectric order allow the switching of magnetic moments by an electric field and vice versa.[5, 6] Experimentally, only a few multiferroic materials are known to be ferromagnetic (FM), with the large majority being antiferromagnetically ordered. This class of materials can potentially be used for future magnetic storage devices with an electronic read-out. To non-destructively identify and probe the spatial extend (thickness dependence) of ferromagnetism in a thin film, polarised neutron reflectomentry (PNR) reaching large q_z is the best suited technique.[7, 8] Single crystalline-like thin films of orthorhombic $LuMnO_3$, a material which is known to exhibit magnetically-induced ferroelectricity with an E type antiferromagnetic (AFM) ground state, were found to have FM localised close to the substrate-film interface.[9] Surprising is the fact, that an intrinsic robust AFM can be converted into a FM with $T_C > T_N$. The most likely origin is growth-induced strain at the substrate/film interface and a change in crystalline symmetry.
Future PNR experiments will address the exchange biased coupling of the FM and AFM when applying electric fields. The samples have to have electrodes structured onto the surface, which limits the space available to conduct the reflectivity measurements. [e]

With the high-intensity mode of *Estia* it is possible to obtain reflectivity curves within seconds to minutes (in comparison to ramping times for a magnetic field or for temperature of the order of an hour).

Monitoring of slow processes

The possibility to repeat measurements on tiny samples or up to high q_z within a few seconds to minutes on *Estia* allows to investigate slow processes.

diffusion processes in solids

Self-diffusion of atoms in solids is a fundamental point-defect mediated matter transport process. It plays a key role for the design and optimisation of materials as well as for the performance of devices in various branches of technology like energy storage/conversion, electronic devices, and sensor technology. The investigation of diffusion processes on very short lengths scales ranging from atomic distances up to some tens of nanometers is an emerging field of research. It is especially important for the characterisation and design of nanostructured materials, metastable compounds and thin films as well as for the study of diffusion process close to room temperature and ultra-slow diffusion processes.
A method which can be used to realise such measurements is neutron reflectometry in combination with isotope multilayers [10]. Using this method, the destruction of an artificial lattice of stable isotopes by

thermally induced interdiffusion is detected. Up to now, the method was used ex-situ to study self- and impurity diffusion in complex amorphous materials and metastable chemical compounds [10, 11, 12], in nano-crystalline metals [13], in single crystalline semiconductors [14], in ion conductors [15] and in electrode materials for Li-ion batteries [16].
In the framework of a seminal advancement of the method, in-situ experiments at elevated temperatures should be carried out in order to monitor real-time atomic migration processes in equilibrium and non-equilibrium states. This requires superior time resolution (seconds) for specular reflectivity, the use of small samples ($< 25\,\mathrm{mm}^2$) due to handling with expensive isotopes, and for ensuring fast and homogeneous heating and cooling. Furthermore, a q_z-range up to $0.4\,\text{Å}^{-1}$ for the detection of diffusion close to atomic distances is required. [c]

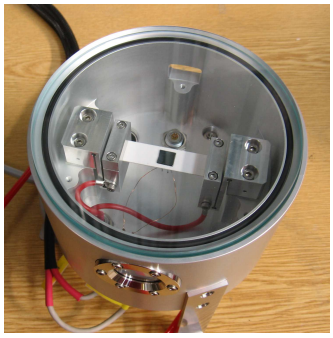
In-situ furnace for the *Selene* prototype on Amor@PSI.

The time-resolution for wide q_z-ranges on *Estia* is mainly limited by the time needed to move the detector. For $q_z \in [0.01, 0.2]\,\text{Å}^{-1}$ a resolution of a few seconds is possible.

High time-resolution
The highest time-resolution for TOF reflectometry at the ESS is given by the pulse repetition rate of 14 Hz. Even with the flux delivered by the ESS it is very challenging to perform *normal* reflectometry measurements using only one neutron pulse. The high-intensity specular reflectivity mode *Estia* provides the possibility to reach a time resolution of 0.1 s on a narrow q_z interval, which is still sufficient to trace e.g. the evolution of Bragg peak intensities, or the shift of Kiessig fringes.

in-situ monitoring of film growth
The in-situ characterisation of thin films during growth by means of electron diffraction, for example RHEED, and even scanning probe microscopy or photo-spectroscopy is common practise. However, only a few efforts have been made to characterise the evolution of the magnetic properties during the deposition of the layers. Neutron reflectometry is the method of choice as it measures directly the magnitude and the orientation of the magnetic moments throughout the heterostructure on a microscopic scale, in contrast to XMCD where only the surface is measured and vector information is lost. [f]

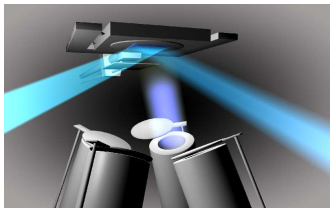

chemical processes
Split-second time-resolution allow to monitor chemical reactions at or close to surfaces initiated e.g. by stop flow in microfluidics chambers, or by triggered with a laser pulse. [d]

1.3 Resolution

The range of resolutions needed for the various NR experiments ranges from 1% to 20%, depending on the thickness of the film/layer of interest.

topological materials
Heterostructures made from topological materials involving chiral structures such as the B20 compound MnSi or thin films (even monolayers) showing chiral magnetic order driven by the inversion symmetry at interfaces may become important functional materials for information technology or spintronics because the involved chiral entities are intrinsically very stable because they are protected by topology. In these materials several length scales compete with each other, for example exchange length, modulation length, film thickness, etc. A wide adaptability of the resolution (1% to > 10%) will allow to investigate the structural and magnetic properties over a very wide range of length scales while maintaining a high intensity.[a]

Estia has an intrinsic resolution of $\Delta q/q \approx 4\%$. This means it is not possible to increase the flux by lowering the resolution. It is just possible to increase the statistics per data point by binning to low resolution. High (2%) and very high (1%) resolution can be reached on *Estia* by λ-θ-encoding.

Dynamic range

The higher flux at ESS allows to measure higher momentum transfer and thus thinner structures, as long as the specular signal can be separated from the background. The *Selene* guide system results in a low environmental background and it allows to avoid the illumination of the sample environment. But for all reflectometry measurements the diffuse scattering from the sample itself sets a limit. For hydrogen-containing samples this is of the order of 10^{-7}, for the often used substrates Si, SiO_2 or $SrTiO_3$ it is $> 10^{-8}$.

The clean focused beam available on *Estia* allows for an approach to enhance the signal-to-background ratio on samples with at least 2 cm width. In *normal* reflectometry samples with a high intrinsic background suffer from the fact that both, the specular and the diffuse scattering spread across the detector in the direction normal to the scattering plane.[2] By using a beam focused in the sample plane to the detector rather than to the sample, the specular signal is concentrated on a small region, while the diffuse background is still spread out. Masking the non-specular part allows to increase the signal-to-background ratio by up to two orders of magnitude. This can be realised on *Estia* with an optic before the sample, which re-focuses the beam to the detector.

q_z-range

The range of film or interface thicknesses reaches form atomic distances to micrometers. This results in a maximum $q_z \approx 3\,\text{Å}^{-1}$ and a resolution of $\Delta q_z \approx 5 \cdot 10^{-4}\,\text{Å}^{-1}$. While the latter can be realised on *Estia* for moderate q_z with $\Delta q_z/q_z = 1\%$, the q_z-range is limited by the peak-to-background ratio accessible on a reflectometer, rather than by the mechanical constraints.[3] Realistically, the dynamic range limits q_z to about $0.7\,\text{Å}^{-1}$, which corresponds to a minimum film thickness of 10 Å. This limit is holds for single films on a substrate. In case there are thicker underlayers, one can deduce the film thickness on an atomic scale by the phase it induces in the signal from the underlayer(s).

1.4 Laterally structured films

The relatively simple theoretical description and the relatively strong signal favoured specular reflectivity in the past. This means most of the experiments probed essentially the depth-profile. On the other hand the scientific interest turns more and more towards laterally structured sample, which demands for (in-plane) off-specular scattering probing length scales of 0.6 to 60 µm, and for out-of-plane scattering for lengths of 1 to 100 nm.

Off-specular scattering

In-plain off-specular scattering gives information about the lateral inhomogeneity of the sample in the µm-range. This allows for measuring the size of domains, or the periodicity and density profile of artificially structured or patterned surfaces.

finite size effects in complex oxides

A number of interesting finite size effects on the magnetic and superconducting properties could be studied in nanostructured samples of complex oxides, like manganites, ruthenates or cuprates. In a collaboration between the University of Fribourg and the laboratory for nanotechnology at PSI, x-ray lithography and lithography with an e-beam writer have been used already to produce large area samples (up to 4 mm^2) with micro- and nanostructures (squares and lines with different sizes and spacing).[a]

It is important to stress that *Estia* can be operated almost like a conventional TOF reflectometer. *Almost* means that the beam is nevertheless convergent. The only restriction is the maximum sample width, all other features are not compromised. This means that the brilliance available for off-specular measurements is about the same as for a conventional instrument.

[2] For the specular signal this is caused by the high divergence in this plane, used to enhance the signal strength.

[3] *Estia* can reach $q_z = 2\,\text{Å}^{-1}$ with a detector angle of 105.5°. For neutron reflectometry this does not make sense, but it allows for the determination of the substrate orientation by measuring its Bragg peaks.

GISANS

Once there is an easy-to-use formalism to analyse and interpret GISANS measurements it is expected that the demand for beamtime dramatically increases.

The beam needed for this Grazing Incidence Small Angle Neutron Scattering (GISANS) has to be highly brilliant, which restricts this method to the high-flux neutron sources. For the same reason theses measurements are often performed on SANS instruments rather than on reflectometers. As a result, the specular reflectivity needed for data analysis has to be obtained separately on a different instrument. It thus is desirable that a new reflectometer at a source with high brilliance allows for the implementation of a GISANS option.

Estia can be equipped with an optic to focus the beam onto the detector in the sample plane, which allows to perform (polarised) focusing GISANS. This is analogue to the multi-beam-focusing implemented on REFSANS, FRM 2.

1.5 Polarisation

The investigation of magnetic depth profiles and of magnetic reversal processes is one of the main applications for *Estia*. Spin polarisation and spin analysis are essential options of any respective neutron reflectometer already today, and even most of the soft matter reflectometers have at least a polarisation option.

magnetic heterostructures

Heterostructures involving magnetic materials are the basic building blocks of a large number of magneto-electronic devices such as read heads or magnetic random access memories. In addition, such heterostructures are increasingly being used as magnetic sensors in industrial applications and in the automotive industry. The performance of magnetic devices relies on the magnetic and elastic properties of the individual layers and on the coupling between the layers. These effects are a function of the morphology and microstructure of the grown layers and accordingly change during the growth of the heterostructures. To determine the structure within the layers and the perfection of the layers, reflectometry with polarised neutrons is a very powerful tool as it allows performing vector-magnetometry in heterostructures, layer by layer. The current trend is to decrease the size of the devices and to go towards thinner layers. Therefore, it is very important to adapt the experimental techniques to cope with the small cross-sections of these materials. [e]

Induced magnetism at oxide interfaces

The recent discoveries of a number of fascinating unexpected phenomena at interfaces between different perovskite oxides have been received with tremendous enthusiasm, leading to the emergence of the field of oxide interface engineering.
The conduction properties found at some interfaces between insulating oxides have attracted a lot of attention. Such conducting interfaces, first discovered in 2002 between a Mott insulator ($LaTiO_3$) and a band insulator ($SrTiO_3$) [17] and in 2004 between two band insulators ($LaAlO_3$ and $SrTiO_3$) [18], have been shown to host two-dimensional electron gases. These discoveries generated an impressive amount of work trying to understand the origin of the conductivity and studying the properties of these fascinating systems, among them superconductivity and magnetism [19, 20].
Several oxide interface systems display induced magnetic structures. Among those, the observation of exchange bias in superlattices composed of nominally paramagnetic metallic $LaNiO_3$, and ultrathin semiconducting ferromagnetic $LaMnO_3$ layers is particularly exciting [21].[b]

magnetic contrast variation

Polarised neutrons can also help in characterising non-magnetic films. For the phase-sensitive specular neutron reflectometry (PSNR) [22] a well-characterised magnetic underlayer can be used to switch the contrast. A common analysis of the respective reflectivity curves allows to retrieve the phase information and thus leads to a unique depth-profile. [d]

1.6 Overlap with the liquids reflectometer

It will be possible to realise the vast majority of present-day experiments on *Estia* and a complementary liquids reflectometer at the ESS. The varying demands concerning time resolution, footprint size, compatibility with sample environments and so on finally decide about the instrument of choice to make the most out of the high neutron flux from the source.

Nevertheless, the expectations of cutting-edge science fields led to the mutually excluding design criteria resulting in at least two reflectometers. Completely excluded on *Estia* are measurements on gas/liquid or liquid/liquid interfaces due to the horizontal scattering geometry.[4] These experiments and the related design criteria form the key drivers for the other reflectometer to be build at the ESS. Since soft-matter samples often can be produced with surface area of $10\,\mathrm{cm}^2$ to $100\,\mathrm{cm}^2$ they would profit from a footprint larger than $\approx 1 \times 5\,\mathrm{cm}^2$, which is about the upper limit for *Estia*. Besides these limitations, the proposed instrument can be used for typical soft-matter measurements as well — in some cases even opening up new possibilities as shown above.

1.7 Infrastructure & support facilities

Sample environment

The sample environment needed to cover the standard applications contains cryomagnets (state-of-the-art are $7\,T$, asymmetric field), cryostats, Helmholtz coils (for lower fields, often combined with a closed-cycle refrigerator), and in-situ furnaces.

More specialised equipment as liquid/solid cells often is provided by the users. For these a device for thermalisation should be present at the instrument.

Various devices will need at need supply of power, gases (N_2, Ar, He) and cooling (water), eventually also He recovery.

Sample preparation and storage

For sample preparation, a chemistry lab should be located not too far away. This is mainly needed by the soft-matter community, but it might also serve e.g. for (HF−) etching a substrate prior to in-situ growth studies. A growing fraction of the soft-matter community will need access to a deuteration lab.

A furnace for off-situ annealing, a glove box, and a fridge for sample storage should be accessible.

It proved to be very helpful at PSI to have direct access to a small workshop in the experimental hall (also as a user), and to mechanical support on short notice. E.g. to modify or build adapter plates or sample holders.

Data analysis

The much shorter measuring times at the ESS will alter the way measurement campaigns are performed towards a scheme as practised at synchrotrons. Decisions about the course of the experiments will have to me made within minutes. It is thus essential that the user has almost instant access to the reduced data, and also to some data analysis tools.

For the same reasons the size of the experiment crews will grow, which demands for sufficient and well equipped workspace.

[4] According to the estimates of the reflectometry STAP this accounts for about 25% of all reflectivity experiments.

2 Description of Instrument Concept and Performance

It is proposed to build a polarising reflectometer, optimised for samples of $10 \times 50\,\mathrm{mm}^2$ area, or less, capable to cover a wide q_z-range with variable resolution. The scattering plane is horizontal to allow for wide detector angles. The unique feature of this instrument is its truly focusing guide system, which reduces background and illumination of sample environment, and which opens new possibilities for beam shaping and filtering.

The actual design of *Estia* and its properties as presented below are the optimum result of following the ESS baseline parameters, the recommendations by ESS experts, and the recommendations given by the STAP. E.g. the decision to use two subsequent *Selene* guide systems was triggered by the spatial constraints within the first 6 m after the moderator, by the strongly limited accessibility of any component within the common instrument shielding, and by the recommendation of the STAP to avoid the prompt time for data acquisition and to sacrifice some brilliance transfer. The result is an excellent shielding against fast neutrons, easy access to all critical mechanical components, and a convenient manipulation of the beam footprint. The price to be paid is a lower transmittance of the guide system (the number of reflections is doubled), and smaller q_z-range accessible with one sample orientation.

The high flexibility of the instrument concept makes it possible to adapt the design of *Estia* to upcoming changes of the constraints. As there might be a pan-cake moderator, or an efficient suppression of fast neutrons from the prompt pulse (including secondary processes). [→2.11]

There is also a high degree of flexibility in design details, such as the various ways to polarise the beam. In the following the favoured approach is presented in detail, possible options are mentioned and might be explored in the further design process.

Normally, neutron guides are designed to optimally feed the secondary instrument, and at the same time perform some filtering. For *Estia* this is different because the *Selene* guide offers new measurement schemes for

Table 2.1: Key features of *Estia*

parameter space		
q_z-range	$[0, 1]\,\mathrm{Å}^{-1}$	to be covered in 5 measurements
λ-range	$[5, 9.4]\,\mathrm{Å}$	
sample size	$[0.3, 50] \times [0.3, 10]\,\mathrm{mm}^2$	$x \times y$
maximum divergence	$\Delta\theta_{xy} = 1.5°$	scattering plane
	$\Delta\theta_{xz} = 1.5°$	sample plane
intrinsic resolution		
$\Delta\lambda/\lambda$	2.1%	5.0 Å
	4.0%	9.4 Å
geometry		
scattering plane	horizontal	
total length	58.0 m	
sample / detector	6.2 m	
2θ	$-2°$ to $50°$ ($110°$)	for $q_z \leq 1\,\mathrm{Å}^{-1}$ ($2\,\mathrm{Å}^{-1}$)
moderator	cold	

reflectometry. These include for example a high-intensity mode for time-resolved measurements or tiny samples. It also enables the precise determination of the beam footprint on the sample and the beam divergence. This happens far from the sample, offering more flexibility for the sample environment. And both features are decoupled and controlled by independent devices.

Thus the understanding of the *Selene* guide is essential for the instrument design, and this is why it is presented first [→2.1], followed by the actual lay-out of *Estia*. The further sections of this chapter deal with the operation schemes [→2.8], simulations [→2.9], and a discussion of the performance [→2.10].

2.1 Selene guide

principle The *Selene* guide concept is the result of the attempt to develop a guide which transports only the useful neutrons, and which allows for a beam manipulation similar to what an objective does with optical light. There, the point-to-point focusing property allows to define the beam spot size at the image position with a diaphragm located at the pre-image. The divergence of the beam can be controlled by an aperture behind the optical lens, far from the image.[1]

For neutrons the lens has to be replaced by a reflecting device, here a planar-elliptic mirror. It is important to notice that the *guide* consists indeed only of two mirrors, one reflecting horizontally, the other vertically, rather than of a tube with rectangular cross-section. The *Selene* guide can be seen as an extended Montel optic [23] as used at synchrotron beam-lines.

Like all optical devices, the elliptic reflector suffers from aberration. For an elliptic reflector coma aberration is largest for reflections close to the focal points. It is thus essential to avoid these regions.[2] The remaining coma aberration can be partially correct for by using two subsequent reflectors [→6.3]. In total this leads to a guide as illustrated in figure 2.1.

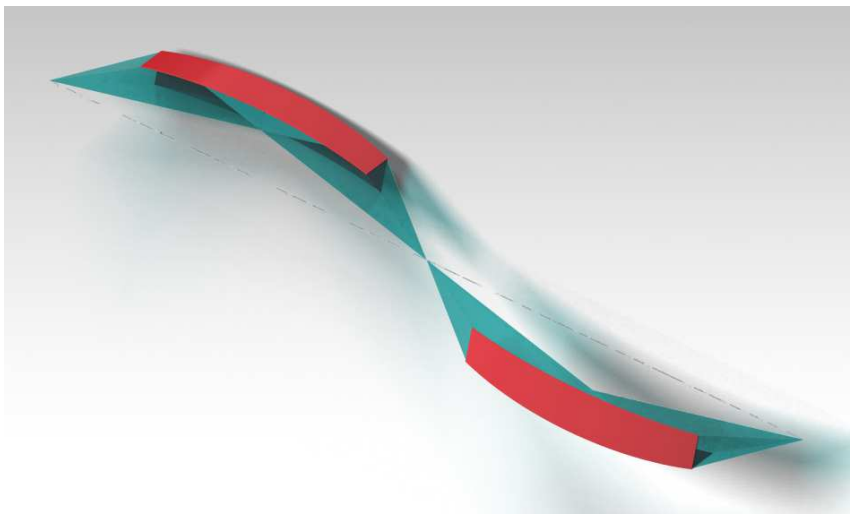

Figure 2.1: Sketch to illustrate the shape of the *Selene* guide. Shown are two segments with L-shaped cross-section (red), sharing the long axis and a focal point. In blue the beam progression is shown.

Such a guide system transports only neutrons originating from a defined region around its initial focal point with a defined divergence. And it maps these to an almost identical region at the second focal point. Outside this phase space volume, the intensity is ideally zero. Thus the guide can be designed in a way that in combination with an initial aperture at the first focal point, it transports only neutrons actually hitting the sample. This has the consequence that radiation issues and illumination of the sample environment are strongly reduced. The divergence of the beam can be controlled (independent from the spot size) by an aperture right behind the guide exit.

Because the concept implies that each neutron is reflected exactly once on each reflector, there is no direct line of sight to the first focal point from any position behind the first reflector segment. Indirect line of sight reaches up to end of the second segment.[3]

[1] For a nomenclature of shading optical elements please refer to table 5.2, page 40.

[2] This is the reason why most other guide concepts based on elliptic guides are not exactly focusing: they suffer from strong coma aberration effects leading to multiple reflections and thus create a divergent beam at the exit.[2, 3] [→6.2]

[3] Thus the ESS recommendation to get out of line of sight half way down the guide, and to avoid indirect line of sight is inherent to the *Selene* guide.

Table 2.2: Parameters of the double *Selene*-type guide for *Estia*. a and b are the half axis lengths of the ellipses, c is half the distance between the focal points. ξ relates the length of the actually built guide to this distance. Please refer to appendix 5 for a full list of used symbols and abbreviations. The offsets originate from the parallel shift of the beam introduced by a *Selene* guide.

guide parameters		
c	6.0 m	half distance between focal points
ξ	0.6	length of the reflector relative to $2c$
b/a	0.01754	$\Rightarrow \quad b = 105.26\,\text{mm}, \quad a = 6000.92\,\text{mm}$
ϵ	1.25°	inclination of the guide system
distances		
moderator / pin hole	4.2 m	first focal point
$2c$	12.0 m	lengths of ellipses
$\xi \cdot 2c$	7.2 m	length of (coated) guide sections
$(1-\xi) \cdot 2c$	4.8 m	space between guide sections
$(1-\xi) \cdot c$	2.4 m	space before sample
sample / detector	6.0 m	
Δz at sample	522.7 mm	vertical offset of one *Selene* section
Δy at sample	522.7 mm	horizontal offset of one *Selene* section
coating		
m	3.0	critical edge
coated area	4 m^2	
material	Ni/Ti supermirror	

guide transmission

λ	t
5 Å	42%
6 Å	52%
7 Å	59%
8 Å	66%
9 Å	71%

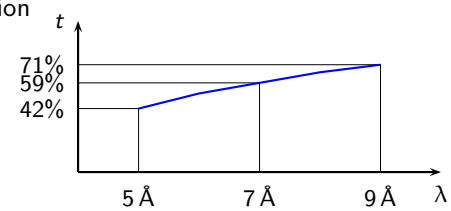

based on McStas simulations

adaption to Estia The guide system for the presented reflectometer consists of two such *Selene* guide sections: The first has to create a *virtual source*[4] with defined size and divergence, but twice out of line-of-sight from the moderator. This virtual source is in a low-radiation region so that sensitive mechanical equipment and optics can be used there. It is also possible to access this area for maintenance during operation (with the instrument shutter closed). At and around the virtual source, the beam is manipulated as is necessary for the measurements. This includes the definition of the footprint and optionally polarisation and angle-wavelength encoding. The second *Selene* guide has to map the shaped beam to the sample. The divergence (and eventually the incident angle) of the beam are defined by an aperture behind the last guide segment. This way spot-size and divergence are adjusted independently (analogue to image size and resolution in optics being defined by a luminous field diaphragm and an aperture). For one operation mode [→2.8.2] it would be favourable if this aperture could be scanned over the guide exit within one pulse. Table 2.2 gives the geometrical parameters of the ellipses, the measures of the guide and the coating.

The use of two *Selene* guides has the consequence that each neutron is reflected exactly 8 times before it arrives at the sample. The resulting reduction in intensity (see graph in table 2.2) is the price one has to pay for low radiation and for convenient beam manipulation.[5]

[4] To avoid confusion with the large number of focal points, the one shared by the two *Selene* guide sections is further referred to as *virtual source*.

[5] Based on the experience at ISIS and SNS, the STAP recommended strongly to avoid data collection during the prompt pulse. This influenced the instrument's total length. [→2.3.1] In combination with the enforcement of the shielding (early out of line of sight) and with the poor accessibility of the region close to the moderator, this was the driving argument to use two *Selene* guides. The consequence is that the beam intensity on the sample is attenuated by another 16% to 35% for $\lambda = 9$ Å to 5 Å.

2.2 Instrument lay-out

The principle instrument lay-out is shown in figure 2.2. The various components are briefly presented in table 2.3. A more detailed discussion follows in the next sections.

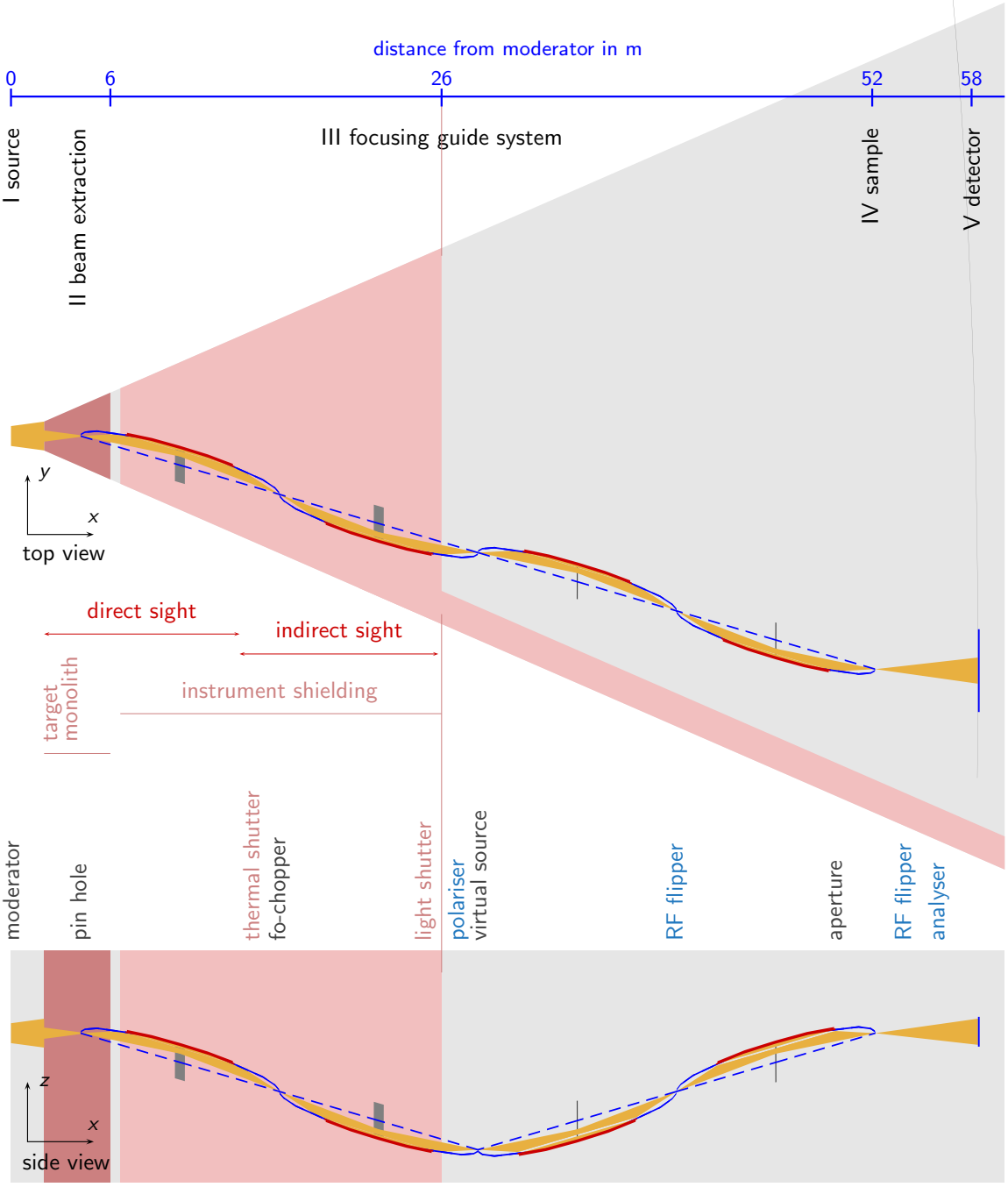

Figure 2.2: Sketches of the instrument lay-out. The sketches are to scale, where direction normal to the beam is stretched by a factor 10 for clarity. The gray area in the upper sketch represents a 5° wedge on the floor. The detector will move outside this area for high angles (gray line). The light red area represents shielding, i.e the target monolith, the common instrument shielding and individual instrument shielding. The thick red lines represent the *Selene* guide segments, where the blue lines give the shapes and the long axis of the related ellipses. The golden area is the beam path (assuming no divergence restriction (aperture open) and no sample (direct beam). (For the nomenclature of the components, please refer to chapter 5 and to figure 5.1.)

Table 2.3: Positions of the essential devices along the instrument. All components in between the target monolith exit and the detector will be in vacuum, with the exception of the sample and the sample environment. All positions outside the guide segments (marked in red) are available for further equipment, e.g. for a spin-echo set up, or for (de)focusing reflectors.

position x/ m	device	
		I
0.0	moderator	The instrument needs a cold moderator[6] as neutron source, where the effective flux maximum (i.e. including losses and rescaling [→2.3.1]) determines the minimum wavelength λ_{min}.
		II
4.2	pin-hole	The purposes of the beam extraction unit are to form a $10 \times 10\,mm^2$ pin-hole, and otherwise to stop as many fast neutrons and γ radiation as possible.
		III
6.6 -13.8	1^{st} guide segment	
14.0	thermal shutter	to allow for access to all components outside the concrete shielding
16.2	frame-overlap chopper	the beam cross section at the chopper position is $30 \times 30\,mm^2$.
18.6 -25.8	2^{nd} guide segment	
25.9	light shutter	
26.0	end of concrete shielding	
26.0 -28.0	polariser	optional, curved transmission polariser [→2.4.3]
28.1	monitor	
28.2	virtual source	= luminous field defining diaphragm
30.6 -37.8	3^{rd} guide segment	
40.2	RF flipper	
42.6 -49.8	4^{th} guide segment	
49.9	aperture	to define the divergence of the beam incident on the sample. If feasible, with the option to be scanned across the beam width within one pulse (scanning aperture) [→2.4.2].
		IV
52.2	sample	located at the final focal spot of the guide [→2.5] No optical element is necessary behind the aperture, so that there is 2.2 m space for sample environment.
		V
52.6 -58.2	evacuated flight path	
	RF flipper	
	spin analyser	optional
58.2	detector	position sensitive [→2.6]

[6] Since the *Selene* guide of *Estia* accepts only neutrons from a $10 \times 10\,mm^2$ spot, it is possible to use a pan-cake moderator instead of the presented combination of the baseline moderator and a pin-hole. The flux gain would be the gain in brilliance of the moderator.

2.3 Energy- and time-range

The time and energy characteristics of the ESS long-pulse source allows for a relatively wide λ-range, while keeping the intrinsic instrument resolution below ≈ 4%, and avoiding the proton pulse time for measurements. A full reflectivity curve is thus achieved by piecing together (a few) measurements with varying angle of incidence. Further stitching due to complex chopped beam characteristics is not necessary.

2.3.1 Flux and λ_{min}

The experience with existing TOF reflectometers is, that the lower limit of the wavelength spectrum λ_{min} corresponds to the effective flux maximum at the sample position. The reason is that even smaller λ result in higher q_z and thus in general in lower reflectivity, and at the same time in lower incident intensity. Thus the accuracy of the data rapidly decreases and it is much more appropriate to measure at a higher angle of incidence to access the corresponding q_z-range.[7]

The effective flux at the sample can be estimated by reducing the initial flux $I_0(\lambda)$ by the losses due to reflections on the guide walls, and by taking into account that in the end one aims for $\Delta q/q$ = constant or close to constant.

The double *Selene* guide concept involves 8 reflections for all neutrons on surfaces with a non-perfect reflectivity R. Since the angle of incidence on the guide surface hardly varies along the guide for the presented concept, one can assume an attenuation of [→6.5] $I(\lambda) \approx I_0(\lambda) \cdot R(\lambda)^8$.

A more prominent effect comes from the required $\Delta q/q$ = constant: effectively, the time-bins, and thus the λ-bins necessary for $R(q_z)$ curves follow $\Delta\lambda/\lambda$ = const, which shifts the spectral weight to bins with larger λ. This shift can be approximated by $I(\lambda)_{\Delta\lambda/\lambda\,=\,\text{const}} \propto \lambda \cdot I(\lambda)_{\Delta\lambda\,=\,\text{const}}$

This way the minimum wavelength $\lambda_{min} = 5\,\text{Å}$ was determined, as illustrated in figure 2.3.

2.3.2 Time regime and λ_{max}

In order to avoid a contamination of the measurement with background originating from the proton pulse and secondary processes, the instrument's length was chosen so that the 5 Å neutrons arrive at the detector right after a pulse. This leads to a minimum length (moderator to detector) of 58 m. And the time between pulses sets the upper wavelength limit to $\lambda_{max} = 9.4\,\text{Å}$. Figure 2.4 shows the corresponding t-x-diagram.

[7] In case the width of the q_z-range covered within one pulse is essential, one might accept also a smaller λ_{min} for the cost of a dramatically increased measurement time.

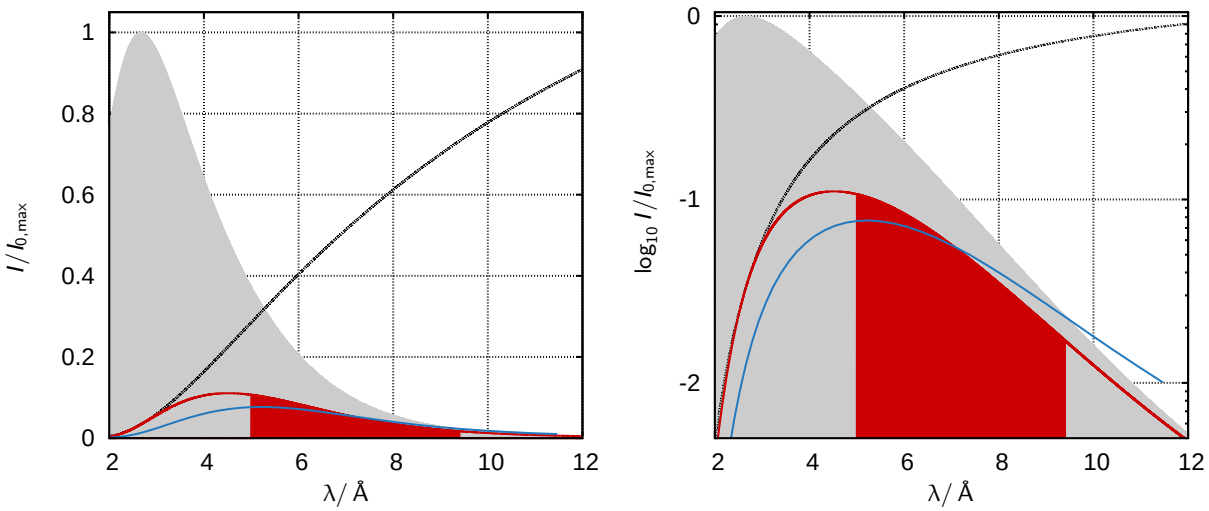

Figure 2.3: Spectra $I(\lambda)/I_0$ (left) and $\log_{10} I(\lambda)/I_0$ (right) as given by the source (gray area), after attenuation according to eqn. (6.5.2) with 8 reflections (red line), and after re-binning it to $\Delta\lambda/\lambda = 2\,\%$ (blue line). The latter line is scaled by an arbitrary value. The black line is the transmission of the guide. The source spectrum $I_0(\lambda)$ is the one used by the McStas component `ESS_moderator_long`. The red area represents the neutrons actually arriving at the sample.

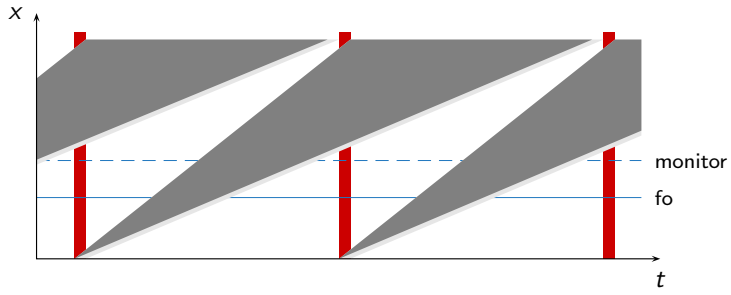

Figure 2.4: Sketch to illustrate how to avoid the influence of the γ and fast neutron burst from the proton pulse hitting the target. The sketch is to scale with period $T = 70\,\text{ms}$, pulse length $t = 3\,\text{ms}$, and a sample detector distance of 58 m, i.e. $\lambda \in [5, 9.4]\,\text{Å}$. The dashed and solid blue lines correspond to the location of the monitor and frame-overlap chopper, respectively.

To also avoid a contamination of the signal used for normalisation, the monitor is located so that it measures in the first frame. An ideal position is right behind the exit of the second guide segment at $x \approx 26\,\text{m}$ (dashed line in figure 2.4).

2.3.3 Intrinsic λ-resolution

The time-resolution is given by the pulse length τ. At the detector position (at $X = 58\,\text{m}$) this corresponds to $\Delta\lambda \approx 0.2\,\text{Å}$. [→8.3.1] Thus the wavelength resolution in the interval $\lambda \in [5, 9.4]\,\text{Å}$ varies from $\Delta\lambda/\lambda = 2.1\%$ at $\lambda = 9.4\,\text{Å}$ to $\Delta\lambda/\lambda = 4.0\%$ at $\lambda = 5.0\,\text{Å}$.

2.3.4 Frame-overlap suppression

A frame-overlap chopper will be installed at the intermediate focal plane within the first guide section at $x = 16.2\,\text{m}$ (blue line in figure 2.4). The beam cross-section there is $\approx 30 \times 30\,\text{mm}^2$. This chopper, running with the source frequency, suppresses all neutrons below 5 Å, and all neutrons above 9.4 Å, with windows at $\lambda \in [22.1, 26.5]\,\text{Å}$, $\lambda \in [39.2, 43.6]\,\text{Å}$, and so on. To *close* these windows, neutrons with $\lambda > \lambda_{\text{max}} = 9.4\,\text{Å}$ will also be suppressed by using a transmission filter. A silicon wafer with a Ni coating ($m = 1$) shaped like a logarithmic spiral [→7.1] is installed before the virtual source. The shape assures that all trajectories pointing towards the virtual source hit the wafer at the same angle (here 0.95°).[8] For neutrons with $\lambda < \lambda_{\text{min}} = 5\,\text{Å}$ the coating of the guide acts as an attenuator.

2.3.5 Choppers

The frame overlap chopper is discussed in the section above.

For this instrument and the operation schemes presented in section 2.8 no pulse-shaping choppers are foreseen.[9]

2.4 Beam manipulation

2.4.1 Footprint definition (beam size)

The beam shape at the sample position is essentially defined in between the two *Selene* guide sections, 24 m upstream. This is because the *Selene* guide is a three-dimensional imaging system (for small volumes close to the focal points). It is thus possible to define the footprint on the sample surface by a diaphragm which has an opening (luminous field) of the shape, size and orientation of the footprint. For the scattering plane this can be realised by two blades oriented normal to the beam, but which open by a separation along the beam rather than orthogonal to it.[10] Figure 2.5 illustrates this in a sketch. This device has only marginal influence on the beam divergence.

The virtual source has to have the same orientation as the sample. The mentioned diaphragm is therefor mounted on a stage with the same degrees of freedom as the sample stage [→2.5], i.e. x, y and z translation and ω rotation. The demands concerning load and magnetic influences are much weaker.

[8] In case the beam is to be polarised this space is occupied by the transmission polariser [→2.4.3]. But since this has the same shape, the band-pass filter coating is deposited on top of the polarising supermirror.

[9] Since the *Selene* guide system in the end fulfils the same task as a *normal* guide, it could be combined with multi-chopper setups for Repetition Rate Multiplication or for Wavelength Frame Multiplication [24]. In the large free regions between the guide segments of the *Selene* guide this would not cause any modifications to the guide. A chopper within the reflecting part results in gap in the divergence distribution.

[10] Such a diaphragm was build at PSI and will be operational 04. 2014.

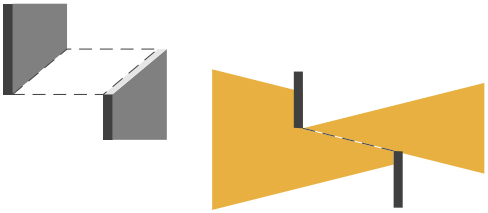

Figure 2.5: Sketch of the diaphragm forming the virtual source (in the scattering plane). The left image shows a bird's eye view of the two blades. The opening they define (dashed line) is almost parallel to the beam. The right sketch shows a horizontal cut. The convergent beam (from the left) is transformed into a divergent beam, which seems to emerge from the (dashed) opening.

2.4.2 Divergence definition and scanning aperture

The mentioned footprint-defining diaphragm has only marginal influence on the divergence because it is located at a focal point. The divergence has to be defined before or behind the focusing element, i.e. at the entrance or exit of the *Selene* guide. To account for possible imperfections of the guide and for off-specular scattering from its coating, the exit (some 2.3 m before the sample) is chosen here. It is not possible to adjust the beam spot size with this aperture. Or positively formulated: beam-size and divergence can be manipulated independently.

This aperture has two tasks: Its opening defines the divergence of the beam incident on the sample, and its position defines the angle of incidence relative to the instrument coordinate system. The beam has a cross section of $60 \times 60\,\mathrm{mm}^2$ at the position of the aperture and it is convergent to the sample position covering a divergence of 1.5°. It is thus possible to change the angle of incidence on the sample by up to 1.5° by repositioning the aperture without rocking the sample.

In the conventional time-of-flight operation mode this feature can be used to switch between up to 4 angles of incidence much faster than by rotating sample and detector. With state of the art components the switching can be performed in less than a second, thus only a few pulses are lost.

scanning aperture In case it is possible[11] to scan the aperture across the beam within one pulse, this device will be used to perform a λ-θ-encoding: The position of the aperture in this case does not only define the angle of incidence, but also the wavelength. Depending on the scan direction (towards smaller or larger θ) on can extend or compress the q_z-range covered in one shot.[12]

2.4.3 Spin polarisation

Neutron spin polarisation and its analysis are key-features of *Estia* Based on the demand nowadays one can estimate that at least 50% of the measurements will need a polarised beam, and some 10% also polarisation analysis.

polarisation The special geometry of the beam within the guide allows to use a transmission polariser, i.e. a transparent substrate, coated with a polarising supermirror.[13] The substrate will be curved into a logarithmic spiral with the virtual source as a pole. This way each neutron trajectory intersects with the substrate at the same angle. This allows to use a low-m coating which is more efficient, and to build a shorter device, compared to a straight transmission polariser. [→7.1] A prototype of this kind of polariser was successfully tested on Amor.

The polariser will be installed in the gap after the end of the second guide section (the end of the concrete shielding). This way the off-specular scattering inherent to transmission polarisers is cut off by the diaphragm defining the virtual source. The 2 m long device can be moved in and out of the beam within a few seconds.

The long distance between polariser and sample environment ($> 24\,\mathrm{m}$) guarantees that no magnetic stray fields from a cryomagnet interfere with the polariser.

[11] If it is not possible to realise a sufficiently fast scanning system, only one out of three principle operation modes is affected. And even for this mode there exist alternative approaches. It is also possible to use a double chopper instead of the scanning aperture with almost the same performance.

[12] This can also be realised by using a multilayer monochromator, but with higher losses due to the finite reflectivity of such a device.

[13] Using ^{3}He for spin polarisation or analysis is compatible with the present design of *Estia*. It is not favoured here because of the higher maintenance and costs.

analysis The geometrical situation behind the sample is very close to the one described above: a divergent beam emerging from a small area (the sample) has to be analysed. Thus also a transmission analyser with the shape of a logarithmic spiral [→7.1] will be used.[14]

To allow for the installation of a spin flipper between sample and analyser, and to enlarge the distance to a possible source of stray fields, the device will be larger than the polariser. (The size scales with the distance from the pole.)

It will be mounted on a lift within the evacuated flight path between sample and detector, so that it can be activated within seconds.

flipper The polarisation state of the neutrons can be switched by RF flippers installed at the intermediate focal point of the second guide section ($x = 40.2\,\mathrm{m}$) for the incoming beam, and directly in front of the analyser ($x = 54\,\mathrm{m}$) for the reflected beam.

2.5 Sample stage

The sample stage is the same as for conventional reflectometers. The position of the stage on the floor might vary with the alignment and the operation mode of the instrument. This means that a *x*-*y* translation stage (or a platform on air-pads) forms the basis.

Since the sample environment can be quite heavy and voluminous, the sample stage will be able to handle weights of up to 1 t. The *free* space between the platform and the sample is at least of the order of 300 mm. In table 9.1 a possible set-up of translation and rotation devices is listed. The complete sample stage will be non-magnetic, because one principle application of this instrument will be the measurements in high magnetic fields.

The guide ending 2.4 m before the sample, and the large distance to the detector leave enough space for even bulky sample environment devices like cryomagnets. Also equipment for *in-situ* complementary measurements like UV or X-ray will find space.

sample environment *Estia* should be equipped with a series of standard sample holders (for environmental condition, in vacuum, thermalised) and with an in-situ furnace. Where possible a sample changer will increase the throughput considerably because of the short expected measurement times.

A vertical field cryomagnet ($T = 2\,\mathrm{K}$ to $300\,\mathrm{K}$, $B \leq 7\,\mathrm{T}$) has to be available (can be a pooled device). For less demanding conditions it proved to be useful on Amor to have a closed-cycle refrigerator and a fitting electromagnet at the beamline.

The sample table of *Estia* has to be flexible enough to allow for hosting user-owned special equipment, e.g. for in-situ studies (annealing or growth chambers) or for rheology.

2.6 Detector

2.6.1 Area detector

For the reflectometry measurements one position sensitive detector is needed. The technology available today (2 mm resolution, area $400 \times 400\,\mathrm{mm}^2$) would work. But higher resolution and a wider area would improve the instrument's performance. In principle, the instrument could be upgraded with a *better* detector once it is available without affecting the rest of the instrument. There is no preference for any detector technology from our side. Table 2.4 gives the (realistic) wish-list of the detector properties. [→9.2]

	state-of-the-art	ideal parameters
size	$400 \times 400\,\mathrm{mm}^2$	$500 \times 170\,\mathrm{mm}^2$
resolution horizontal	2 mm	≤ 0.5 mm
resolution vertical[15]	2 mm	≥ 1 mm
instant rate at 5 Å		$5 \cdot 10^8\,\mathrm{s}^{-1}\mathrm{Å}^{-1}$
at 9.4 Å		$2 \cdot 10^8\,\mathrm{s}^{-1}\mathrm{Å}^{-1}$

Table 2.4: Key parameters for the area detector. The numbers of the state-of-the-art detector were given by R. Hall-Wilton, ESS. ($\Delta\lambda \approx 0.2$ Å)

[14] For spin analysis also a multi-channel bender could be installed directly in front of the detector. Similar devices are in operation at FOCUS@PSI and at HYSPEC@SNS. These are more compact than the proposed model, but the stacking of the substrates leads to a reduced transmission.

[15] Unless used for GISANS, the detector could be integrating vertically, i.e. no spatial resolution would be required

2.6.2 Single detector

For diffraction measurements on the films or the substrates a second (single) detector on a shorter 2θ arm might be used. This possibility proved to be useful e.g. to check possible bending or twinning of the substrate upon cooling.

2.6.3 CCD camera

To align the guide and to monitor its performance, and also for aligning the sample, a CCD camera in front of the area detector can be used. This has the advantage that its resolution is much higher, while its draw-backs of high noise and low efficiency do not play a role for this purpose.

The active area should be some $150 \times 150\,\mathrm{mm}^2$, the resolution about $0.1 \times 0.1\,\mathrm{mm}^2$.

2.7 Shielding

An advantage of using two *Selene* guide sections is that the heavy shielding is concentrated before and around the first guide section. The second *Selene* guide section will also need some shielding, but since neither thermal or fast neutrons, nor γ-radiation should reach this region, only a moderate boron-based absorber should be sufficient. Figure 2.6 shows the shielding concept for the first *Selene* guide section including the target monolith. The individual components are discussed below.

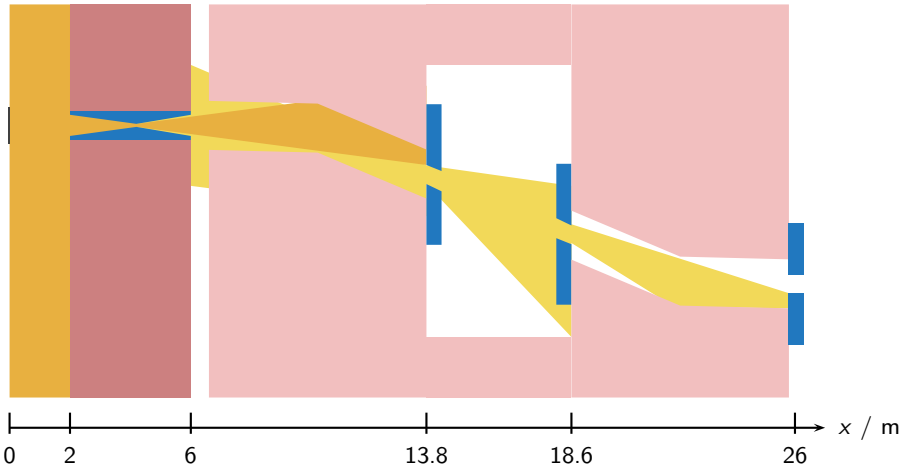

Figure 2.6: Sketch of the fast neutron and γ shielding concept. Here a vertical cut through the shielding is shown, following the beam in horizontal direction. The guide geometry and thus the shielding is the same horizontally and vertically. The source (moderator) is represented by the dark gray rectangle on the left. The red area stands for the monolith, the blue insert is the extraction unit. The pale red area represents heavy concrete shielding (or a sandwich of various moderators and absorbers), which hosts the guide elements. Additional masks (here blue) are needed to block the opening outside the neutron beam path. The area directly illuminated from the source is shaded yellow, the indirectly illuminated area is pale yellow. The neutron guides are not shown.

2.7.1 Beam extraction

Within the first 6 m the only *optics* needed is a pin-hole at $x = 4.2\,\mathrm{m}$ acting as a virtual source for the first *Selene* guide section. The location is chosen to accept the required divergence of $\Delta\theta = 1.5°$ from the $120 \times 120\,\mathrm{mm}^2$ wide moderator. The extraction insert consists of some highly γ and neutron absorbing material (e.g. copper).

To take the expected settling of the ground into account, the pin-hole size can be increased. The *Selene* guide will still pick up about the same phase space volume, but the radiation shielding gets weaker. This has to be compensated for by increased shielding along the beam guide.

There is no restriction when it comes to including a maintenance shutter in the monolith or in the extraction insert at any position.

Behind the monolith there is a gap of 600 mm until the first guide starts. Unless used for filters or a shutter, this gap can be filled by an extension of the insert.

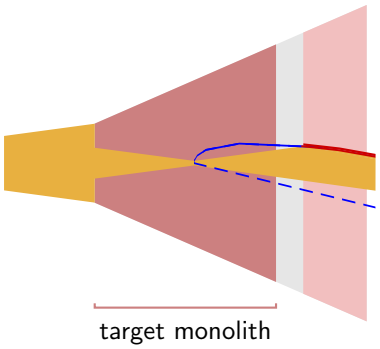

Figure 2.7: Sketch of the beam extraction section with a pin hole. A small ($10 \times 10\,\mathrm{mm}^2$) aperture 4.2 m from the moderator defines the initial focal point for the first *Selene* guide section. This position allows for a divergence of $\Delta\theta_{xy} = \Delta\theta_{xz} = 1.5°$. The openings of the flight path section are 68 mm / 58 mm at the entrance / exit of the target monolith.

2.7.2 First guide section: common and individual instrument shielding

It is inherent to the *Selene* guide concept that neutrons are reflected on each reflector exactly once, so that the complete beam has changed its direction when leaving a guide segment. This means that within each segment one gets out of line of sight from its initial focal point. The guide dimensions and the wide free spaces before and behind the segments enable efficient shielding. Thus after the second segment one is out of line of sight twice with respect to the moderator and its environment, as is required by the ESS [→8.2]. There is space for a vacuum housing and mounting equipment around the guide. The guides' open construction (it forms an L, rather than a rectangle) allows for a tight shielding on two sides, the support mechanics can be mounted on the other sides.

The first and second guide elements are enclosed in a heavy concrete block. In the sketch at least 50 mm free space between guide and shielding are assumed for support, alignment devices, and vacuum housing. Because the dimensions of the openings are about 3 times the actual guide width, additional shielding is needed before and after the concrete shielding. These masks are supposed to consist of copper (displayed in blue). The area directly irradiated from target and moderator ends at the exit of the first concrete block at $x = 13\,800$ mm. This is still withing the common instrument shielding, reaching up to $x = 15\,000$ mm. The indirectly irradiated area ends at $x = 25\,800$ mm, i.e. less than half way between source and detector. In the gap $x \in [14, 18]$ m the instrument shutter (see below) and a frame overlap chopper will be installed, again surrounded by a concrete shielding.

The support system for the guides needs more space than just the $160 \times 160\,\mathrm{mm}^2$ within the channel. Swiss-Neutronics suggested to use a granite beam to support the guide. This could also be part of the shielding, with appropriate shape to prevent straight holes parallel to the channel. Whether granite is suited for this purpose has to be investigated. On the other side, one could use a heavy concrete beam as support if it is stable enough also against thermal influences.

2.7.3 Apertures within guides

To block the direct line of sight through the *Selene* guide sections, one-sided apertures are positioned at the centres of each section. These apertures ensure that each transmitted neutron is reflected once for each direction (horizontally and vertically). The opening of these apertures is fix. The ones in the first segments will be quite heavy because they have to also block fast neutrons and γ-radiation. In figure 2.2 these apertures are depicted in gray.

2.7.4 Shutter

A service shutter can be installed within or right behind the target monolith.

In addition an instrument shutter will be placed in the gap between the first and the second guide segments. This region is already out of line of sight from the moderator, so that only secondary radiation and cold neutrons transported by the guide have to be blocked. Once closed,this shutter allows access to all the area behind the end of the second guide segment, i.e. from 26 m onward.

2.7.5 MCNPX simulations

Based on the model given in figure 2.6 MCNPX simulations have been performed by U. Filges, PSI. The results are summarised in table 2.5. These show that the proposed geometry and dimension of the *Selene* guide allows for a shielding which fulfils the requirements by the ESS. Just outside direct line of sight the dose rate is $37\,\mu\mathrm{Sv h}^{-1}$, and it drops below the computational threshold at the end of the shielding.[16]

[16] The simulations took 7 days on a cluster with 7×24 cores.

position	x/ m	y/z position	dose rate / μSv h^{-1} γ	dose rate / μSv h^{-1} neutron	flux / s^{-1}cm^{-2} neutron	error
exit common shielding	14.5	in beam	37	78 000	$9.3 \cdot 10^4$	7%
		off beam	37	10 000	$1.6 \cdot 10^4$	7%
entry instrument shielding	18.1		8	1 400	$2.5 \cdot 10^3$	20%
exit instrument shielding	26.5	in beam	–	–	–	–
		off beam	–	–	–	–
5 m behind shielding	31.5	in beam	–	–	–	–

Table 2.5: Dose rates and flux calculated with MCNPX for various positions along the guide. The source was assumed to be continuous with a power of 5 MW. This means that the peak dose and flux are a factor 30 higher. The computational statistics was too low for the positions marked with –.

2.8 Operation modes

In figure 2.8 the three principle operation modes are sketched, and the corresponding λ-θ detector diagrams are shown. A short description is given below, and an extensive discussion including data acquisition and reduction is given in the appendix [→10].

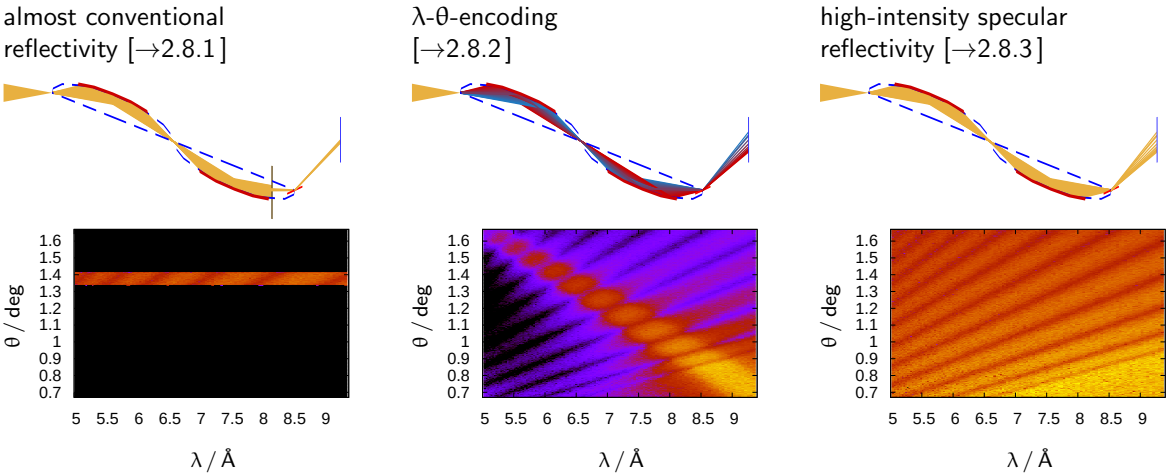

Figure 2.8: Operation schemes and $I(\theta, \lambda)$ maps obtained by simulation [→2.9] assuming a 1000 Å thick Ni film on glass as sample: using an aperture behind the guide, using a multilayer monochromator for angle-wavelength-encoding, and using full divergence and pulse. Only the second *Selene* guide section is shown. For more details see section 2.8.4

2.8.1 Almost conventional & off-specular reflectivity

[→10.2] Though still giving a convergent beam to the sample, this mode is quite close to the operation scheme of conventional TOF reflectometers. An aperture 2.2 m before the sample defines the divergence $\Delta\theta$. The wavelength is obtained by the time-of-flight, and θ is adjusted by rocking the sample. The λ resolution is given by the pulse length and varies from 2.2% (9.4 Å) to 4% (5 Å).

The beam footprint is defined by the virtual source at $x = 28.2$ m. Over-illumination of the sample and illumination of the sample environment can be suppressed.

By moving the divergence-defining aperture within the θ-range of the beam leaving the guide, one can change θ_i without tilting the sample.

Figure 2.9 shows intensity maps (left), and the reflectivity curve extracted therefrom (right). These data were obtained by simulation.

This mode will be needed to align the sample, and for measuring (or discriminating) off-specular scattering.

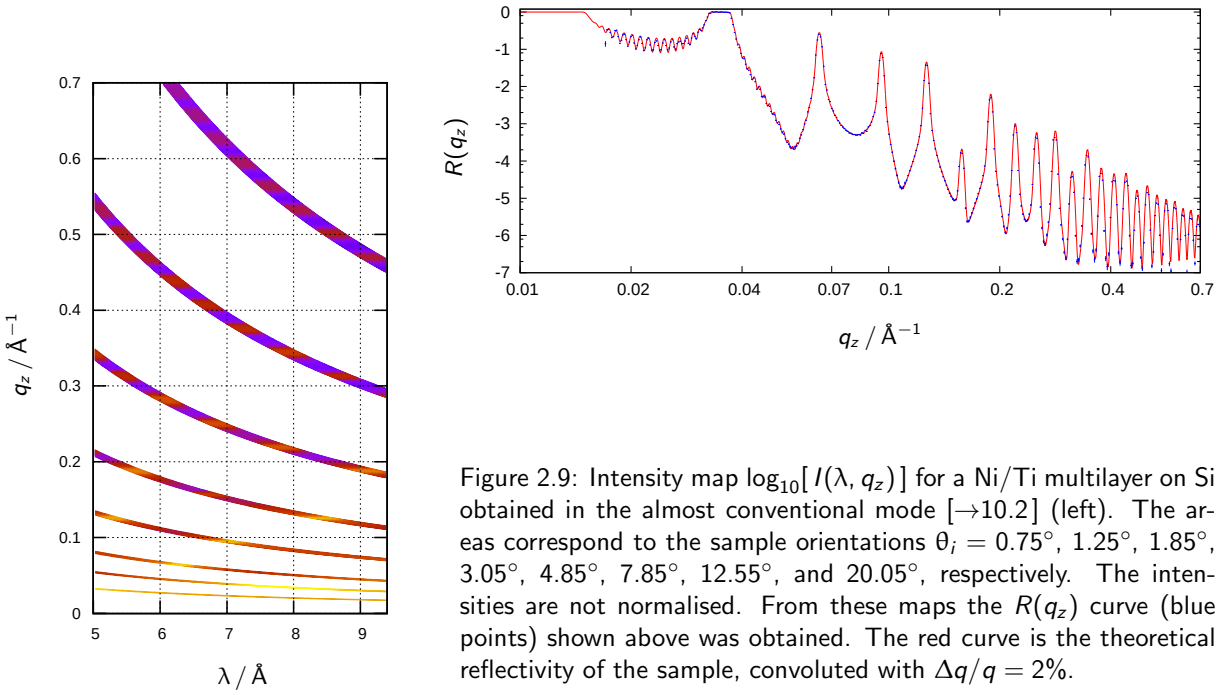

Figure 2.9: Intensity map $\log_{10}[I(\lambda, q_z)]$ for a Ni/Ti multilayer on Si obtained in the almost conventional mode [→10.2] (left). The areas correspond to the sample orientations $\theta_i = 0.75°$, 1.25°, 1.85°, 3.05°, 4.85°, 7.85°, 12.55°, and 20.05°, respectively. The intensities are not normalised. From these maps the $R(q_z)$ curve (blue points) shown above was obtained. The red curve is the theoretical reflectivity of the sample, convoluted with $\Delta q/q = 2\%$.

off-specular scattering In this mode off-specular scattering can be measured exactly in the same way as on conventional TOF reflectometers. Without using pulse shaping choppers the q_z resolution is essentially given by $\Delta\lambda \propto \tau$. The q_x resolution varies strongly as a function of λ and θ_f.

2.8.2 Angle-energy-encoding

[→10.3] Compared to the almost conventional mode there are two essential differences: It allows coverage of a wider q_z-range in one shot by relating λ_{max} to small θ and λ_{min} to large θ. And while λ is encoded in θ, it has the resolution $\Delta\lambda/\lambda = \Delta\theta/\theta$. This means that the resolution can be manipulated without pulse shaping, so no choppers are needed.

The encoding is achieved by using a (double bounce) multilayer monochromator before $x = 28.2\,\text{m}$. To get a clean beam, a scanning aperture 2.2 m before the sample is necessary to scan θ within one pulse.

Figure 2.10 shows intensity maps obtained by simulation for this operation scheme.

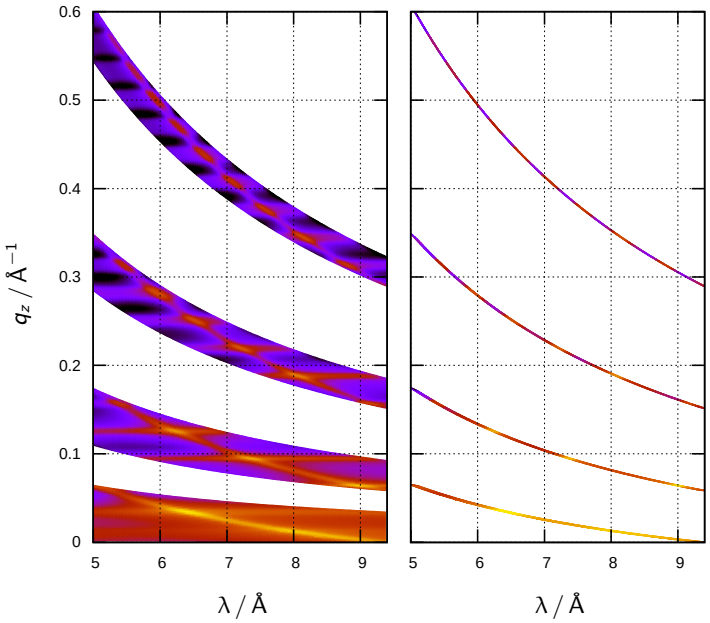

Figure 2.10: Intensity map $\log_{10}[I(\lambda, q_z)]$ for a Ni/Ti multilayer on Si obtained in the λ/θ-encoding mode [→10.3]. The 4 areas correspond to the sample orientations $\omega = -0,5°$, 2°, 6°, and 12°, respectively. The intensities are not normalised. The left maps show the signal after transformation of t to λ and θ to q_z. In the maps on the right side the areas where only off-specular intensity is expected (assuming a perfect monochromator) are shaded. Comparison to figure 2.9 illustrates the reduction of sample orientations needed to cover a given q_z-range.

off-specular scattering Also in this mode off-specular scattering can be measured. Since the specular scattering occupies the diagonal of the λ-θ diagram, the off-specular *area* consist of two triangles. The q_z resolution is almost constant, the q_x resolution varies strongly as a function of λ. Figure 2.11 compares the q_x-q_z area covered by the almost conventional and the λ-θ-encoding mode.

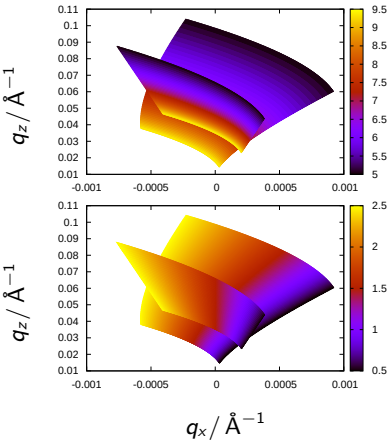

Figure 2.11: q-space covered by off-specular measurements in the λ-θ-encoding mode (larger area) and in the almost conventional mode (smaller, more distorted area). In the top map, λ and in the bottom map θ is plotted as a function of q_x and q_z. The detector was assumed to cover $\theta_f = 0.5°$ to 2.5°, and $\theta_i = 1.5°$ in the conventional mode.

accuracy In the λ-θ-encoding mode it is essential that the reduction of the λ-resolution induced by angular error is below the desired $\Delta\lambda/\lambda$. The encoding is given by $\lambda = 4\pi \sin(\theta_s + \omega_m - \omega_s)/q_m$ with the coating of the monochromator having a Bragg peak at q_m, and the monochromator and sample angles $\omega_{m/s}$. An angular error $\Delta\alpha$ caused by a misaligned guide or by waviness leads to a wrong θ and thus to $\Delta\lambda \approx 4\pi \sin\Delta\alpha/q_m$. If the angular error is so large that the beam misses the sample, the error does not cause a reduction of the resolution, but it just leads to a reduction of the reflected intensity.

For a 10 mm long sample and $\omega_s = 10°$ the projected sample height is ≈ 2 mm. This corresponds to angular errors of 0.006° to 0.025° along the last guide segment, and thus to $\Delta\lambda < 0.02$ Å. This can be neglected. So in most cases an imperfect guide will result in a reduced intensity on the detector (the dark lines seen with the prototype set-up), but the encoding is still valid.

2.8.3 High-intensity specular reflectometry

[→10.4] This is the operation mode which delivers the most flux to the sample. The full divergence and also the full wavelength band accepted by the instrument are used. The wavelength is encoded in the time of flight, and thus the resolution is given by the pulse length of the source. The angular resolution is determined by the spatial detector resolution and the sample-to-detector distance.

The measured signal on the position sensitive detector is a $I(t, z)$ map which can be transformed into a $I(\lambda, \theta)$ map. Each row corresponds to a TOF measurement at a given θ, and each column corresponds to an angle dispersive measurement for a given λ. This means that one combines the two conventional reflectometry set-ups to increase the specularly reflected intensity. [1] However, a disentangling of an off-specular signal is a challenge.

Figure 2.12 shows an intensity map obtained by simulation, which illustrates the principle and the flux gain of this mode.

Thus this mode can be used
– on tiny samples where one is satisfied if some reflectivity curve can be obtained in a reasonable time,
– on samples with negligible off-specular or incoherent scattering,
– to screen the dependence of $R(q_z)$ on temperature, electric or magnetic fields, surface tension, or the like, and
– to perform time-resolved measurements on a split-second time scale.

There is no simple answer to the question of how much off-specular scattering from the sample itself, from the optical elements, or scattering from the sample environment affect the measurements. But it is no problem to check this whenever necessary: A comparison of $R(q_z)$ obtained in the almost conventional mode (achieved by just closing an aperture) and in the high-intensity mode immediately shows how strong the influences are.

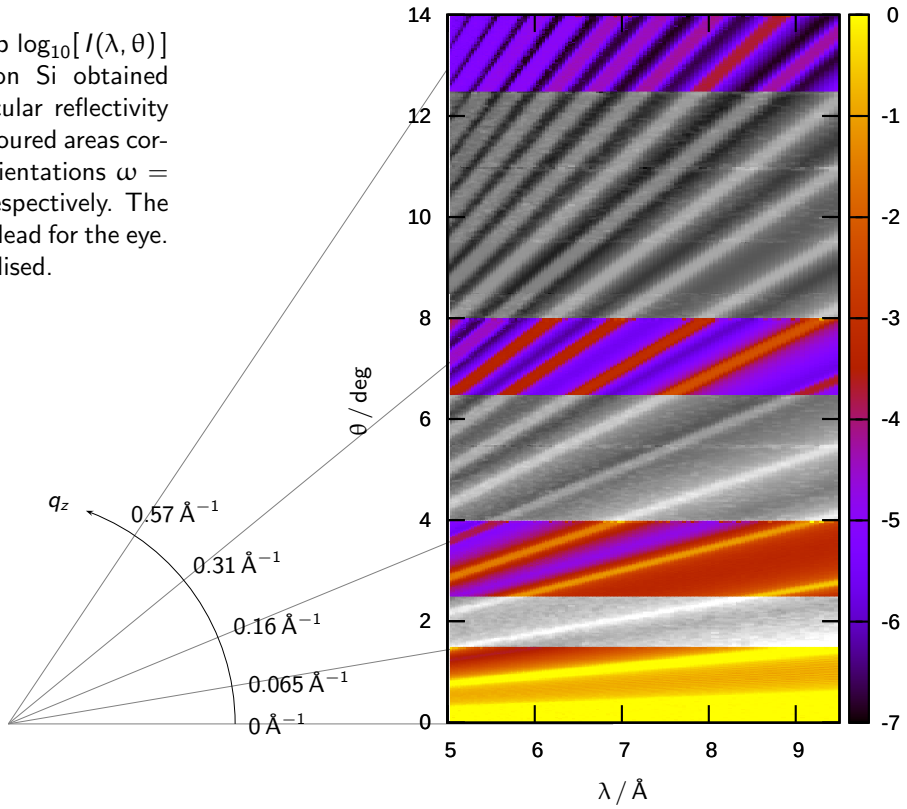

Figure 2.12: Intensity map $\log_{10}[I(\lambda,\theta)]$ for a Ni/Ti multilayer on Si obtained in the high-intensity specular reflectivity mode [→10.4]. The 4 coloured areas correspond to the sample orientations $\omega = -0, 5°, 2°, 6°$, and 12°, respectively. The gray-scale areas are just a lead for the eye. The intensities are normalised.

2.8.4 Comparison

Figure 2.8 shows sketches of the main operation modes and the corresponding $I(\lambda,\theta)$ maps as obtained with a 1000 Å Ni film on Si as a sample. The sample size was $5 \times 5\,\mathrm{mm}^2$.

a) λ-θ-encoding [→2.8.2] by using a ML monochromator after the beam extraction.

   This results in a diagonal streak in the λ/θ space, where $\Delta\lambda/\lambda = \Delta\theta/\theta = \text{const}$. In the off-diagonal region the finite reflectivity of the ML monochromator leads to some structured background. This does not affect the specular reflectivity, but it might prohibit off-specular measurements.

b) High-intensity specular reflectometry [→2.8.3] by substituting the ML monochromator by a supermirror.

   Here all of the available λ/θ space is used for specular reflectometry. Off-specular and incoherent scattering leads to an enhanced background. This mode allows for a fast (and dirty) screening of external parameters as e.g. temperature or magnetic field strength, and for time-resolved studies.

c) Almost conventional reflectometry [→2.8.1] by using an aperture to cut down the divergence given by the set-up (b).

   The specular reflectivity concentrates on one line, while the rest of the λ/θ space is available for off-specular measurements. The q_z-range accessible this way is reduced. A movement of the aperture between pulses can be used to vary θ without tilting the sample.

From these maps from a second set for a higher angle the reflectivity curves shown in figure 2.13 were obtained by integrating the λ/θ maps along constant q_z. The binning was done with $\Delta q_z/q_z = 1\%$. The error-bars shown were obtained by assuming $\Delta I/I = \sqrt{I}$ where I is the flux given by the simulation, multiplied by a

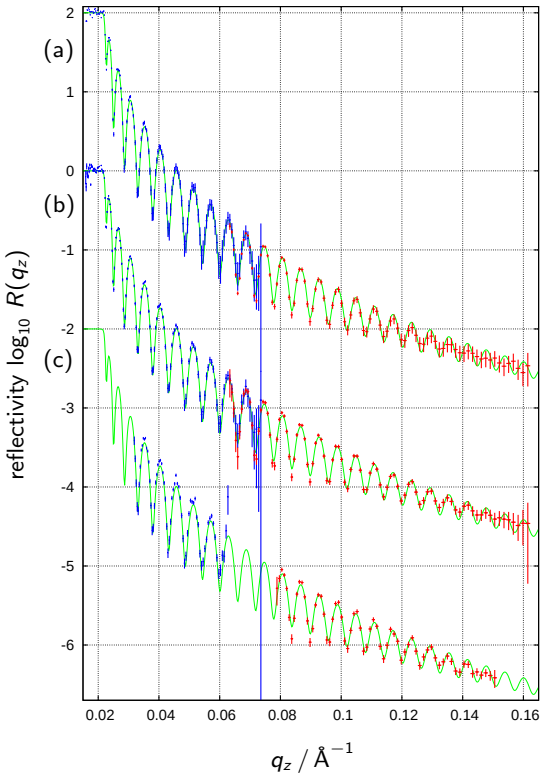

Figure 2.13: Comparison of the performance of the three basic operation modes. Shown are the reflectivities $R(q_z)$ extracted from the maps shown in figure 2.8 ($\omega = 2°$, blue) and from the corresponding maps for a higher angle ($\omega = 4°$, red).
The corresponding modes are:

	mode	ω	t
(a)	λ-θ-encoding with	2°	60 s
	$\Delta\lambda/\lambda = 3.5\%$	4°	900 s
(b)	high-intensity specular	2°	1 s
	reflectivity	4°	10 s
(c)	almost conventional set-up	2°	10 s
	with $\Delta\theta/\theta = 4\%$	4°	100 s

The curves are scaled by $10^2, 10^0, 10^{-2}$ for clarity. The green curves correspond to the initial reflectivity with $\Delta q/q = 2.4\%$. The covered q_z-range and the resolution functions depend on the measurement scheme. The *measurement times* t were chosen to get comparable error bars.

measurement time t. For the high-intensity specular reflectivity at the lowest angle $t = 1$ s was chosen, the other values were adjusted to get comparable accuracy.

The graphs in figure 2.13 tell that the high-intensity mode and the λ-θ-encoding mode cover the same q_z-range, while for the conventional mode it is only half or two third, depending on ω. A comparison of the counting times tells that the high-intensity mode is about one order of magnitude faster than the conventional mode for the same accuracy in the overlapping q_z interval. The encoding mode is another order of magnitude slower due to the losses from the monochromators and the higher resolution.

2.8.5 Further options

focusing SANS The fact that the *Selene* guide gives a strongly focused beam can be directly used for setting up a focusing small angle scattering scheme. A detector has to be placed in the focal plane (where otherwise the sample is located), and the sample is positioned behind the guide end, some 2 m before the detector. This set-up gives an angular resolution of $\approx 0.03°$. The sample size can be up to $52 \times 52\,\text{mm}^2$ (using the full divergence of 1.5° and the minimum resolution).

GISANS There are two principle modes of how GISANS could be realised on *Estia*. One can convert the beam focused to the sample into a beam focused onto the detector by using a hyperbolic reflector [→7.3]. This concept can be applied in the sample plane and in the specular scattering plane independently. The divergence of this beam is defined by the size of the virtual source. The width of the beam depends on the distance of the reflector from the focal point and can thus be tuned.

B. Hjörvarsson suggested another approach: Using the beam convergent to the sample for GISANS results in a convolution of the detector image with the angular resolution function. While this is constant for all λ, the GISANS map on the detector scales with $1/\lambda$. Using the TOF data and the known resolution function should thus allow for a rather precise deconvolution of the detector image. Since the divergence of the incoming beam can be modified in both directions independently, one can tune the resolution function.

MIEZE A group at TUM including R. Georgii, W. Häußler and G. Brandl investigates the possibility to use a *Selene* type guide system for a dedicated MIEZE (Modulation of IntEnsity by Zero Effort) instrument.[25] Their know-how can be used to develop an add-on MIEZE set-up for the proposed instrument. The coils can

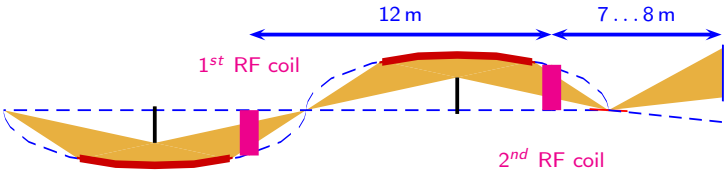

Figure 2.14: Sketch to illustrate the combination of MIEZE and a *Selene* guide. (On *Estia* only the second guide section would be used.)

be located before the third or fourth guide segment, and before the sample. The elliptic shape of the guide guarantees the same length for all trajectories. Figure 2.14 illustrates the short version of the MIEZE set-up.

2.9 Simulations

The *Selene* guide concept and the basic design of *Estia* were developed on the basis of analytic calculations. In a later stage also Monte Carlo simulations with the software package McStas [26, 27] were performed to

- independently verify the results of the analytic calculations [→tab. 2.1];
- check the influence of gravity [→6.4];
- estimate the performance of the operation modes, including the development of a data reduction scheme [→2.8.4];
- estimate the influence of misalignment of the guide(elements) [→3.1]; and to
- provide a reference for comparison with other reflectometer concepts [→11].

Details for the latter are given in appendix 11. The essential results of this simulation are given in table 2.6. The reference sample is a silicon wafer of 1 cm^2 with a oxide layer on top. An artificial background of 10^{-7} was used to estimate the measurement time for high q_z. The reflectivity drops below that background level at $q_z \approx 0.32\,\text{Å}^{-1}$ so that the measurement time to reach the required statistical accuracy in the range $q_z \in [0.32, 0.35]\,\text{Å}^{-1}$ grows exponentially. Depending on the operation mode 90% to 99% of the total counting time has to be spent for this interval.[17]

The results of the other simulations are given in the respective sections throughout this proposal and the appendices.

2.10 Performance

The instrument's performance is governed by the design of the neutron guide. The truly focusing leads to a well-defined and clean beam, and to a low background. But it also leads to restrictions concerning maximum spot-size, or brilliance transfer. In the following these aspects are discussed in detail.

[17] The obtained counting times are not representative for a real experiment, because nobody would measure a feature-less profile like this with such a high resolution and accuracy. And a reflectivity curve with more structure can be assumed to have a higher reflectivity.

mode	$q_z \in [0.05, 0.30]\,\text{Å}^{-1}$		$q_z \in [0.05, 0.35]\,\text{Å}^{-1}$	
	settings	time	settings	time
conventional[†]	4+3	26 min	4+4	4.6 h
λ-θ-encoding	3	22 min	4	7.3 h
high-intensity	3	4 min	4	1.8 h
	5	1 min	4	1.2 h

[†] The 4 lowest settings can be realised by moving the aperture rather than sample and detector.

Table 2.6: Counting times needed to reach a relative error below 14% for each bin with $\Delta q_z/q_z = 1\%$ for the three main operation modes of *Estia* for a Si/SiO$_2$ sample of 1 cm^2 area. The number in the *settings* column tells how many sample orientations were needed to cover the respective q_z-range.

sample size The beam-spot will have a maximum width of 10 mm. The spot length is not restricted, but it influences the achievable resolution. A reasonable upper footprint size is $10 \times 50\,\mathrm{mm}^2$. The majority of the solid state samples studied today fit to these parameters. All wider samples (of high homogeneity) are not optimally exploited.

The minimum footprint size is about $1 \times 1\,\mathrm{mm}^2$, limited by the optical perfection of the guide and unavoidable aberration. But even samples with an area of $0.3 \times 0.3\,\mathrm{mm}^2$ can be measured up to $q_z = 0.2\,\text{Å}^{-1}$ within approximately 4 h.

The focusing allows to define the footprint far from the sample and thus no slit or other optical element is needed close to the sample. Bulky sample environment or high magnetic fields are no obstacle for precise beam definition.

q_z-range A maximum $q_z > 2\,\text{Å}^{-1}$ can be reached with a detector angle of 120°. For reflectometry measurements this is too high (there are hardly any samples which allow for $1\,\text{Å}^{-1}$), but it enables to measure crystal Bragg peaks of the substrate or the film (with $d > 3\,\text{Å}$).

The most interesting region $q_z \in [0.005, 0.5]\,\text{Å}^{-1}$ can be covered with 4 orientations of the sample.

resolution The intrinsic instrument resolution is below 5%, which fits for 90% of the experiments. Since the full pulse is already used, a lower resolution will not result in shorter counting times or better statistics. Only if $\Delta q_z/q_z < 5\%$ is required one has to trade intensity for resolution. $\Delta q_z/q_z = 1\%$ or 2% can be realised by λ-θ-encoding. For very small q_z the detector resolution will dominate and set a limit.

background It is impossible to calculate the actual background, and thus the dynamic range. During the design process of the instrument and the measurement schemes, care was taken to reduce the background as much as possible.

One big advantage of the *Selene* guide system is that it transports much less neutrons compared to other guides. This and the focusing to the sample leads to a lower background and to a reduced illumination of the sample environment. Each *Selene* guide section avoids direct line of sight twice, i.e. already after half the guide length the ESS criteria are matched. Thus most probably, *Estia* will have a much lower fast neutron background than all other instruments.

In addition, the time-intervals of the proton pulse are not used for data acquisition, neither in the monitor nor in the detector.

Focusing on the detector rather than on the sample in the sample plane can be used to reduce the influence of sample-intrinsic background by more than an order of magnitude for relatively wide surfaces.

polarisation The spin-polarisation is performed (optionally) far from the sample so that it will not interfere with its magnetic environment. For spin-analysis the distances to the sample are shorter, but still large compared to present days reflectometers.

counting time The counting time is limited by the brilliance transfer of the guide system, and by the fraction of the neutron pulse used for measurements. The *Selene* guide system has in general a lower transmittance than ballistic guides. On *Estia* a further decrease of the beam intensity is taken into account because of using two *Selene* sections to reduce the fast neutron background. These losses are partly compensated for by focusing on the *hot area* of the moderator (giving a gain of some 30%).

Estia will out-perform any existing reflectometer independent of the sample size. For surfaces area $10 \times 50\,\mathrm{mm}^2$ the gain in the conventional mode is approximately a factor 30, increasing with shrinking size.[18] An other order of magnitude can be expected for specular measurements for the high-intensity mode. Below are given the estimates for three selected examples:

- A normal polarised reflectivity measurement on a $1\,\mathrm{cm}^2$ sample with $\Delta q_z/q_z = 5\%$, $q_z \in [0.01, 0.3]\,\text{Å}^{-1}$ takes 10 min per spin state (conventional or λ-θ-encoding mode).
- The same sample and resolution but $q_z \in [0.01, 0.08]\,\text{Å}^{-1}$ can be measured by using one pulse only, which allows for spit-second time resolution (high-intensity mode).
- A polarised reflectivity measurement on a $1\,\mathrm{mm}^2$ sample with $\Delta q_z/q_z = 5\%$ and $q_z \in [0.01, 0.3]\,\text{Å}^{-1}$ in the high-intensity mode takes 40 min per spin state.

[18] The reason is the higher brilliance transfer of a *Selene* guide for smaller beam cross sections.

flexibility In the basic configuration allowing for specular and off-specular (polarised) reflectometry, *Estia* has wide *gaps* along the neutron path. This means that besides a (evacuated) flight tube there is no guide or optical element. Without compromising the design or performance, these gaps can be used for

- bulky sample environment and for combination with equipment for in-situ studies;
- insertion of spin-echo options;
- refocusing the beam to the detector (for GISANS or low-background measurements); and
- upcoming concepts.

upgrade options *Det er svært at spå, især om fremtiden.*[19]
The mentioned flexibility also provides the possibility for future add-ons. Furthermore the individual building blocks of *Estia*, i.e. the virtual source, the second *Selene* guide, sample stage, and detector are widely independent and thus can be upgraded or replaced easily when new concepts require modifications.

For example it is possible to access liquid surfaces (from above and below) by using a deflector behind the guide. This requires a sufficiently flexible sample stage and the possibility to move the detector vertically.[20]

2.11 Design options

The instrument design and its properties as presented above are obtained by following the ESS baseline parameters for the moderator size and emission characteristics, the available space (and restricted area), and radiation issues (e.g. to be out of line of sight twice). It was also attempted to meet the requests and suggestions given by the STAP, e.g. not to measure during the prompt pulse.

If some of these constrains vary, or if the science case changes (larger samples, wider instant q_z-range, no high resolution, ...), it is possible to adapt the instrument concept.

small moderator The recently discussed *pan-cake* moderator with a higher brilliance can be easily used by skipping the pin-hole in the extraction unit and using the moderator itself as a focal point. The brilliance gain can be entirely used to reduce the measurement time.[21] The only price one has to pay is an increased shielding of the first guide section.

sample size Larger samples are accessible with a changed shape of the ellipses - on the cost of divergence or intensity.

vertical scattering plane The guide as presented does not give a preference for horizontal or vertical scattering geometry as the beam at the sample position is convergent with the same divergence in both directions. A slightly modified sample stage and a vertically movable detector enable a vertical scattering geometry. To access liquid surfaces the beam also has to be reflected downwards (or upwards).

shorter wavelengths If a gap in the TOF-data due to the prompt pulse time can be accepted (in the conventional mode), it is possible to reduce the instrument length, and thus to increase the wavelength band and lower λ_{min}. This would result in a wider q_z-range and a higher intensity. In the high-intensity mode and when using the scanning aperture for λ-θ-encoding a gap in q_z can be avoided.

short instrument Using a feeder section, followed by only one *Selene* guide section for a much shorter instrument would increase the brilliance transfer and the q_z-range for one angular setting considerably. But beam manipulation (polarisation, virtual source) would have to be performed within the shielding.

[19] *Prediction is very difficult, especially about the future.* Assigned to Niels Bohr, Winston Churchill, Karl Valentin and others. Most likely going back to some danish politician.

[20] This would be no alternative to the optimised liquids reflectometer because of the lower performance of *Estia* with respect to acceptable sample size, and simultaneous and total q_z-ranges (the latter is restricted by the deflector). Nevertheless it might be interesting some day for special applications, e.g. for liquid/liquid interfaces under high pressure.

[21] This has been confirmed by McStas simulations.

single Selene guide There are two main reasons why *Estia* uses two subsequent *Selene* guides: the recommendation not to measure during the prompt pulse, and the easy access to the virtual source. In parallel an instrument concept with only one *Selene* guide was developed. That instrument is much shorter and thus covers a wider q_z-range. Its guide system has a higher brilliance transfer. The diaphragm defining the virtual source is placed within the extraction unit unless the moderator height drops below 5 cm. In that case no virtual source can be used and the *Selene* guide focuses to the moderator directly. A precise definition of the beam footprint on the sample then is no longer possible.

The intrinsic resolution raises to 4% to 8%, which means that the λ-θ-encoding mode becomes more important because it can be used to achieve $\Delta\lambda/\lambda = \text{const}$. In this case a part of the flux gain of the shorter instrument is lost again.

3 Technical Maturity

3.1 Guide system

The biggest challenge of the presented instrument is the long-term stability of the *Selene* guide alignment. It is relatively straight forward to set up and align the individual components, as long as one has full access. Once buried under concrete and activated, this is no longer the case for the 1st guide section.

A misalignment of the 1st guide section as a whole can be accepted if the pin-hole in the extraction unit is large enough to act as a virtual source also for the tilted or shifted guide. This means that an off-set of several cm or an inclination of up to 0.2° can be accepted. Thus a settling of the target monolith with respect to the guide hall does not impose a problem.

The misalignment of individual components is easy to trace, but not so easy to correct. A solution would be to put all components on actuators. But this would result in ≈ 150 degrees of freedom — which is essentially a costing problem. The realignment with these actuators is possible by using light optics or interferometry and an adapted computer algorithm. Tests to align the prototype elements with an interferometer were performed successfully at the SLS metrology lab.

P. Böni, SwissNeutronics, suggested to mount all individual mirror elements of one guide segment (7.2 m long) on a rigid support (steel or granite beam). He claims that no realignment would be needed within this unit later on. The 4 guide segments then have to be adjustable with regard to the moderator and pin-hole, and relative to each other. This results in 24 degrees of freedom in total (position and orientation of each segment).

A comparison with the accuracy and stability required for the elements of the ESS linear accelerator, or at a synchrotron beam line tells that the technology to keep the *Selene* guide aligned is available.

guide accuracy The angular accuracy needed for the guide alignment can be estimated by looking at the longest free flight path before the sample. This is the trajectory from the entrance of the last guide segment to the sample. A beam off-set of 0.1 mm at the sample position corresponds to an angular error of 0.1 mm/9600 mm $\approx 10^{-5}$ rad. The waviness of a state-of-the-art float glass guide is of the order $2 \cdot 10^{-5}$ rad. A yz-position accuracy better than 0.1 mm can be achieved, so that this can be neglected compared to the influence of waviness.

Figure 3.1 shows the intensity distribution on the detector in y direction for a beam reflected off an ideal sample of $10 \times 10\,\mathrm{mm}^2$ for various guide building blocks being misaligned. This tells that a position error of 0.1 mm has about the same effect as a rotational misalignment of 0.001° ($\approx 2 \cdot 10^{-5}$ rad). The latter corresponds to the waviness of a brilliant state-of-the-art neutron guide. This means that the limiting factor is rather the waviness than the guide alignment. From the simulations it can be deduced that the main features of a misaligned guide are due to the discontinuities at the ends of the building blocks. This means that a misaligned, but continuous guide surface should perform better than individually misaligned parts. This has to be investigated further.

monitoring The geometry of the *Selene* guide allows for a relative simple monitoring of the guide alignment. A point-like white light source (e.g. a LED) at the initial focal point of one segment should ideally produce a homogeneous rectangular image on a screen behind the final focal point. Any deviation of the guide surface from the exact elliptic profile leads to a redistribution of the intensity on the screen. Since there is a unique relation of any point on the screen to a certain beam trajectory, it is possible to trace an intensity drop back to the part of the guide which is misaligned. For the first guide section, which can not be monitored with optical light[1] one can use a pin-hole at the final focal point and use the neutron beam itself.

[1] The light source would have to be located in an early part of the beam extraction unit and coupled into the neutron beam.

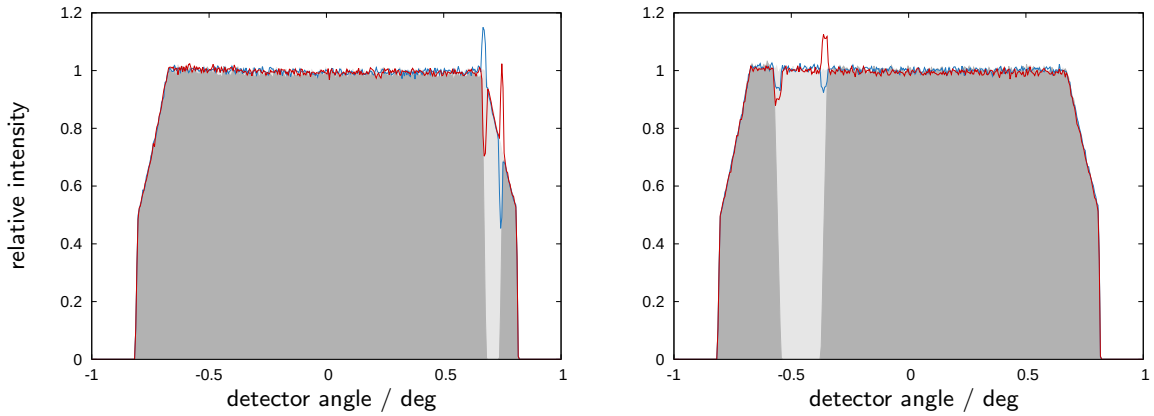

Figure 3.1: Intensity distribution on the detector in y direction of a beam reflected off a perfect sample of $10 \times 10\,\mathrm{mm}^2$. The total shaded area corresponds to the perfectly aligned guide. The light gray shaded areas correspond to intensity losses when the second (left), and the next-to-last 500 mm long building block (right) of the last segment of the guide were *removed*, respectively. The solid lines correspond to shifting each building block by 0.1 mm (red), and by rotating it by 0.001° (blue), respectively.

By coupling in/out the light by optical mirrors (e.g. Si wafers), this monitoring set-up can be installed permanently, allowing for fast feedback.

3.2 Optical components, polarisation

A prototype of a frame-overlap-filter / polariser working in transmission [→7.1] and the double bounce monochromator [→12.2.4] were already successfully tested at PSI.

Spin analysers using supermirror technology to cover a wide angular range or a large window are operational, e.g. at FOCUS, PSI, or at HYSPEC, SNS.

Thus no problems are expected for optical components.

3.3 Mechanics, sample stage

The mechanical support system for the sample and sample environment, and the analogue support for the virtual source are standard components. The same is true for slowly moving diaphragms, and for stages to exchange optics or insert a CCD camera.

A challenge is the support system for the 2nd *Selene* guide section. This is some 20 m long, but it has to be adjusted with respect to the virtual source with an accuracy in the sub-mm-range and an angular error well below 0.1°. Since it is expected that the heavy shielding leads to a drop of the monolith area with time, it is necessary that the guide can be realigned as a whole, without too much effort.

Similar tasks exist at Synchrotron beamlines, so that the technology is available. A survey of state-of-the-art solutions and the adaption to *Estia* will be part of the pre-construction phase.

3.4 Scanning aperture

For all operation modes an aperture behind the last guide segment is needed. For the almost conventional mode it defines the beam divergence and the angle of incidence, for all modes it helps aligning the sample. For these applications the aperture is defined by a standard slit system and does not represent a risk.

To change the angle of incidence without rotating the sample and the detector it is necessary to move the aperture in between measurements. The faster this movement is, the shorter the total measurement time gets, and thus the time-resolution increases. The data acquisition time for low q_z might be of the order of a second or less, thus the repositioning should be realised within fractions of a second. This is possible with state-of-the-art components. Further development will be needed to reach the ideal speed allowing to reposition in between two pulses within 10 ms.

This last feature is not necessary for the conventional operation mode of *Estia*, but a fast scanning aperture is one possibility to realise the λ-θ-encoding [→2.8.2]. When used to scan the beam during one pulse, both

blades must move independently and very accurately over $\approx 60\,\mathrm{mm}$ within 60 ms and reset within 10 ms. If such a device is possible to realise is not clear and will be subject to further investigations in the preconstruction phase.[2]

If it can not be realised, there are two alternative approaches:

multilayer monochromator A double bounce multilayer monochromator before the virtual source can also be used to create a λ-θ-encoding. This was tested at PSI. The disadvantage is, that off-specular scattering from the sample is contaminated with specular off-Bragg scattering from the monochromator. And insertion of the device has the consequence that the second guide section has to be translated by several cm.

double disk chopper A double disk chopper behind the *Selene* guide can be used instead of the fast scanning aperture. There the drawback is that the phasing of the chopper disks depends on the sample orientation. Changing the latter thus results in a delay between two measurements. Standardised choppers with a large radius (1 m) and slow rotation (so called *rotors*) are under development for other instruments at the ESS. For *Estia* such a rotor would run with $0.16\,\mathrm{s}^{-1}$ and the disks would have 87 openings.

Thus the fast aperture is the first choice with respect to flexibility and performance, but it is not mandatory to realise the λ-θ-encoding. Since the divergence-defining aperture as mentioned at the beginning of this section is mechanically decoupled from the rest of the instrument and easily accessible, it is possible to replace it by a fast scanning aperture at a later stage without problems.

3.5 Detector

The detector technology available nowadays can be used in principle, so that even when new detector concepts fail, the operation of the instrument is guaranteed. The limitations of present day detectors are the resolution and the accepted count rate.

In section 9.2 a wish-list of the detector properties is given together with the motivations. Besides the additional costs for a new detector, there are no principle obstacles to later replace the *day one* detector for a better one.

3.6 Computing, data analysis

The raw data will have a format of the type $I(t, y, z)$ (or the single event analogue). Simple perl scripts to normalise, integrate and re-bin the data are written for the analysis of the prototype measurements at PSI. This means that the algorithms for data analysis are available.

The situation changes when one wants to conserve all information contained in the raw data for fitting. The re-binning and integration (especially in the high-intensity mode) leads to a reduction and mixing of resolution. To overcome this, one can compare measured and simulated intensity maps, rather than curves. The challenge is then to modify the output of a simulation program (eventually supported by reference measurements), and to implement a good fitting algorithm. The fitting *by eye* is no longer possible.

[2] For comparison: 1) State-of-the-art CNC laser-cutter machines allow for positioning speeds of 20 mm/10 ms. This is only a factor 4 below the needs for the fast scanning aperture. At the same time it handles heavy loads over large distances with 4 degrees of freedom instead of one. The position accuracy is 10 µm. 2) Industry robots sorting pralines non-stop (4 axis, $\approx 1\,\mathrm{m}$ distance) realise up to 4 pics per second. This means an average travel speed of 80 mm in 10 ms. The position accuracy most likely is lower than necessary for the aperture.

4 Costing

The cost estimates for *Estia* given in table 4.1 are based on quotations, experience at PSI, and on information obtained from ESS experts. Selected justifications for the mentioned numbers are given below.

In total *Estia* will cost some 12 M€.

Table 4.1: Estimated costs for *Estia*, broken down into phases, hardware / person months (PM), and topics. One PM is assumed to cost 10 k€ in average. The phases are: **I** design and planning, **II** final design, **III** procurement and installation, and **IV** beam testing and cold commissioning. The numbers for personal were obtained from the ESS, the hardware costs from [1]ESS experts, [2]provider quotations, and [3]experience at PSI. The total cost for *Estia* will be about 12 M€without VAT. Not included here are costs for common installations and equipment as the shielding up to 15 m, chemical laboratories, and pooled sample environment.

phase		integrated design [1]	systems integration [1]	guide system [2]	optical components [2,3]	chopper / scanning aperture [1]	mechanics / motion control [1,3]	detectors [1,3]	shielding [1,3]	instrument infrastructure [1]	$\sum$
	hardware / k€	0	0	0	0	0	0	0	0	0	0
I	staff / k€	420	0	30	30	60	60	60	30	30	720
	/ PM	42	0	3	3	6	6	6	3	3	72
	hardware / k€	0	0	0	0	50	0	0	0	0	50
II	staff / k€	720	30	30	30	60	60	60	60	30	1 080
	/ PM	72	3	3	3	6	6	6	6	3	108
	hardware/ k€	0	0	1 700	600	500	1 050	1 100	3 000	300	8 250
III	staff / k€	480	120	60	60	60	240	30	60	120	1 230
	/ PM	48	12	6	6	6	24	3	6	12	123
	hardware/ k€	0	0	0	0	0	50	0	0	0	50
IV	staff / k€	240	60	10	30	30	30	30	60	30	520
	/ PM	24	6	1	3	3	3	3	6	3	52
	hardware / k€	0	0	1 700	600	550	1 100	1 100	3 000	300	**8 350**
$\sum$	staff / k€	1 860	210	130	150	210	390	180	210	210	**3 550**
	/ PM	186	21	13	15	21	39	18	21	21	**355**

4.1 Guide system

neutron guide SwissNeutronics made an offer for the *Selene* neutron guide and the support system on January 2013. The offer covers the neutron guide on glass or aluminium, the alignment frames, granite beams as a base and an aluminium housing to contain the vacuum. This does not exactly match the requirements by the ESS, since shielding issues most likely will not allow for the offered wide and straight vacuum housing and the alignment system with frames. But it still gives an idea of the actual costs to be expected.

double-*Selene* guide system: 550 k€

support system The support consists of 4 granite beams on kinematic mounts, the alignment frames, the vacuum housing, and vacuum windows. No shielding is included. Mounting is due to the customer.

guide support: 520 k€

shutter The costs for the instrument shutter consisting of a thermal shutter within the common instrument shielding and a light shutter at the end of the instrument shielding were given by P. Bentley, ESS

instrument shutter: 50 k€

vacuum equipment In between the guide sections and before and behind the sample evacuated flight tubes are needed. These host also equipment like polariser, analyser, aperture, and so on.

4.2 Optical components

filter / polariser Based on the costs of a prototype of the bent frame-overlap and polarisation filter, a similar but longer device will cost some 25 k€.

analyser The wide-angle analyser based on SM-coated, bent substrates for the instrument FOCUS at PSI cost some 500 k€ (U. Filges, PSI).

spin flipper The price for one RF flipper (electronics, coils, magnets and housing) is approximately 30 k€ (private communication with P. Hautle, PSI).

guide field In addition, a guide field of some 24 m length has to be realised.

polarisation equipment: 600 k€

4.3 Chopper / scanning aperture

frame-overlap chopper Standard component developed by the ESS

fo-chopper: 200 k€

scanning aperture This device needs to be developed. Here we use the known costs for the alternative double-rotor system (provided by ESS)

scanning aperture: 350 k€

4.4 Mechanics / motion control

sample and virtual source Based on offers by Huber, ADC and Franke, P. Keller, PSI, estimated the costs for the standard components for the sample stage, the beam-definition stage and other similar devices to be $\approx$ 180 k€. This does not take into account that at the sample stage non-magnetic components will be needed, which approximately doubles the costs.

translation / rotation: 400 k€

motion control For the *standard* components an approximate price per freedom of 4 k€ is assumed, including motor controller, encoder, motor, and cabling (discussed with T. Gahl, ESS, 18. 03. 2013).

motion control: 150 k€

4.5 Detectors

area detector The cost estimate for the area detector was given by R. Hall-Wilton, ESS

area detector: 1 000 k€

monitor A fission chamber monitor costs

monitor: 10 k€

scintillator / CCD camera A CCD camera with scintillator and housing for instrument and sample alignment (based on a similar system purchased for BOA at PSI) costs

CCD camera: 60 k€

4.6 Shielding

The common shielding up to $x = 15\,\mathrm{m}$ is not taken into account here. The measures and materials used for this estimate are based on input by P. Bentley, ESS, 10. 04. 2013.

insert The insert within the target monolith is assumed to consist of copper. Its measures are: $0.2 \times 0.2 \times 4.0\,\mathrm{m}^3 = 0.16\,\mathrm{m}^3 \mathrel{\hat{=}} 1.4\,\mathrm{t}$ (the free space for the beam can be neglected here). The masks at 18.6 m and at 26 m and between monolith and common shielding are assumed to use $1\,\mathrm{m}^3$ copper, each. This corresponds to 27 t. Assuming a copper price (04. 2013) of $6\,\text{k€}/t$ this gives

insert in target monolith and masks: 170 k€

instrument shielding The instrument shielding (without the common shielding) from $x = 15\,\mathrm{m}$ to $x = 25.8\,\mathrm{m}$ is assumed to have a heavy concrete core with a cross section of $2 \times 2\,\mathrm{m}^2$ (with the guide in the centre), and an outer shell of light concrete with a cross section of $5 \times 5\,\mathrm{m}^2$. This corresponds to $44\,\mathrm{m}^3$ of heavy concrete, and $226\,\mathrm{m}^3$ of light concrete. Based on a recent (01. 2013) offer to PSI for $200\,\mathrm{m}^3$ light concrete and $50\,\mathrm{m}^3$ heavy concrete this gives

concrete shielding: 2 000 k€

cave Further concrete shielding is needed to protect the sample and detector area from radiation from neighbouring instruments.

cave: 1 000 k€

Appendices

5 List of Abbreviations and Nomenclature **39**

6 Selene Guide System **41**

7 Optics and Beam Shaping **53**

8 Boundary Conditions and Consequences **59**

9 Technical Details **63**

10 Measurement Schemes and Data Reduction **67**

11 McStas Simulations on Reference Sample **81**

12 Prototype **91**

5 List of Abbreviations and Nomenclature

Table 5.1:

physical quantities	
x	lab-system: horizontal scale, *along the main neutron path*
y	lab-system: horizontal scale, normal to x
z	lab-system: vertical scale
t	time, with $t = 0$ at the beginning of a neutron pulse
τ	(≈ 2.86 ms) length of the proton pulse
T	($= 70$ ms) pulse repetition time
λ_{min}	shortest wavelength used for measurements
λ_{max}	longest wavelength used for measurements

ellipse parameters describing the guide geometry	
a	long half-axis
b	short half axis
c	($= a^2 - b^2$) distance from focal point to centre
b/a	asymmetry of ellipse
α	angle between long axis and end of guide seen from the first focal point
β	angle between long axis and beginning of guide seen from the first focal point
$\Delta\theta$	($= \beta - \alpha$) accepted divergence of the guide
ϵ	($= \beta/2 + \alpha/2$) inclination of the long axis relative to the mean beam direction
ξ	effective length of the guide, relative to the distance between focal points

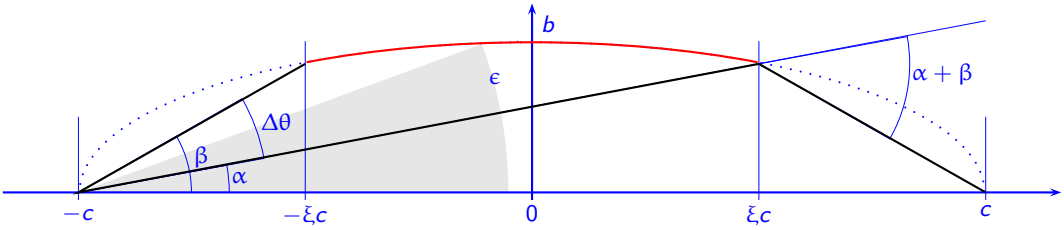

sample coordinate system	
x	direction of neutron beam projected onto the sample plane
y	in the sample plane, normal to x
z	normal to the sample plane
ω	inclination of the sample surface relative to the long axis of the last guide segment.[1]
θ_i	actual angle of incidence of a neutron on the sample surface
θ_f	final angle of a neutron leaving the sample surface
2θ	scattering angle

[1] in the scattering plane ω is a pure instrument parameter and is only indirectly connected to the angle of incidence.

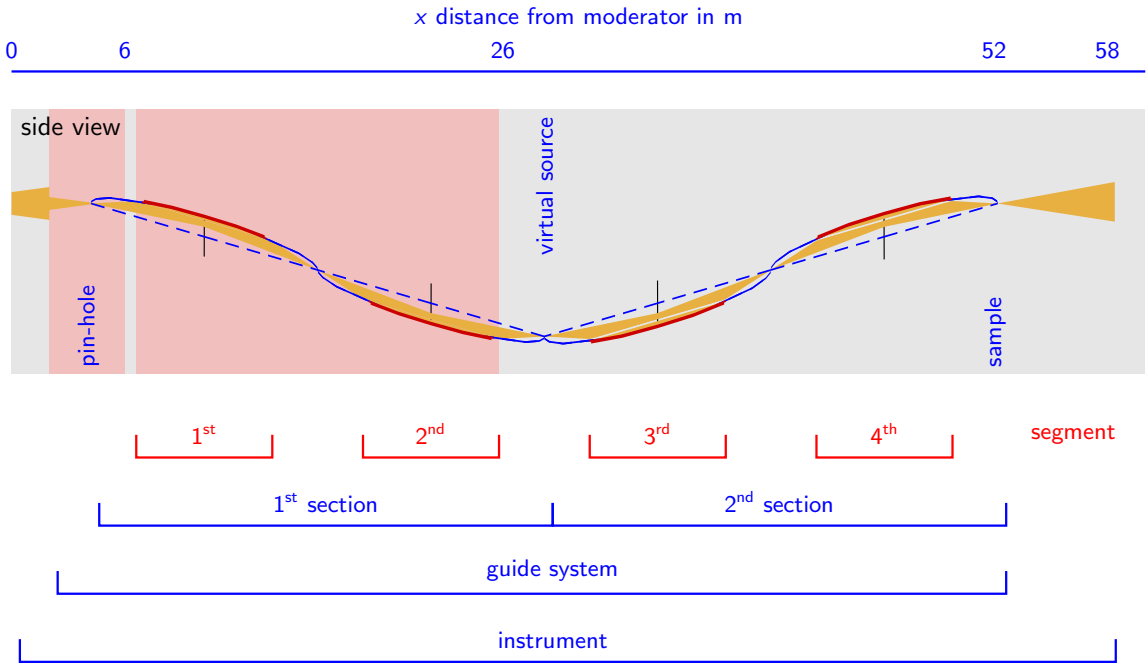

Figure 5.1: Nomenclature used in this script to address the various items and measures of the double *Selene* guide. The sketch is taken from figure 2.2. The guide segments are the elliptically curved and SM coated guides. The distance between the initial and final focal point of one *Selene* guide is called section. Here, two sections and the extraction unit make up the guide system, ending at the sample position.

Table 5.2:

nomenclature (as used in this proposal) for optical elements based on shading the beam	
diaphragm	some device shading part of the beam
slit	a diaphragm consisting of two blades with parallel edges to define the beam width in one dimension
pin hole	(here) a diaphragm with a rectangular opening; avoiding high radiation rather than defining the beam
aperture	opening defining the divergence or resolution (like in optics: an aperture is not placed in an image plane) the diaphragm defining the aperture is also called *aperture stop* or short and improper (nevertheless used here) *aperture*
virtual source	(here) luminous field defined by a special diaphragm, located at the focal point in between the first and second guide sections the diaphragm defining the luminous field is also called *field stop*

Acronyms	
GISANS	gracing incidence small angle neutron scattering
NR	neutron reflectometry
PM	person month
PNR	polarised neutron reflectometry
PSI	Paul Scherrer Institut
SLD	scattering length density
STAP	scientific and technical advisory panel
TOF	time-of-flight

6 The Selene Guide System

We chose two subsequent elliptically shaped reflectors to focus the beam to the sample. The reason is that this set-up allows for:

- independent definition of the divergence $\Delta\theta$, and of the beam footprint on the sample;
- a three-dimensional definition of the footprint;
- convenient beam manipulation;
- early reduction of the phase space, i.e. low background and radiation in the sample and detector region.

At the same time all trajectories have the same length. In the following sections several aspects of the *Selene* guide system are presented.

history The idea for the *Selene* guide is based on concepts by F. Ott to use a focused beam with a wide divergence in combination with λ-θ-encoding, obtained by a graded monochromator of half-elliptic shape.[28, 29] First experiments with a graded multilayer coating [30] revealed conceptual problems and led to the approach to use a flat multilayer monochromator for λ-θ-encoding, followed by the elliptic reflector. And attempts to correct for coma aberration finally led to the *Selene* guide geometry with two subsequent elliptic reflectors. This way, neutron guide and encoding are decoupled. This means that encoding is optional and might be also achieved by other approaches like the *rainbow* concept by R. Cubitt.[31, 32]

Though developed for a reflectometer, the *Selene* guide concept can in principle also be used for other instruments. The limiting factors are the transported divergence, the minimum wavelength, and the sample size.

optimisation strategy The design and a large part of the optimisation of the *Selene* guide system was performed analytically. This is possible because of the rather straight-forward and clear mathematical description of the possible beam trajectories. As a consequence one can relate almost all geometrical parameters of the guide system, the coating and the transmission. The rather large number of parameters collapses this way to essentially three which can be chosen freely. All the rest is then determined. In the following sections these relations are derived and discussed.

Figure 6.1 illustrates the approach chosen here for the design of the instrument, starting with an estimate for the desired divergences and wavelength-range at the sample position. The second set of input parameters are the given source brightness $I_0(\lambda)$ and a reasonable length of the guide, described by the ratio of the actual guide segment length to the focal point distance, ξ. As figure of merit the measurement time t is used. The physical parameters of the guide (b/a and ϵ) are deduced from the starting parameters and they determine the coating (m), reflectivity (R) and thus the transmission T of the guide. Together with the divergence and $I_0(\lambda)$ this determines the counting time.

The *optimisation problem* can be illustrated at the example of $\Delta\theta$, which enters the counting time quadratically (for high-intensity specular reflectivity), but which also affects m linearly. Since high m leads to a lower transmission T with a more complicated dependence, one has to iteratively find the best $\Delta\theta$.

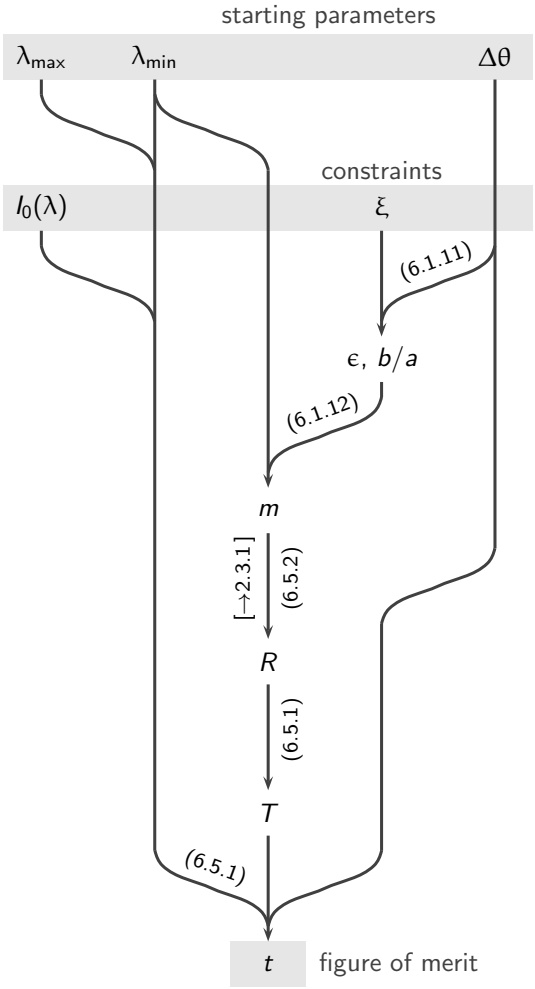

Figure 6.1: Flow diagram used to estimate the counting time t as a figure of merit from chosen (λ-range, $\Delta\theta$) and given ($I_0(\lambda)$, ξ) starting parameters.
The meaning of the other symbols is: ϵ, b/a orientation and shape of the ellipses, m coating of guides, R reflectivity of the guide, and T transmission of the guide system.
The diagram is simplified since it is based on the ideal assumption of a point-like sample, perfect guides and coatings, and some external constraints such as the exclusion of the prompt time for data collection [→8.3] are not taken into account.

6.1 Geometrical considerations for an elliptic reflector

The geometry of the elliptic guides (i.e. the ratio of the half axes b/a), their length and coating should be defined starting by the requirements at the sample position. The limitations are the maximum curvature of the guide, the available coating, $I_0(\lambda)$, and the space available.

The following formulae can be used to estimate the optimum geometry of a *Selene*-type guide for given parameters like expected divergence $\Delta\theta$, and wavelength-range $\lambda_{min} \ldots \lambda_{max}$.

Theses formulae are based on the small-angle approximation $\tan\alpha \approx \alpha$, $\tan\beta \approx \beta$, and a strong asymmetry of the ellipse $a \gg b \Rightarrow c \approx a$. Furthermore, the distance from the initial focal point to the guide entrance is assumed to be the same as the distance from its exit to the second focal point.

ellipse relation:

$$\frac{x^2}{a^2} + \frac{y^2}{b^2} = 1 \tag{6.1.1}$$

$$y = \pm\frac{b}{a}\sqrt{a^2 - x^2} \tag{6.1.2}$$

$$c = \sqrt{a^2 - b^2} \quad \text{half distance between focal points} \tag{6.1.3}$$

minimum acceptance angle (relative to long axis):

$$\begin{aligned}\alpha &\approx \frac{b}{a}\frac{\sqrt{a^2-(\xi a)^2}}{(\xi+1)a}\\ &\approx \frac{b}{a}\sqrt{\frac{(1-\xi)(1+\xi)}{(1+\xi)^2}}\\ &\approx \frac{b}{a}\sqrt{\frac{1-\xi}{1+\xi}}\\ &\approx \frac{b}{a}\frac{1-\xi}{\sqrt{1-\xi^2}}\end{aligned} \tag{6.1.4}$$

maximum acceptance angle (relative to long axis):

$$\begin{aligned}\beta &\approx \frac{b}{a}\frac{\sqrt{a^2-(\xi a)^2}}{(\xi-1)a}\\ &\approx \frac{b}{a}\sqrt{\frac{(1-\xi)(1+\xi)}{(1-\xi)^2}}\\ &\approx \frac{b}{a}\sqrt{\frac{1+\xi}{1-\xi}}\\ &\approx \frac{b}{a}\frac{1+\xi}{\sqrt{1-\xi^2}}\end{aligned} \tag{6.1.5}$$

accepted / delivered divergence:

$$\begin{aligned}\Delta\theta &= \beta-\alpha\\ &\approx \frac{b}{a}\left(\frac{1+\xi}{\sqrt{1-\xi^2}}-\frac{1-\xi}{\sqrt{1-\xi^2}}\right)\\ &\approx \frac{b}{a}\frac{2\xi}{\sqrt{1-\xi^2}}\end{aligned} \tag{6.1.6}$$

inclination of the centre of the beam relative to the long half axis:

$$\epsilon = \frac{1}{2}(\alpha+\beta) \tag{6.1.7}$$

$$\begin{aligned}&\approx \frac{1}{2}\frac{b}{a}\left(\frac{1+\xi}{\sqrt{1-\xi^2}}+\frac{1-\xi}{\sqrt{1-\xi^2}}\right)\\ &\approx \frac{1}{2}\frac{b}{a}\frac{2}{\sqrt{1-\xi^2}}\\ &= \frac{\Delta\theta}{2\xi}\end{aligned} \tag{6.1.8}$$

minimum coating of the guide surface:

$$m = \frac{4\pi\frac{\alpha+\beta}{2}}{\lambda_{\min}\, q_{\mathrm{Ni}}^{c}} \qquad \text{with (6.1.7):}$$

$$= \frac{4\pi\,\epsilon}{\lambda_{\min}\, q_{\mathrm{Ni}}^{c}} \tag{6.1.9}$$

Starting with input parameters $\lambda_{\min}$ and $\Delta\theta$ required at the sample, and with given ξ, it is possible to deduce all other parameters:

$$\frac{b}{a} \approx \frac{\Delta\theta}{2}\sqrt{\frac{1}{\xi^2}-1} \tag{6.1.10}$$

$$\epsilon \approx \frac{\Delta\theta}{2\xi} \qquad \text{inclination of the guide, and maximum angle of incidence on the guide} \tag{6.1.11}$$

$$m = \frac{4\pi\,\epsilon}{\lambda_{\min}\, q_{\mathrm{Ni}}^{c}} \qquad \text{for a finite source, the angular error has to be taken into account to calculate the } \textit{real } m \tag{6.1.12}$$

and

$$\alpha \approx \epsilon \cdot (1 - \xi) \tag{6.1.13}$$
$$\beta \approx \epsilon \cdot (1 + \xi) \tag{6.1.14}$$

For $\xi = 0.6$ one gets the following approximations:

$$\begin{aligned} \frac{b}{a} &\approx \frac{2}{3}\Delta\theta \\ &\approx 0.012\,\Delta\theta/\,\mathrm{deg} \\ \epsilon &\approx 0.8\,\Delta\theta \\ m &\approx 8\,\frac{\Delta\theta/\,\mathrm{deg}}{\lambda_{\mathrm{min}}/\,\text{Å}} \end{aligned}$$

For $\Delta\theta \approx 2\epsilon$ the pre-assumptions are no longer fulfilled! A reasonable upper limit for ξ is about 80%.

Figure 6.2 shows the iso-lines for constant m and for constant $\Delta\theta$ on a map of b/a vs. ξ, obtained for $\lambda = 4$ Å. E.g. if a divergence of $\Delta\theta > 3^\circ$ is required, but the coating is limited to $m = 6$, the possible values for b/a and the relative length ξ are within the (light gray) area below the blue iso-line for $m = 6$ and above the red iso-line for $\Delta\theta = 3^\circ$. So the smallest ξ is ≈ 0.62 with the strong curvature $b/a \approx 0.033$. Relaxing the latter value leads to a longer guide and allows for a coating with lower m.

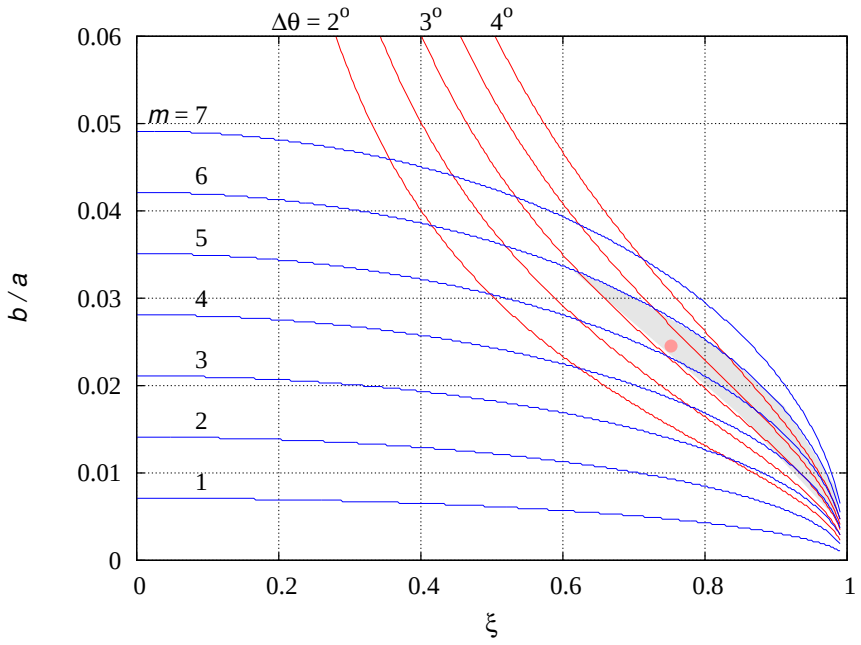

Figure 6.2: Iso-line for constant m (blue) and for constant divergence $\Delta\theta$ (red) for $\lambda = 4$ Å as a function of the effective length of the guide ξ and the ratio of the half axes parameters b/a.

Reducing the wavelength e.g. from 4 Å to 2 Å does not affect the red iso-line, but the blue ones are scaled down by 0.5 along b/a. There is no intersection left (for reasonable guide lengths) with the $\Delta\theta = 3^\circ$ criterion, so that there is no guide geometry possible fulfilling the requirements.

For $\Delta\theta = 3^\circ$ and $\lambda = 4$ Å a reasonable choice would be $b/a \approx 0.025$ and $\xi = 0.75$ (marked by a red dot). The coating then should be $m \approx 5.5$. (These are for the sake of example and are not the parameters chosen for *Estia*.)

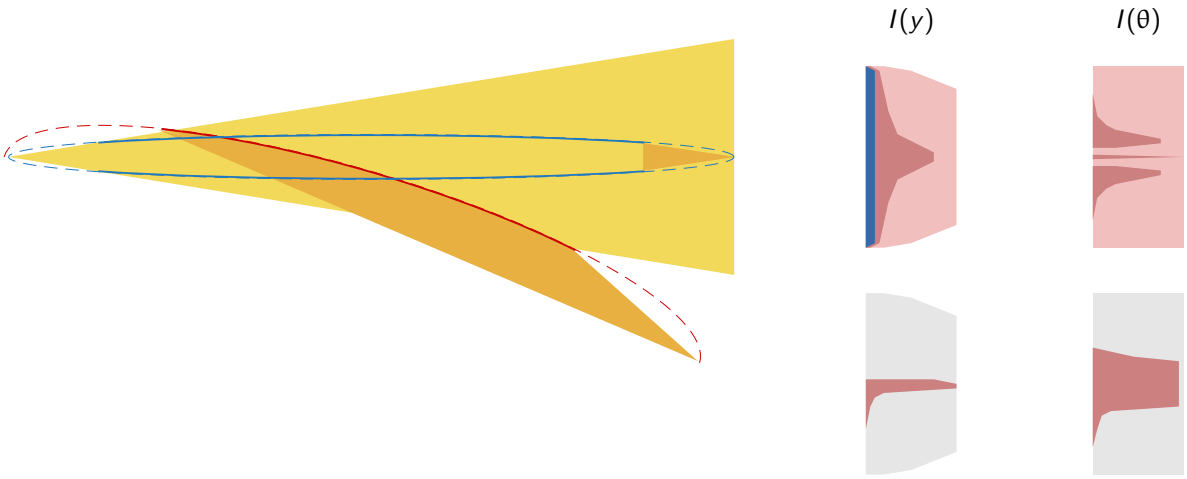

Figure 6.3: Sketch to illustrate the difference between a full elliptic guide (blue) and a *Selene* guide (red). Both are designed to deliver a beam of a certain divergence to the sample (gold). The beam emitted by the source (yellow) of a certain divergence is accepted by both guides. The elliptic guide generates $I(y)$ and $I(\theta)$ distributions containing contributions with no (blue area), one (red) and multiple reflections (light red). Due to the strong coma of the full ellipse (large ξ, small b/a) the single-reflected beam is quite broad in $I(y)$, and it shows a bi-modal distribution in $I(\theta)$ caused by the guide not closing about the source. The complete beam over-illuminates the sample position and it provides a wide divergence, while the divergence at the sample position is considerably narrower (defined by the distance and width of the guide end). In contrast, the *Selene* guide delivers only neutrons reflected exactly one time, with the wanted divergence and a sharp beam spot. (The one-reflector set up shown here still suffers from coma aberration which leads to the visible tails in the $I(y)$ and $I(\theta)$ distributions.)

6.2 Angular acceptance

We are often confronted with the remark that a full ellipse could transport twice the divergence of half an elliptic guide. The point is that the divergence should be defined by the needs on the sample, or it is given by geometrical limitations. In this case one has to ask for the most efficient way to transport this divergence. And if this can be realised with one branch of an ellipse, there is no need to accept the disadvantages of the full ellipse. Figure 6.3 illustrates this.

6.3 Coma aberration — and correction

Elliptic reflectors show coma aberration. This means two things: radiation emitted from (close to) the first focal point into a solid angle Ω and reflected before the mid of the ellipse reaches the second focal point under a smaller solid angle. Radiation emitted in Ω but reflected behind the mid of the ellipse results in a large solid angle. Consequently, the focusing / de-focusing property of the reflector varies along its length.

At the same time the position of the image of an off–axis pre-image point depends on the position where along the reflector the beam is reflected. For an early reflection the distance of the image from the long axis increases, for a late reflection it decreases.

In total the phase space density is conserved, but the distribution of intensity vs. angle and beam-height $I(\theta, z)$ is distorted. An identical second collinear reflector, sharing one focal point with the first one, shows the same aberration, but since early reflection in the first reflector leads to a late reflection in the second one, the distortion is almost cancelled.

This is illustrated in figure 6.4. The maps show $I(\theta, z)$ as accepted by the elliptic reflector (left), the corresponding intermediate image with the distorted shape (middle) and the almost restored shape at the image (source) position. The deviations still visible originate from the final length of the second reflectometer, and from the quite large pre-image chosen to emphasise the effect of coma aberration.

For small angles, i.e. small b/a and $\xi < 0.8$ one can deduce a simplified mapping algorithm. A trajectory connecting the first focal point, a point on the ellipse at (x', z'), and the second focal point intersects the

long axis at angles α_1 and α_2. These are given by

$$\begin{aligned} \alpha_1 &\approx \tan\alpha_1 \\ &\approx z'/(c-x') \qquad \text{and} \\ \alpha_2 &\approx z'/(c+x') \end{aligned}$$

Using eqn. 6.1.2 and $c \approx a$ one gets

$$\begin{aligned} z' &= \frac{b}{a}\sqrt{c^2 - x'^2} \\ \alpha_1\alpha_2 &= \frac{z'^2}{(c-x')(c+x')} \\ &= \left(\frac{b}{a}\right)^2 \frac{c^2-x'^2}{c^2-x'^2} \\ &= \left(\frac{b}{a}\right)^2 \end{aligned}$$

If the trajectory intersects the first focal plane with a (small) offset z_1 this leads to an angular error $\Delta\alpha \approx z_1/(c-x')$. Since the beam is specularly reflected, α_2 changes by the same $\Delta\alpha$. The resulting offset at the

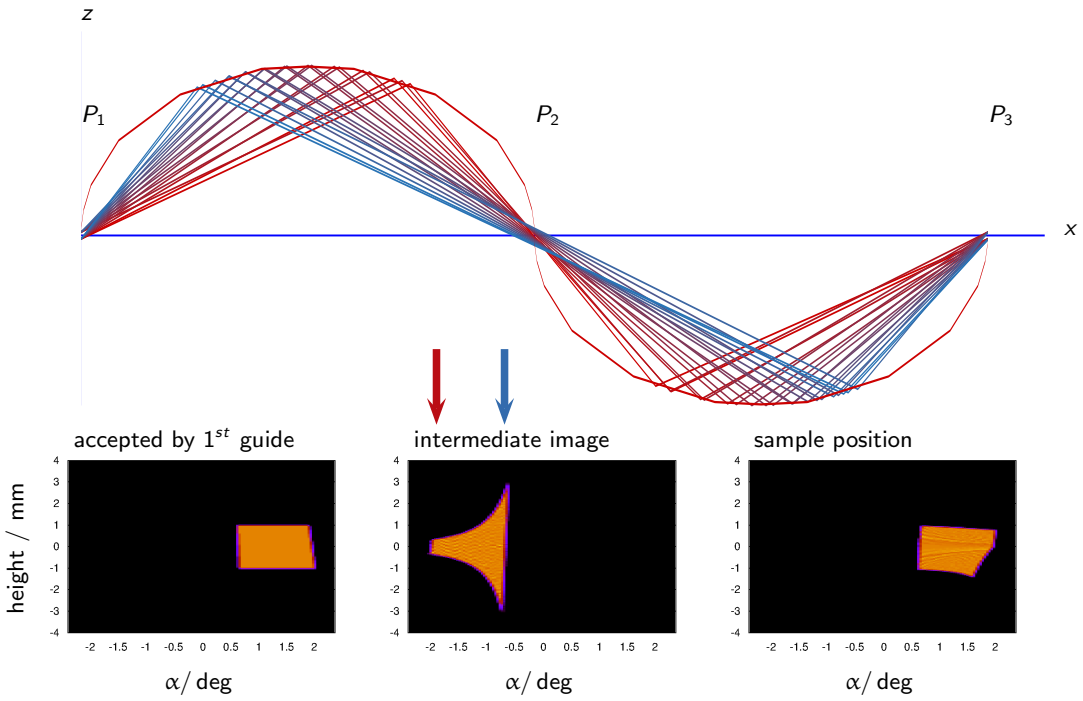

Figure 6.4: Sketch to illustrate the effect of coma aberration. The pre-image consists of 2 point-sources, located at $z = \pm 1$ mm. The half-axis parameters used here are $a = 2000$ mm, $b = 50$ mm, the sketch is stretched by 30 normal to the long axis. The take-off angle α is encoded in the colour of the beam. At the intermediate position a clear separation of the colours can be seen. High α results in an almost parallel wide beam, while low α results in a beam focused to the second focal point. Behind the second ellipse, the initial image is almost restored. The $I(\alpha, z)$ maps illustrate the shape of the phase space as accepted by the ellipse and defined by a 2 mm slit at P_1 (left), at the intermediate position P_2 (middle), and finally after correction at P_3 (right). The arrows atop the middle map denote for which α the beam is compressed (red) or expanded (green).

second focal plane is

$$\begin{aligned} z_2 &\approx (c + x')\,\Delta\alpha \\ &\approx \frac{c + x'}{c - x'}\, z_1 \\ &\approx \frac{\alpha_1}{\alpha_2}\, z_1 \\ &\approx \frac{(b/a)^2}{\alpha_2^2}\, z_1 \end{aligned}$$

The second elliptic reflector transforms z_2 into

$$\begin{aligned} z_3 &\approx \frac{(b/a)^2}{\alpha_3^2}\, z_2 \\ &\approx \frac{(b/a)^2}{\alpha_3^2}\,\frac{(b/a)^2}{\alpha_2^2}\, z_1 \\ &\quad \text{with } \alpha_2\alpha_3 = (b/a)^2 \\ &\approx z_1 \end{aligned}$$

This means that reflection on a range $\{x\}$ rather than a point x' results in a line at the second focal plane, but again in a point at the third focal plane. The coma[1] aberration is corrected for.

There are several limitations for this approach:

source height The source height is limited by the requirement that no garland reflections should occur. The *first* garland case one reaches by making z larger is the one when the trajectory connects $(-c, z(-c))$, the entrance of the guide $(-\xi c, z(-\xi c))$, the exit of the guide $(\xi c, z(\xi c))$, and a point on the second focal point. The symmetry of the problem tells, that the trajectory is parallel to the long axis between the two points on the ellipse. The inclination of the guide at the entrance is $\beta - \epsilon$. Thus the inclination of the incoming trajectory is twice this value:

$$\begin{aligned} z_1 &= \beta\,(1 - \xi)c - 2(\beta - \epsilon)\,(1 - \xi)c \\ &= (2\epsilon - \beta)\,(1 - \xi)c \\ &= (2\epsilon - (1 + \xi)\epsilon)\,(1 - \xi)c \\ &= \epsilon\,(1 - \xi)^2 c \end{aligned}$$

For the *Estia* parameters this means $z_1 < 21\,\text{mm}$! To the other side of the long axis, away from the reflector, there is no such restriction. The *missing* lower right edge of the phase space volume at the sample position of figure 6.4 illustrates this effect.

higher angles Exact calculation of the trajectories not using the small angle approximation show that the aberration is not completely compensated for. This can be seen in the slight bending of the phase space volume in figure 6.4.

finite reflector length Trajectories with a large offset at the intermediate focal point might miss the entrance or the exit (i.e. they are not reflected) of the second guide. These are lost. As a consequence the image at the final focal point gets blurred on one side (the other side is limited by the acceptance of the first reflector). This sets a limit for the source size in the other direction.

making use of coma aberration It is not always useful to correct for coma aberration: If e.g. a small beam is required, one can reach this by using the beam reflected at the end of the reflector. For the present case, its height is only 30% of the initial slit. On the other side one can get a wide beam of low divergence by using only the beginning of the reflector. This is what at synchrotron sources is achieved with a Kirkpatrick-Baez optics (which consists of two elliptically shaped reflectors, one for each transverse direction).

[1] *coma* (lat.) means *tail* and refers to the shape of the image of a not-centred point source or, more generally, a finite source

6.4 Chromatic aberration due to gravity

P. Korelis, E. Rantsiou

While the focusing properties of reflecting optics are achromatic (besides the λ dependent reflectivity) for straight trajectories, there are chromatic effects induced by gravity. Its influence on the spot size and divergence is not immediately apparent because there are amplifying and compensating aspects for reflections on an elliptic guide. For example, if one assumes the first reflection pointing downwards, gravity leads to a longer free flight path before the neutron hits the reflector. But it will hit it at a smaller angle.

The drop of the neutrons due to gravity is given by

$$\begin{aligned} \Delta z &= -\frac{1}{2} g\, t^2 \\ g &\approx 9.81\,\mathrm{m/s^2} \\ t &\approx 2.52 \cdot 10^{-4}\,\mathrm{s\,m^{-1}\,\text{Å}^{-1}}\, x\, \lambda \\ \Rightarrow \frac{\Delta z}{\mathrm{m}} &\approx 3.07 \cdot 10^{-7} \left(\frac{x}{\mathrm{m}} \frac{\lambda}{\text{Å}} \right)^2 \end{aligned}$$

So Δz scales with distance and wavelength squared.

Δz	$x = 2400$ mm	9600 mm	19200 mm
$\lambda = 5.0$ Å	−0.04 mm	−0.7 mm	−2.8 mm
9.4 Å	−0.16 mm	−2.5 mm	−10 mm

The main question to be answered then is whether or not gravity sets limitations to the focusing performance of a *Selene* guide at the sample position. To elucidate the effect of gravity, virtual studies using the McStas simulation software package have been performed.

The model instrument is comprised of a single *Selene* guide with the first element reflecting downwards and the second reflecting upwards as shown in figure 6.5. The geometrical parameters are the same for the horizontal (xy plane) and vertical (xz plane) elliptic reflectors: $b/a = 0.0228$, $\xi = 0.5$, and length of the focusing section $4c = 40$ m. The resulting angular acceptance is $\Delta\theta = 1.5°$.

To single out the effect of gravity and to better illustrate that, certain simplifications have been added to the model. Regarding reflector performance, the reflectors are constructed from ideal supermirrors, disregarding changes in supermirror reflectivity as a function of momentum transfer and effects such as absorption. A virtual source is used, with a uniform wavelength distribution extending from 2 to 10 Å, and it is located at the entrance focal point of the *Selene* guide. The size of the source is 1×1 mm^2 and its divergence is adjusted to compensate for the crooked neutron trajectories that might result in some of the long-wavelength neutrons missing the far end of the reflector. As a result, the entirety of the reflecting surface of the first *Selene* element is illuminated by neutrons of all wavelengths.

Figure 6.6 shows the intensity maps at the intermediate focal point P_2, simulated with and without including gravity (bottom and top row, respectively). To single out with which trajectory certain features in the intensity maps are related, the first and second half of the first guide element were interchangeably switched to be vertically absorbing. The horizontal reflection element was fully reflecting in all cases.

The coma aberration, inherent to the elliptical shape of the reflectors, is evident in the intensity maps in the top row. Reflecting on the first half of the vertical elliptical reflector (left image) contributes a broad beam profile at P_2. In an inverse manner, reflecting on the second half of the vertical elliptical reflector (right image) results in a highly focused beam profile. As expected, the centre image in the top row, generated by reflecting on the complete first element, shows no difference in the intensity profile between the vertical and horizontal direction.

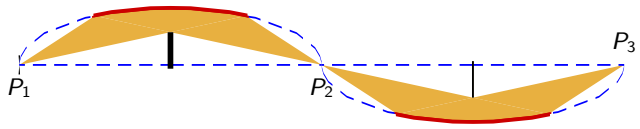

Figure 6.5: Sketch of the setup used for simulations including gravity. The guide parameters are $c = 10\,000$ mm, $b/a = 0.0228$ and $\xi = 0.5$. The initial slit has a height of 1 mm and is centred at the focal point.

Gravity is included in the simulations shown in the bottom row. While no change in focusing is observed in the horizontal direction, a tail becomes visible in the vertical direction. Gravity does little to improve the focusing of neutrons reflected on the first half of the vertical elliptical reflector. The vertical tail is also shown to originate almost exclusively from reflections on the first half of the reflector. Reflections on the second half of the vertical elliptical reflector (bottom right image), are found to result in some smearing out of the bright focused spot, along the positive direction of the vertical axis. It was further clarified, through simulations using a single wavelength, that the vertical position of the focusing spot at P_2 shifts upwards, scaling with neutron wavelength. On one hand, the height of the focusing position for longer wavelengths is shifted upwards, and on the other hand, the long-wavelength neutrons are also more heavily influenced by gravity on their way to the second *Selene* element.

The intensity maps of the beam spot at the exit focal point P_3 are shown in figure 6.7, simulated with and without gravity. In the graph to the right, the intensity is integrated along the horizontal direction and the distribution of intensity as a function of the vertical position is shown for selected wavelengths.

Comparing the intensity maps, the beam profile appears to be close to fully restored. It becomes apparent that a compensating mechanism exists for the effect of gravity for small λ, once the neutrons have travelled through and interacted with the full length of the *Selene* guide. The integrated intensity as a function of vertical position indicates that for small wavelengths, e.g., 3 Å, the effect of gravity is negligible. For wavelengths near the upper end of the range that is expected at ESS for a *Selene* type reflectometer, there is an observable change, manifested by a vertical shift of the centre of the focused spot by approximately 0.3 mm, broadening at the base by nearly the same amount and a corresponding reduction in the intensity of the maximum plateau by about 15%.

The $I_\lambda(z)$ graph illustrates that there is only a week chromatic aberration up to at least 6 Å and a moderate effect at 9 Å. Above that the picture changes, the intensity for $\lambda = 15$ Å, for example, is distributed over 4.5 mm with a bi-modal distribution. Obviously there is an upper limit for $x^2\,\lambda^2$, up to which the *Selene* guide has low chromatic aberration due to gravity.

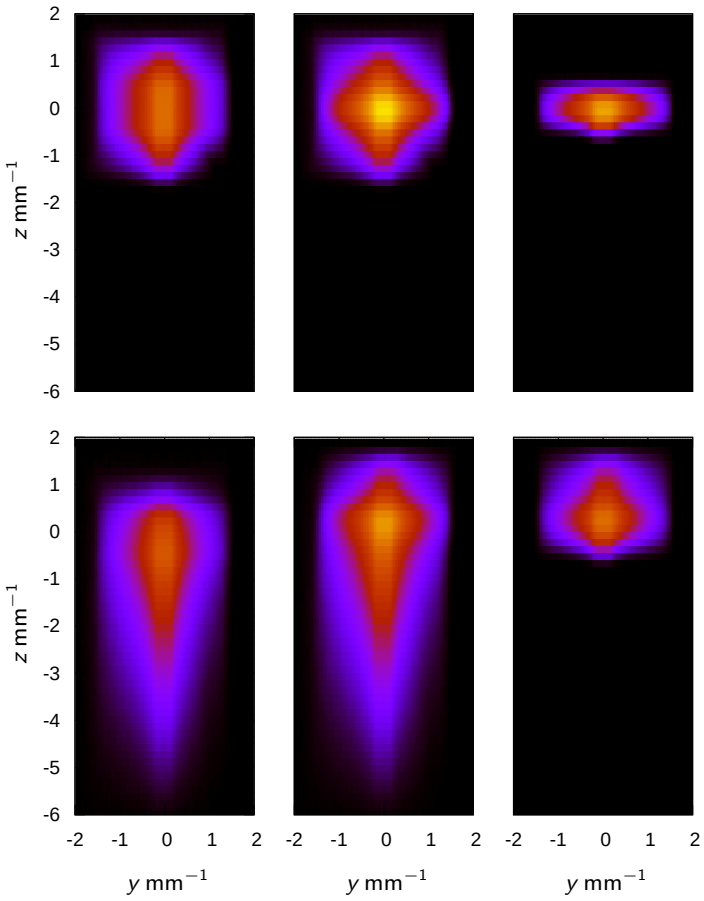

Figure 6.6: Intensity maps $\log_{10}[\,I(y,z)\,]$ at the intermediate focal point P_2 of a *Selene* guide system with a total length of 40 m. The upper row was simulated without gravity, the lower one with gravity. For the left/right column only the first/second half of the vertically reflecting guide element was actually reflecting. The middle column was obtained with reflection along the full guide element. The incident slit was $1 \times 1\,\text{mm}^2$, the wavelength-range was $\lambda \in [2,\,10]$ Å.

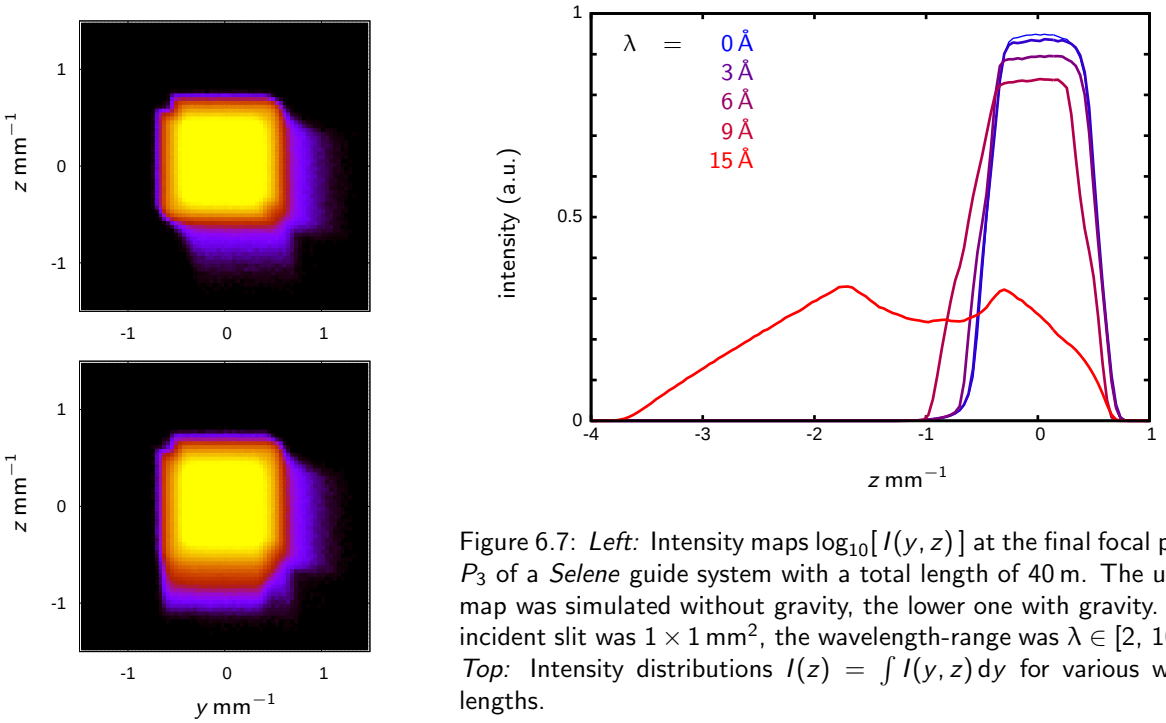

Figure 6.7: *Left:* Intensity maps $\log_{10}[\,I(y,z)\,]$ at the final focal point P_3 of a *Selene* guide system with a total length of 40 m. The upper map was simulated without gravity, the lower one with gravity. The incident slit was $1 \times 1\,\mathrm{mm}^2$, the wavelength-range was $\lambda \in [2, 10]$ Å. *Top:* Intensity distributions $I(z) = \int I(y,z)\,\mathrm{d}y$ for various wavelengths.

In a further set of simulations the geometry shown in figure 6.5 was turned upside down, i.e. the first guide element reflecting downwards and the second upwards. The essential difference is, that for longer wavelengths the intensity is reduced (some 10% at $\lambda = 9$ Å), while the spot size is slightly smaller.

discussion Taking into account that the actual length of one *Selene* section will be 24 m instead of the 40 m used here, while keeping the λ-range, one can assume that the chromatic aberration plays in the sub-mm-range for the proposed reflectometer with two *Selene* sections. In addition, it affects only the spot size normal to the scattering plane.

chromatic aberration on Estia Similar simulations as described above were performed for the lay-out and geometry of *Estia* as given in table 2.2. Figure 6.8 shows the vertical intensity distribution $I(z)$ at the sample position.

Here gravity has three obvious effects: ○ It leads to a slight reduction of the transmission, caused by the fact that some neutrons do not reach a coma-correcting second guide segment due to gravity. ○ The intensity peak shifts upward by at most 1 mm. ○ And the profile gets sharper with increasing wavelength. The latter effect overcompensates the mentioned shift, so that the full beam still hits the sample.

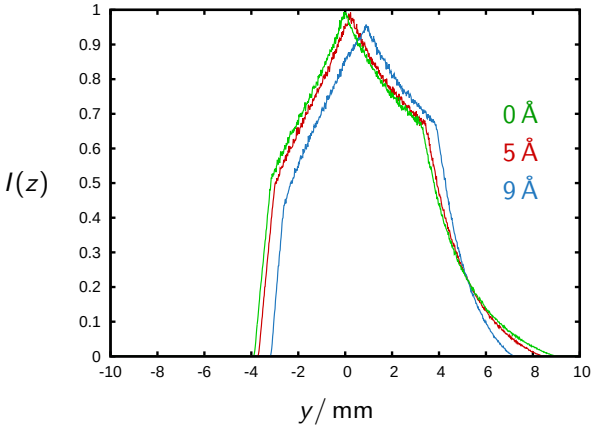

Figure 6.8: Simulated vertical intensity distribution $I(z)$ at the sample position of *Estia* (normal to the scattering plane). The green line was obtained without gravity, the red and blue lines correspond to 5 Å and 9 Å, respectively.

6.5 Transmission

The effective flux at the sample can be estimated by reducing the initial flux $I_0(\lambda)$ by the losses due to reflections on the guide walls. The double *Selene* guide concept involves 8 reflections for all neutrons on surfaces with

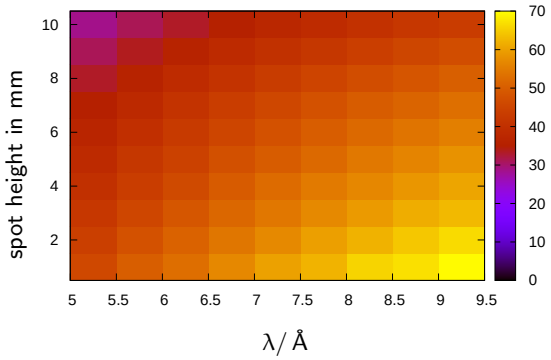

Figure 6.9: Brilliance transfer of *Estia* obtained by McStas simulations for a divergence of $1.5° \times 1.5°$ and beam spot sizes reaching from $1 \times 10\,\mathrm{mm}^2$ to $10 \times 10\,\mathrm{mm}^2$.

a non-perfect reflectivity R (plus further reflections in the extraction unit). The angle of incidence on the guide surface hardly varies along the guide for the presented concept: $\theta \approx \epsilon = \Delta\theta/2\xi$. One can thus assume $R(q_z) = R(\lambda, m)$, with the optimised coating m [→6.1.12]. This leads to and an attenuation of

$$I(\lambda) \quad = \quad I_0(\lambda) \cdot \prod_{i=1}^{n} R(\lambda, m_i) \tag{6.5.1}$$

n is the number of reflections,. This pushes the flux maximum to higher λ. Based on typical reflectivities (by SwissNeutronics) the following linear relation was used for a fast estimate of the transmission:

$$R(\lambda, m) \quad = \quad \begin{cases} 1 & \text{for } \lambda > m\,\lambda_{\mathrm{min}} \\ 0 & \text{for } \lambda < \lambda_{\mathrm{min}} \\ \frac{13}{12} - \frac{1}{12}\,\frac{m\,\lambda_{\mathrm{min}}}{\lambda} & \text{else (i.e. 50\% reflectivity at } m = 7 \text{ and 100\% at } m = 1) \end{cases} \tag{6.5.2}$$

The resulting transmission for *Estia* is shown in the graph in table 2.1.

More precise results were obtained by performing McStas simulations on the full guide (without gravity, assuming a perfect surface). The resulting brilliance transfer strongly depends on the beam spot size. In figure 6.9 the brilliance transfer as a function of wavelength and beam spot size is given.

7 Optics and Beam Shaping

7.1 Frame-overlap and polarisation filter

An optical element used for polarising a beam or for frame-overlap suppression (i.e. used as a low-pass for λ) should ideally intersect the beam at the same optimised angle γ everywhere within the beam. For a parallel beam this is fulfilled by a flat surface, inclined relative to the beam by γ. For a beam emerging from a point the corresponding surface has the shape of a logarithmic spiral

$$\begin{aligned} x &= a\,e^{bt}\cos t \\ y &= a\,e^{bt}\sin t \end{aligned}$$

with $b = 1/\tan\gamma$, and the scaling factor a.

For a small γ and a rather low divergence $\Delta\alpha \ll 10°$ the spiral can be approximated by a function $f(x)$. A beam trajectory passing through the origin with slope α has the function

$$y_\alpha(x) = x\tan\alpha \tag{7.1.1}$$

It intersects $f(x)$ at the point where

$$f(x_\alpha) = x_\alpha\tan\alpha$$

At this point the slope of $f(x)$ has to be $(\alpha+\gamma)$. Thus

$$\begin{aligned} f'(x_\alpha) &= \tan(\alpha+\gamma) \\ &= \frac{\tan\alpha+\tan\gamma}{1-\tan\alpha\tan\gamma} \\ &= \frac{f(x_\alpha)/x+\tan\gamma}{1-f(x_\alpha)/x\tan\gamma} && (7.1.2) \\ &\approx \frac{f(x_\alpha)}{x_\alpha}+\gamma \qquad \text{for small } \gamma \text{ and } \alpha && (7.1.3) \end{aligned}$$

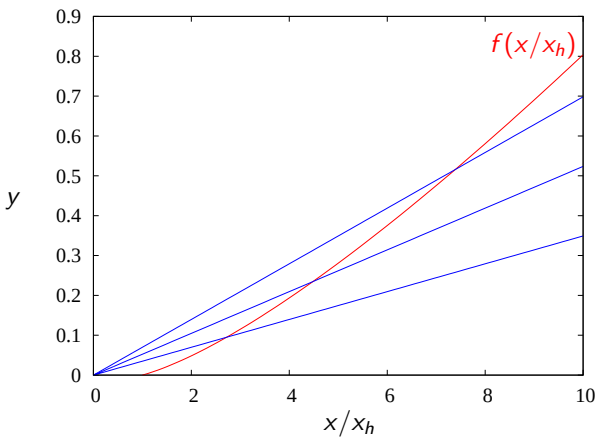

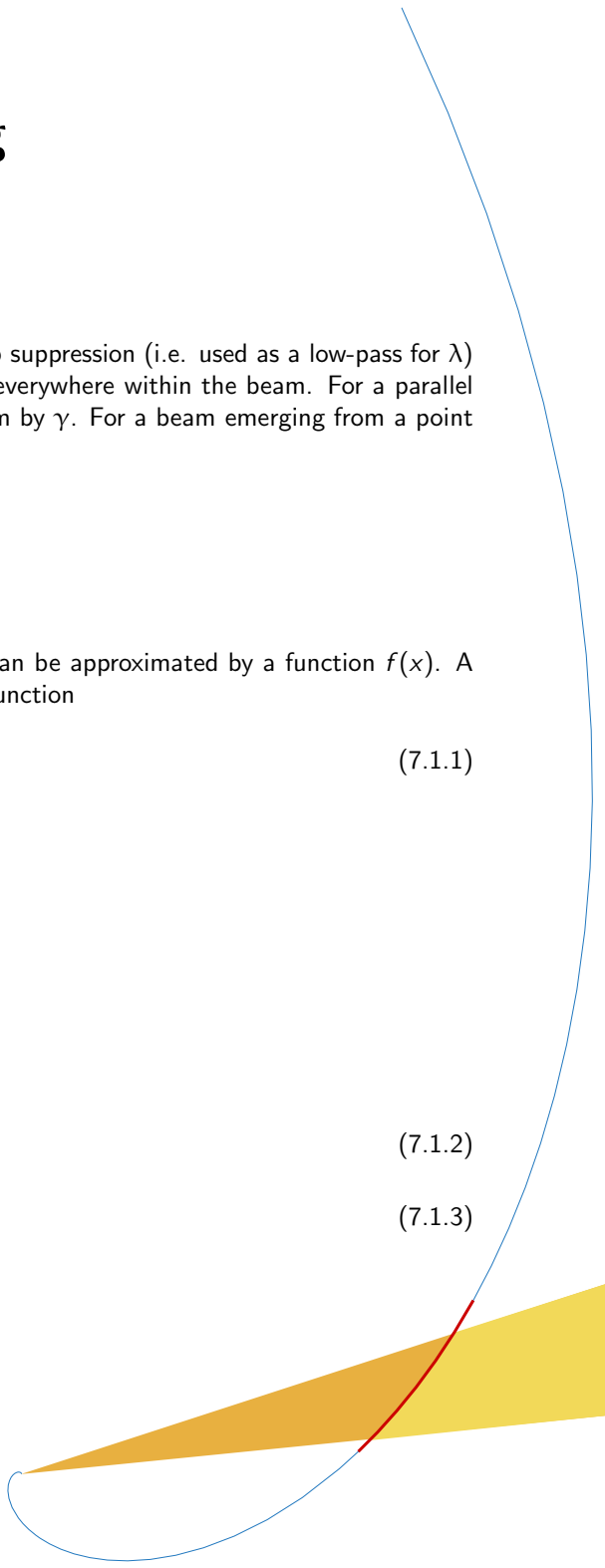

Figure 7.1: Sketch of the geometry of a surface $f(x)$ which is hit by all trajectories $y = x\tan\alpha\,(\forall\alpha)$ at the same angle γ. Here $\gamma = 2°$ and $\alpha = 2°, 3°, 4°$ are displayed.

It is assumed here that all angles are small. Equation 7.1.3 does no longer contain α so that the index can be dropped. The solution for this simplified differential equation is

$$f(x) \;=\; \gamma\, x\, \ln\left[\frac{x}{x_h}\right] \tag{7.1.4}$$

where x_h is a scaling factor given by the intersection of $f(x)$ with the horizon $f(x_h) = 0$.

Since the problem is centrosymmetric, one can rotate f around the origin (which is the same as changing x_h).

The intersecting point is obtained by

$$\begin{aligned} \gamma\, x_\alpha\, \ln\left[\frac{x_\alpha}{x_h}\right] &= x_\alpha \tan\alpha \\ \gamma \ln\left[\frac{x_\alpha}{x_h}\right] &\approx \alpha \\ x_\alpha &= x_h \exp\left[\frac{\alpha}{\gamma}\right] \end{aligned}$$

A possible application is the *simultaneous* use of such a device as frame overlap filter and polariser. For the **low-pass for** λ the ideal coating is Ni with $R = 1$ for $q < q_{\mathrm{Ni}}$. The (idealised) cut-off angle is then given by

$$\sin\gamma = q_{\mathrm{Ni}}\,\frac{\lambda_{\mathrm{max}}}{4\pi}$$

Below the Ni coating a polarising SM can be deposited with

$$m \;=\; 4\pi\,\frac{\sin\gamma}{\lambda_{\mathrm{min}}\, q_{\mathrm{Ni}}} \;=\; \frac{\lambda_{\mathrm{max}}}{\lambda_{\mathrm{min}}}$$

For the present parameters $\lambda \in [5, 9.4]$ Å one gets $\gamma \approx 1°$, and $m_{\mathrm{SC}} < 2$. Assuming $\Delta\theta = 1.5°$ and a minimum distance of the device from the point-source of 300 mm, the total length is $300\,\mathrm{mm}\cdot\exp[1.5°/1°] \approx 1\,400\,\mathrm{mm}$. These numbers are obtained for a point source. For a finite source they increase.

prototype A polariser based on the principle mentioned above was designed and build for the *Selene* prototype.[1] The rather short distances and the relatively large virtual source with a height of 1 mm resulted in a split assembly, i.e. the device has a V-shape comparable to a polarising cavity.[2] Figure 7.2 shows the first sketch and the final device.

[1] The device was designed at the Laboratory for Neutron Scattering, PSI, and manufactured by SwissNeutronics.

[2] Despite the similar shape, this is no cavity. The polarisation is based on exactly one interaction of the beam with the polarising reflector, there are no outer (reflecting) walls.

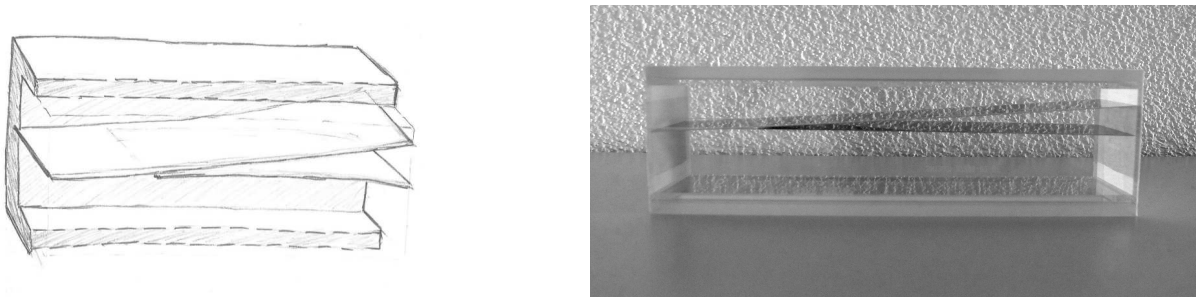

Figure 7.2: Left: First sketch for a frame-overlap filter and polariser for the *Selene* prototype set-up, based on transmission/reflection through/at spiral-curved surfaces. Right: Final device, produced by SwissNeutronics. The glass tube is 215 mm long and has an inner height and width of $50 \times 50\,\mathrm{mm}^2$. The virtual source is to be 170 mm before the entrance (to the left).

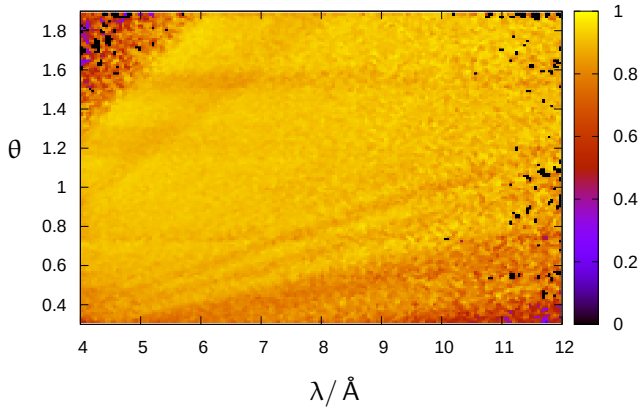

Figure 7.3: Measured polarisation efficiency of the beam filtered by the transmission polariser, transmitted through the *Selene* guide, and *analysed* by a remanent FeCoV/Ti:N supermirror on glass ($10 \times 10\,\mathrm{mm}^2$, $m = 3$). The magnetisation of the analyser was performed with a permanent magnet by hand, i.e. not under optimal conditions. The polarisation was flipped with a RF spin-flipper. All features (lines) pointing towards $\lambda = 0\,\text{Å}$, $\theta = 0°$ originate from the analyser. E.g. the darker triangle in the upper left corner corresponds to $q_z > 0.66\,\text{Å}^{-1}(m = 3)$, and the wide triangle at the bottom to $q_z < 0.16\,\text{Å}^{-1}$. The horizontal structure can be caused by imperfections of the *Selene* guide (mis-alignment) or of the polariser. The dark line at $\theta \approx 0.75°$ is corresponds to the tip of the V-shaped polariser. This map tells that the polariser has an efficiency of at least 90% over an angular range of 1.6° for a source opening of 1 mm.

The technical parameters are $\lambda \in [4, 16]\,\text{Å}$, and $x \in [170, 395]\,\text{mm}$, with x the distance from the focal point. The upper limit is given by the entrance of the prototype *Selene* guide at $x = 400\,\text{mm}$. The divergence to be covered is $\Delta\theta = 1.8°$. The polarising coating is a $m = 4.2$ FeCoV / Ti:N supermirror, covered with Ni to simultaneously act as a low-pass for $\lambda < 16.8\,\text{Å}$. Figure 7.3 shows an early performance test with an improvised set-up.

7.2 Condenser

A convergent beam can be transformed into a parallel beam by deflection on the outside of a parabolically shaped surface, where the focal points coincide. In analogy with light optics this device is called *condenser*, here.

The function for a parabola with the focal point at (0,0), a horizontal axis, and the opening to negative x is

$$y = \sqrt{p^2 - 2px} \tag{7.2.1}$$

p defines the curvature of the parabola, $p/2$ is the distance of the apex from the focal point. The incoming neutron trajectories (pointing to the focal point) are

$$y = x \tan\alpha \tag{7.2.2}$$

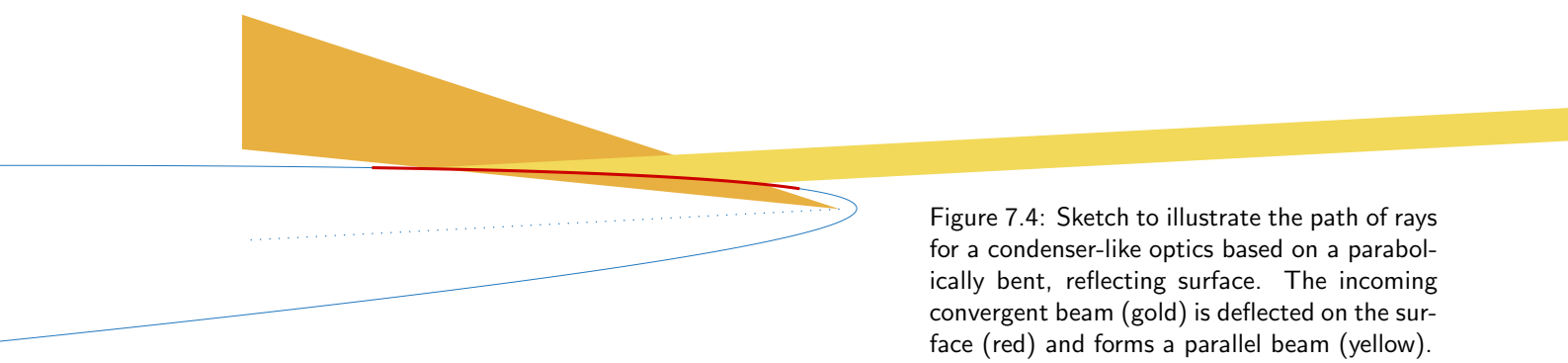

Figure 7.4: Sketch to illustrate the path of rays for a condenser-like optics based on a parabolically bent, reflecting surface. The incoming convergent beam (gold) is deflected on the surface (red) and forms a parallel beam (yellow).

with $-90° < \alpha < 0°$. Both functions intersect at

$$\begin{aligned}
\sqrt{p^2 - 2px_\alpha} &= x_\alpha \tan\alpha \\
x_\alpha^2 \tan^2\alpha + 2p\,x_\alpha - p^2 &= 0 \\
x_\alpha &= \frac{-2p \pm \sqrt{4p^2 + 4p^2 \tan^2\alpha}}{2\tan^2\alpha} \\
&= \frac{p}{\tan^2\alpha}\left(-1 \pm \sqrt{1+\tan^2\alpha}\right) \\
&= \frac{p}{\tan^2\alpha}\left(-1 - \frac{1}{\cos\alpha}\right) \qquad (7.2.3) \\
y_\alpha &= \frac{p}{\tan\alpha}\left(-1 - \frac{1}{\cos\alpha}\right) \qquad (7.2.4)
\end{aligned}$$

It was used that only intersections before the focal point ($x < 0$) are of interest. For a given distance x and angle α the parameter p can be obtained from eqn. 7.2.3:

$$p = \frac{x\tan^2\alpha}{-1 - 1/\cos\alpha} \qquad (7.2.5)$$

The direction of the parallelised beam is given by the parabola axis. The width can be tuned by changing p and thus the distance from the focal point where the deflection occurs.

divergence The divergence of the beam behind the condenser depends on the spot size at the focal position, and on the degree of compression. The latter is a result of Liouville's theorem which states $\Delta y \times \Delta\theta = \text{constant}$.

example To make a convergent beam with $\Delta\theta = 1.5°$ parallel with a beam width of 26 mm, the deflector extends from $x = -2\,000$ mm to $x = -500$ mm, and it has a shape defined by $p = 0.686$. The angle of incidence on the deflector varies from 0.75° to 1.50°. This corresponds to a SM coating of $m = 3$ for $\lambda \geq 5$ Å.

To make the beam parallel in both directions, two subsequent devices (analogue to a Kirkpatrick-Baez mirror), or a nested device (Montel Optics) can be used. The first approach allows to use individually tunable surfaces (adaptive optics) so that beam width and divergence can be adjusted.

7.3 Tele- or wide-angle optics

A beam convergent to one pole of a hyperbola can be reflected on the outside of the hyperbola and focused to its other pole. The reflector thus changes the focal length and acts like a tele optics (as shown in figure 7.5) or as a wide-angle optics.

As for the condensor, the direction of the reflected beam can be varied by tilting the hyperbola main axis. The virtual source size and the shape of the hyperbola determine the resolution.

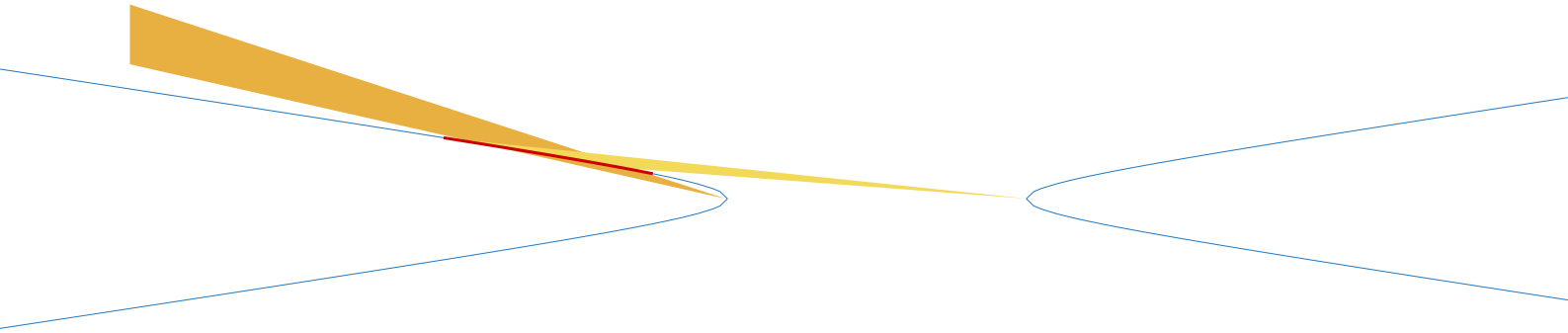

Figure 7.5: Sketch to illustrate the path of rays reflected on the surface of a hyperbolically shaped surface (blue line). The hyperbola has one pole at the focal point of the incoming beam (gold). The beam is redirected to the second pole (yellow).

There is an infinite set of parameters a and b defining a hyperbola

$$\frac{x}{a} - \frac{y}{b} = 1$$

with a distance between the poles of

$$2e = 2\sqrt{a^2 + b^2}$$

so that with adaptive optics it will be possible to tune the beam size for the sample.

GISANS The tele version could be used to focus the beam on the detector rather than on the sample position in both directions. This allows to perform focusing GISANS.

reduction of diffuse background Samples with intrinsic diffuse scattering lead to a more or less homogeneous illumination of the detector with background. If the specular signal is spread over a wide region on the detector, a lot of this background is collected by summation. In case the sample is wide enough (several cm), one can refocus the beam to the detector in the sample plane. The detector area illuminated by the specular signal is strongly reduced (more than an order of magnitude), and so is the contribution of the background.

The objective against the high-intensity specular reflectivity mode, that the high divergence in the scattering plane leads to a high background for samples with a lot of diffuse scattering, is correct. The same is true for the divergence in the sample plane. With the proposed focusing to the detector the latter is reduced so that the resulting contamination of the specular reflectivity should be about the same for the conventional approach (high divergence in the sample plain *to gain intensity* and low divergence in the scattering plane *to reduce background*) and in the high-intensity mode (focusing to the detector in the sample plane *to reduce background* and to the sample in the scattering plane *to reduce counting time and increase the q_z-range*.)

wider q_z-range With the wide-angle set-up the sample together with the focal point moves closer to the guide end, but it experiences a wider divergence. Thus the q_z-range accessible without rocking the sample gets expanded.

8 Boundary Conditions and Consequences

Based on information distributed at IKON3, and on private communications with P. Bentley, K. Anderson, and H. Wacklin, 11. 2012, there are the following boundary conditions to be expected for a *short* reflectometer. Short means of the order of 50 m long or less, i.e. situated in one of the inner guide halls at the ESS.

8.1 Space

- The first 2 m around the moderator are free of any elements.
- Within the target monolith shielding (2 to 6 m) an insert of 210 mm width (but at most forming a 5° wedge) and of 210 mm height can be freely shaped. Optical elements are allowed in the insert. Since there will be a cooled He atmosphere (from moderator up to the end of the monolith) also free-standing Si-wavers can be used.

  The last 500 mm of the monolith might be occupied by a shutter (which can host optical elements).
- Behind the monolith there might be a chopper or other moving parts.
- From the monolith up to a radius of 15 m a common shielding for all instruments will be built. The beam guide can be of any shape and size. There is the option to insert choppers and other devices (most likely accessible from the top).
- At a distance larger than 15 m to the moderator, the individual instrument guide shielding starts. Its length depends on the dose rate caused mainly by fast neutrons (also by secondary processes).
- The *short* instruments will have a 10° wedge-shaped space available. This is necessary to allow for sufficient shielding to prevent cross-talk of background.
- The height differences from moderator to floor are 3 m and 2 m. The hall allowing for high magnetic fields will have the 2 m distance. If needed it is possible to get a lower floor locally.

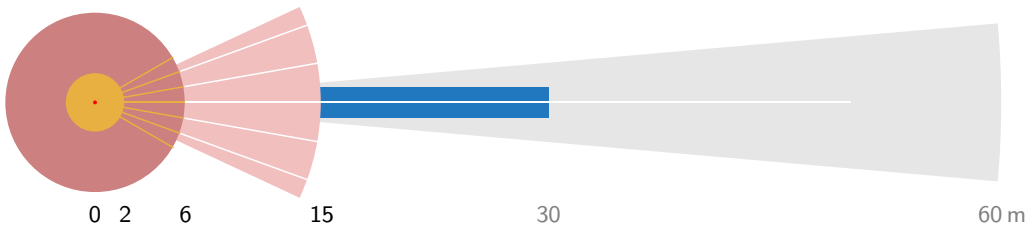

Figure 8.1: Sketch to illustrate the various shielding jackets intended for the source and the instrument. The colours mean: red–moderator, yellow–He-atmosphere, dark red–target-shielding (monolith), light red–common instrument shielding, blue–individual guide-shielding (as far as possible), light gray–10° wedge available for a short instrument.

8.2 Shielding and background

- The target monolith (for the moment) is intended to consist of steel.
- The common instrument shielding will be made of various materials to moderate fast neutrons, convert muons and neutrons, and absorb γ and neutrons.
- The effective direct line of sight from any point of the instrument area to the moderator and target is to be avoided. This means at least 12 m material in the direct line.

  At most half of the length of the guide (shielding) is to have direct line of sight.
- Indirect line of sight has to be avoided, i.e. from outside the shielding no area directly illuminated by the source (moderator and target) is visible. Here the thickness of the shielding material is about 2 m.

8.3 Exclusion of proton prompt

At ISIS second target station and at the SNS the fast neutrons and hard x-rays produced during the proton pulses (or by secondary processes in the shielding) cause problems in the data acquisition. The corresponding STAP members R. Dalgliesh and J. Ankner suggest not to collect data during these times. So it is favourable to tune the instrument length and λ-range in a way to exclude the pulse times without creating holes in the q-range.

For the time being all reflectometers should be developed in a way that the time interval of high fast neutron background is excluded from the measurements.

Following the argumentation of section 2.3.1 the usable wavelength-range for reflectometry starts at about 4 Å to 5 Å for *Selene* guides. An instrument length of some 60 m results in a wavelength-range of e.g. $\lambda \in [5, 10]$ Å. For the ESS baseline parameters this has the consequence that the background burst from the proton pulse appears at the beginning or the end of the used wavelength-range. Further optimisation leads to the situation that the bursts are just outside the required λ-range, as is sketched in figure 8.2.

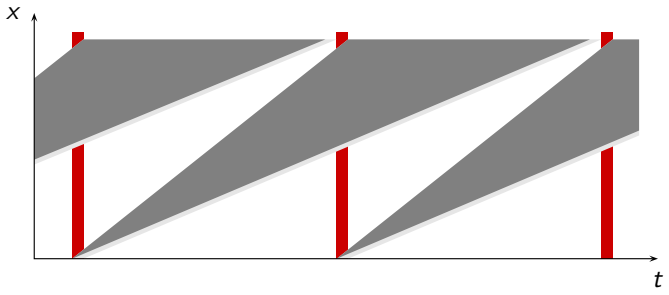

Figure 8.2: Sketch to illustrate how to avoid the influence of the γ and fast neutron burst from the proton pulse hitting the target. The sketch is to scale with period $T = 70$ ms, pulse length $t = 3$ ms, and a sample detector distance of 58 m, i.e. $\lambda \in [5, 9.3]$ Å.

For this scheme, the flight times for the shortest / longest wavelength are $t = 73$ ms / 137 ms (assuming a burst time of 3 ms and a period of 70 ms). For $\lambda_{\text{min}} = 5.00$ Å this leads[1] to an instrument length of $\overline{SD} = 58'400$ mm, and this in turn to $\lambda_{\text{max}} = 9.38$ Å.

8.3.1 Intrinsic resolution

The intrinsic λ-resolution for this instrument is given by the length of the flight path X, and the pulse length τ via

$$\begin{aligned} \frac{\Delta\lambda}{\lambda} &= \frac{\Delta t}{t} \\ \Delta\lambda &= \frac{\tau}{\frac{m}{h} X \lambda}\lambda \\ &= 3\,956 \cdot 10^{-7}\,\text{m}^2\,\text{s}^{-1}\,\frac{\tau}{X} \\ &\approx 0.2\,\text{Å} \qquad \text{for } X = 58.4\,\text{m},\ \tau = 2.85\,\text{ms} \end{aligned}$$

[1] From $E = \frac{mv^2}{2} = \frac{h^2}{2m\lambda^2}$ and $v = \frac{x}{t}$ (with distance x, time t, and neutron mass $m = 1.6745 \cdot 1^{-27}$ kg) follows $x = \frac{h}{m}\frac{t}{\lambda} \approx 3.956 \cdot 10^{-7}\,\frac{\text{m}^2}{\text{s}}\,\frac{t}{\lambda}$.

This leads to

$$\frac{\Delta\lambda}{\lambda} \quad = \quad 4.0\% \ldots 2.1\% \quad \text{for} \quad \lambda = 5\,\text{Å} \ldots 9.4\,\text{Å}.$$

9 Technical Details

9.1 Moving elements

This section gives a preliminary list of translation and rotation stages, sorted by location and purpose. All motion devices besides the guide positioning and alignment are also listed in table 9.1 with estimated ranges, accuracy, and load.

	motion	range	accuracy	load	
apertures	y translation	$0 - 80$ mm	< 1 mm	20 kg	
within ellipses	z translation	$0 - 80$ mm	< 1 mm	20 kg	
	y translation	$0 - 80$ mm	< 0.1 mm	2.0 kg	
	z translation	$0 - 80$ mm	< 0.1 mm	2.0 kg	
beam definition	x translation	$0 \ldots 40$ mm	< 0.1 mm	2 kg	
	z translation	± 20 mm	< 0.1 mm	5 kg	
	tilt	$\pm 5°$	$< 0.01°$	10 kg	
	roll	$\pm 5°$	$< 0.01°$	15 kg	
	x translation	± 20 mm	< 0.01 mm	20 kg	
	y translation	± 20 mm	< 0.01 mm	25 kg	
	ω	$0° \ldots 360°$	$< 0.002°$	30 kg	
	2θ	$\pm 2°$	$< 0.01°$		1)
	x translation	± 100 mm	< 0.1 mm	0.5 t	
	y translation	± 100 mm	< 0.1 mm	0.5 t	
fast aperture	y^+ translation	$0 \ldots 80$ mm	< 0.01 mm	1.0 kg	
	y^- translation	$0 \ldots 80$ mm	< 0.01 mm	1.0 kg	
	z^+ translation	$0 \ldots 80$ mm	< 0.1 mm	1.0 kg	
	z^- translation	$0 \ldots 80$ mm	< 0.1 mm	1.0 kg	
sample stage	z translation	± 20 mm	< 0.1 mm	0.6 t	
	tilt	$\pm 5°$	$< 0.01°$	0.7 t	
	roll	$\pm 5°$	$< 0.01°$	0.7 t	
	x translation	± 20 mm	< 0.01 mm	0.8 t	
	y translation	± 20 mm	< 0.01 mm	0.8 t	
	ω	$0° \ldots 360°$	$< 0.002°$	1.0 t	
	2θ	$-5° \ldots 140°$	$< 0.01°$		2)
	x translation	± 500 mm	< 0.1 mm	1.5 t	
	y translation	± 500 mm	< 0.1 mm	1.5 t	
CCD camera	z translation	$0 \ldots 400$ mm	< 0.01 mm	10 kg	3)

Table 9.1: Parameters for motion control, sorted by locations and purpose., For beam manipulation and sample stage a classical set-up using rotation and translation stages was assumed. 1) rotation of the full second guide section; 2) rotation of the detector arm; 3) accuracy only for the end-position.

9.2 Detector characteristics

According to Richard Hall-Wilton, ESS, it is realistic to expect the following parameters:

resolution:	$0.5 \times 0.5\,\mathrm{mm}^2$	minimum
size:	$500 \times 500\,\mathrm{mm}^2$	maximum

As consequence the highest resolution at $q = 0.01\,\text{Å}^{-1}$ with a sample-detector distance of 6.2 m, limited by the detector is

$$\begin{aligned} \Delta\theta &= \arctan[0.5/6200] \\ &\approx 0.005^\circ \\ \theta &= 0.43^\circ \quad \text{for } \lambda_{max} = 9.4\,\text{Å} \\ \Delta\theta/\theta &= 1.1\% \end{aligned}$$

position Since the length of the flight path is optimised to avoid the proton pulse time it is not advisable to change the sample-detector distance. So it could be mounted on a 2θ arm of fixed length, with a evacuated, frustum-shaped nozzle pointing towards the sample.

size A width of 500 mm results in an angle-range of 4.6°. This is three times the maximum divergence of the beam incident on the sample. The excess area in the scattering plane is needed for off-specular measurements. When using λ-θ-encoding, the specular beam scans over the inner 1.5°, so that effectively only another $\pm 1.5^\circ$ are available.

Normal to the scattering plane the maximum area of interest is only 170 mm wide. So the expected minimum detector size is

$$\begin{aligned} \text{width} \quad y &= 500\,\text{mm} \\ \text{height} \quad z &= 170\,\text{mm} \end{aligned}$$

resolution In the scattering direction (i.e. horizontally) a high resolution is required. Ideal would be a pixel-size of 0.5 mm or less. The lower limit is given by the effective sample size of a fraction of a mm.

Normal to the scattering plane (vertical) a much coarser resolution can be accepted. In an ideal case no position sensitivity is needed at all. A real effect that might still require some resolution are the suppression of background *outside* the region of interest. And also to align the *roll* of the sample (tilt around the x-axis) a 2-dimensional detector would be favourable. But this task could also be performed with an optional CCD-camera.

$$\begin{aligned} \text{horizontal} \quad \Delta y &\leq 0.5\,\text{mm} \\ \text{vertical} \quad \Delta z &\in [\Delta y, \infty] \end{aligned}$$

rate per pixel Since the pixel size is not defined, here the maximum rate per mm^2 is given. It was obtained by assuming a perfectly reflecting reference sample of $10 \times 10\,\mathrm{mm}^2$ and full beam divergence. The rate[1] per pixel varies in the range

$$\begin{aligned} 10^5\,\mathrm{s}^{-1}\text{Å}^{-1}\mathrm{mm}^{-1} \quad &\text{for} \quad \lambda = 5\,\text{Å} \\ 3 \cdot 10^4\,\mathrm{s}^{-1}\text{Å}^{-1}\mathrm{mm}^{-1} \quad &\text{for} \quad \lambda = 9.4\,\text{Å} \end{aligned}$$

total rate This quantity was obtained by simulation with the same setting as mentioned above, but by integrating over the full detector. The maximum specularly illuminated area is $2.7 \cdot 10^4\,\mathrm{mm}^2$, but the illumination is not homogeneous. The maximum integral rates are

$$\begin{aligned} 5 \cdot 10^8\,\mathrm{s}^{-1}\text{Å}^{-1} \quad &\text{for} \quad \lambda = 5\,\text{Å} \\ 2 \cdot 10^8\,\mathrm{s}^{-1}\text{Å}^{-1} \quad &\text{for} \quad \lambda = 9.4\,\text{Å} \end{aligned}$$

[1] This is the maximum instant rate, not averaged over one pulse. The wavelength band width is 0.2 Å at the detector position, 58.4 m from moderator [→8.3.1].

homogeneity The detector images are normalised by division by a reference measurement. Already a relative misalignment of 0.005° leads to a shift of one (0.5 mm) pixel. It is thus crucial that the detector area is homogeneous (if necessary after pixel-wise normalisation) on the order of 1%.

stability The intended measurement scheme requires a reference for each detector image obtained with a sample. To save measurement time, there will be a set of reference sample sizes and orientations available, obtained with standard samples. This requires that the homogeneity of the detector does not change with time (over months), and that the total sensitivity can be detected continuously, so that a renormalisation of the reference is possible.

dynamic range The dynamic range of the detector must be quite high since at the same time one can expect maximum flux on some area of the detector, while it drops by 6 orders of magnitude (or more) for high-q_z or off-specular regions. This can be seen in figure 2.8.

A signal of 10^{-8} relative to the full intensity given by a *small* sample has to be measurable. Small here means 2 orders of magnitude smaller than the reference mentioned above. The signal will then be of the order $5 \cdot 10^8\,\mathrm{s}^{-1}\text{Å}^{-1} \times 10^{-2}\,10^{-8}$, with $\Delta\lambda = 0.2\,\text{Å}$. Thus the integral noise of the detector should be below $10^{-2}\,\mathrm{s}^{-1}$.

9.2.1 Cross-talk

All measurements with the *Selene* prototype were performed with an EMBL wire detector. Recent (08. 2013) tests to estimate the contribution of air-scattering to the background revealed that all noteworthy background for these measurements is detector-intrinsic.

The test compared the signal on the detector obtained with a highly collimated beam with various set-ups, namely a flight tube filled with air with and without Al windows, and filled with Ar, all with the detector slit fully open. And a reference with the detector slit closed to 5 mm. The only sizeable effect was the intensity gain when using Ar due to the reduced scattering on N_2. Figure 9.1 shows the horizontally integrated intensity as a function of the height (in terms of detector angle). The direct beam can be clearly seen at $\theta \approx -0.05°$. The background sets in some 2.5 orders of magnitude below the peak intensity and drops down to 4 orders at the corners. The detector slit opening corresponds to $\Delta\theta \approx 0.2°$

The test-situation is not so far from a typical situation in the high-intensity-mode or the λ-θ-encoding-mode. One part of the detector is illuminated by the totally reflected beam, while other parts should record a signal down to 6 (or even more) orders of magnitude below.

Presumably this cross-talk is responsible for the finite-background problems we have seen in the experiments with the *Selene* prototype.

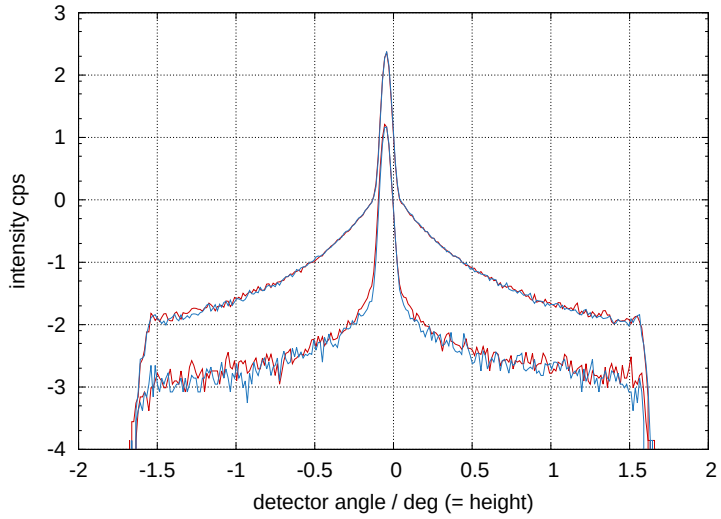

Figure 9.1: Intensity distribution on the Amor area detector integrated horizontally. The detector was illuminated with a vertically collimated beam, corresponding to the sharp peak. For the red curves, the detector slit was completely open, for the blue it was closed to shade the area outside the beam. The upper curves are obtained by integrating λ from 3 Å to 5 Å, the lower curves by integrating from 8 Å to 10 Å.

10 Measurement Schemes and Data Reduction

This chapter gives a more detailed description of the data collection and processing for the three principle operation modes.

- almost conventional reflectometry [→10.2]
- λ-θ-encoding reflectometry [→10.3]
- high-intensity specular reflectometry [→10.4]

For these modes simulations were performed with a standard sample, presented in chapter 11. Further simulations to highlight the principle and performance of the individual modes are presented below.

10.1 General aspects

10.1.1 Sample alignment

A narrow slit behind the end of the guide ensures a small divergence so that the situation is similar to a conventional TOF reflectometer. The low-divergent beam allows to align the sample by alternating rocking scans and z-scans[1]. The accuracy is given by the divergence and for larger samples by the footprint. The only difference from conventional TOF reflectometers is that the beam converging at the centre of rotation ideally does not have any parallel components. A z-scan at $2\theta = 0°$ to find the absorbing substrate at the half-shaded beam is thus modified. At $\theta = 0°$ one has the end of the absorbing substrate leading to half the intensity, and not the sample centre. For small samples this can be neglected, for large samples one still gets the approximate position.

For a high precision alignment an additional CCD-based detector can be used. It has much higher resolution and fast feed-back (no TOF analysis is necessary).

Depending on (the transparency of) the sample environment one can use optical light to pre-align the sample. The divergent white light is coupled into the beam before the virtual source. Besides gravity effects, this follows the same trajectories as the neutrons, creating a spot where the centre of rotation should be. This method is used on Amor and on the *Selene* prototype with large success.

10.1.2 Normalisation and reference measurement

In principle, the best normalisation is obtained by using a perfectly reflecting reference of the same shape as the sample. Each measurement has to be performed with both so that at the end the ratio of the measured intensities $I^s(q_z)$ and $I^r(q_z)$ is the ratio of the reflectivities of the samples. And because $R^r = 1\,\forall q_z$ this is the reflectivity of the sample. All inhomogeneities of the detector efficiency and due to absorbing elements in the beam path are compensated.

The snag in it is that there is no perfectly reflecting sample. For rather small q_z one can use a supermirror of known reflectivity $R^r(q_z)$ for the normalisation. The ratio of the measurements then has to be corrected:

$$R(q_z) = \frac{I^s(q_z)}{I^r(q_z)/R^r(q_z)}$$

This method is restricted to $q_z \approx 0.22\,\text{Å}^{-1}$, i.e. a reference with a $m = 10$ supermirror coating.[2] The reflectivity of this reference is not high, but as long as it is smooth up to the critical angle the imperfection

[1] Here, z is in the sample coordinate system, i.e. normal to the sample surface

[2] A $m = 10$ supermirror with a reflectivity of at least 1% can be realised according to SwissNeutronics.

just leads to longer counting times.[3] If the reference has a different shape or size than the sample, an additional illumination correction has to be applied. This correction can be obtained analytically or by simulation. The illuminated detector area is the same, so that inhomogeneities there are still compensated.

For higher q_z this approach has to be modified: The reference is measured at low q_z, only, but is used to normalise also the high-q_z measurements of the sample. This requires another illumination correction, and the normalisation is not performed on the basis of q_z but by using detector pixels (or something similar). One has to take care that all measurements illuminate the same area on the detector.[4]

To save beam-time and to be independent of the sample size, it might be possible to use synthetic references obtained e.g. by McStas simulations. These have to be compared to sporadically performed measurements on a set of real reference samples to take inhomogeneities of the beam (caused by the *Selene* guide and optics) and the detector (and a possible variation of these with time) into account. This has not yet been tested.

10.1.3 Data reduction

In the following the reduction of the raw data for specular reflectivity measurements is presented. The off-specular measurements are treated analogue, but with a projection to $R(q_y, q_z)$ rather than to $R(q_z)$.

raw data The measurements each lead to a vector with a data triple for each detected neutron. This is time-of-flight t, and the position on the area detector y, z. For further data treatment these events are binned with $\Delta t/t = \text{const.}$, Δy and Δz. This gives the matrix $\mathbf{I}(y, z, t)$. In most cases (GISANS is an exception), there is no information expected in y direction so that one can project it to $\mathbf{I}(z, t)$. With the known distances from moderator or sample to the detector the instrument parameters z and t can be converted to θ and λ, respectively. Thus one gets the matrix

$$\mathbf{I}^{\mathrm{s}}(\lambda, \theta) \quad : \quad I^{\mathrm{s}}_{\lambda,\theta}$$

and assuming Poisson statistics also the corresponding error matrix

$$\Delta\mathbf{I}^{\mathrm{s}}(\lambda, \theta) \quad : \quad \Delta I^{\mathrm{s}}_{\lambda,\theta} \quad = \quad \sqrt{I^{\mathrm{s}}_{\lambda,\theta}}$$

reference and normalisation In analogy one gets the matrices for the reference by measurement or simulation as mentioned above:

$$\begin{aligned} \mathbf{I}^{\mathrm{r}}(\lambda, \theta) \quad &: \quad I^{\mathrm{r}}_{\lambda,\theta} \\ \Delta\mathbf{I}^{\mathrm{r}}(\lambda, \theta) \quad &: \quad \Delta I^{\mathrm{r}}_{\lambda,\theta} \end{aligned}$$

where the error of the reference $\Delta\mathbf{I}^{\mathrm{r}}(\lambda, \theta)$ depends on the way $I^{\mathrm{r}}_{\lambda,\theta}$ was obtained. $I^{\mathrm{r}}_{\lambda,\theta}$ already contains the scaling factors due to varying sample size, sample orientation and counting time, if applicable. Element-wise division leads to the reflectivity matrix

$$\begin{aligned} \mathbf{R}(\lambda, \theta) \quad &: \quad R_{\lambda,\theta} \quad = \quad \frac{I^{\mathrm{s}}_{\lambda,\theta}}{I^{\mathrm{r}}_{\lambda,\theta}} \\ \Delta\mathbf{R}(\lambda, \theta) \quad &: \quad \Delta R_{\lambda,\theta} \quad = \quad R_{\lambda,\theta} \sqrt{\left(\frac{\Delta I^{\mathrm{s}}_{\lambda,\theta}}{I^{\mathrm{s}}_{\lambda,\theta}}\right)^2 + \left(\frac{\Delta I^{\mathrm{r}}_{\lambda,\theta}}{I^{\mathrm{r}}_{\lambda,\theta}}\right)^2} \end{aligned}$$

[3] All measurements performed with the prototype on BOA and Amor at PSI were normalised this way up to $q_z \approx 0.1\,\text{Å}^{-1}$ with $m = 5$ or $m = 6$ supermirrors on silicon or on glass.

[4] This approach worked fine for the measurements on Amor for $q_z > 0.1\,\text{Å}^{-1}$.

projection to $R(q_z)$ Each matrix element $R_{\lambda,\theta}$ can be associated with a q_z, where the mapping is not bijective. But the matrices $\mathbf{R}(\lambda,\theta)$ and $\Delta\mathbf{R}(\lambda,\theta)$ can be projected[5] on vectors $\mathbf{R}(q_z)$ and $\Delta\mathbf{R}(q_z)$ with a q_z binning of $\Delta q_z/q_z = c = \text{const}$.

$$\begin{aligned}
\mathbf{R}(q_z) \;:\; R_{q_z\,n} &= \sum\nolimits_{\lambda,\theta:\, q_{z\,n} \le q_{z\,\lambda,\theta} < q_{z\,n+1}} p_{\lambda,\theta}\, R_{\lambda,\theta}\, M_{\lambda,\theta} \\
\Delta\mathbf{R}(q_z) \;:\; \Delta R_{q_z\,n} &= \sqrt{\sum\nolimits_{\lambda,\theta:\, q_{z\,n} \le q_{z\,\lambda,\theta} < q_{z\,n+1}} \left(p_{\lambda,\theta}\,\Delta R_{\lambda,\theta}\right)^2 M_{\lambda,\theta}} \qquad \text{or} \\
\Delta R_{q_z\,n} &= \left(\sum\nolimits_{\lambda,\theta:\, q_{z\,n} \le q_{z\,\lambda,\theta} < q_{z\,n+1}} \left(\frac{M_{\lambda,\theta}}{\Delta R_{\lambda,\theta}}\right)^2\right)^{-\frac{1}{2}}
\end{aligned}$$

with the q_z bin

$$q_{z\,n} = q_{z\,0}\,(1+c)^n$$

the weights

$$p_{\lambda,\theta} = \frac{\frac{1}{\Delta R_{\lambda,\theta}}}{\sum_{\lambda',\theta':\ldots} \frac{M_{\lambda',\theta'}}{\Delta R_{\lambda',\theta'}}}$$

and the mask

$$\mathbf{M}(\lambda,\theta) \;:\; M_{\lambda,\theta} = \begin{cases} 1 & \text{for} \quad \theta(\lambda) - \Delta\theta(\lambda)/2 \le \theta \le \theta(\lambda) + \Delta\theta(\lambda)/2 \\ 0 & \text{else} \end{cases}$$

The mask $\mathbf{M}(\lambda,\theta)$ guarantees that the summation is performed only over a defined range in the θ-λ-space where specular reflectivity is expected. The functions $\theta(\lambda)$ and $\Delta\theta(\lambda)$ depend on the operation mode.

resolution In analogy to $\Delta\mathrm{R}(q_z)$ a resolution vector $\Delta\mathrm{q_z}(q_z)$ can be defined, based on the λ uncertainty dominated by the pulse length τ and the angular resolution Δθ given by the spatial resolution of the detector. This leads to a matrix

$$\Delta\mathbf{q_z}(\lambda,\theta) \;:\; \Delta q_{z\,\lambda,\theta} = \frac{4\pi\sqrt{\cos^2\theta\,\Delta\theta^2 + \sin^2\theta\,\Delta\lambda^2/\lambda^2}}{\lambda}$$

For *Estia* with an assumed detector resolution of 0.5 mm the corresponding uncertainties are

$$\begin{aligned}
\Delta\lambda &= \tau\,\frac{h}{m\,\overline{\mathrm{MD}}} \\
&\approx 0.2\,\text{Å} \\
\Delta\theta &= \arctan\frac{\Delta y}{\overline{\mathrm{SD}}} \\
&\approx 0.0045^\circ
\end{aligned}$$

with the neutron mass m, the moderator-to-detector distance $\overline{\mathrm{MD}} = 58\,400$ mm, and the sample-to-detector distance $\overline{\mathrm{SD}} = 6\,200$ mm.

The resolution vector is then obtained by summation

$$\Delta\mathbf{q_z}(q_z) \;:\; \Delta q_{z\,n} = \sum\nolimits_{\lambda,\theta:\, q_{z\,n} \le q_{z\,\lambda,\theta} < q_{z\,n+1}} p_{\lambda,\theta}\,\Delta q_{z\,\lambda,\theta}\, M_{\lambda,\theta}$$

[5] Two possibilities to calculate $\Delta R_{q_z\,n}$ are given. The first is derived from the Gaussian error propagation, but it might lead to the confusing situation that increasing the counting statistics with a statistically less robust additional data point leads to an increase of the error. The second approach *behaves* as expected: summing m data points of same statistical weight decreases the error by $1/\sqrt{m}$, and for a strong imbalance in weights, the error of the sum is always smaller than all the individual errors.

merging of reflectivity curves The procedure described so far deals with the reduction of one measurement. In almost all relevant cases the interesting q_z-range can not be covered with one measurement only, so that one ends up wit a set of vectors $\mathbf{R}^\omega(q_z)$, $\Delta\mathbf{R}^\omega(q_z)$ and $\Delta\mathbf{q_z}^\omega(q_z)$ for each sample orientation ω. If all data sets were projected to the same q_z-grid, i.e. with the same $q_{z\,0}$ and c, they can be merged:

$$\begin{aligned}
\mathbf{R}^\Sigma(q_z) \quad &: \quad R^\Sigma_{q_z n} \quad = \quad \sum_\omega p^\omega_{q_z n} R^\omega_{q_z n} \\
\Delta\mathbf{R}^\Sigma(q_z) \quad &: \quad \Delta R^\Sigma_{q_z n} \quad = \quad \left(\sum_\omega \left(\frac{1}{\Delta R^\omega_{q_z n}} \right)^2 \right)^{-\frac{1}{2}} \\
\Delta\mathbf{q_z}^\Sigma(q_z) \quad &: \quad \Delta q^\Sigma_{z\,n} \quad = \quad \sum_\omega p^\omega_{q_z n} \Delta q^\omega_{z\,n} \\
p^\omega_{q_z n} \quad &= \quad \frac{\frac{1}{\Delta R^\omega_{q_z n}}}{\sum_{\omega'} \frac{1}{\Delta R^{\omega'}_{q_z n}}}
\end{aligned}$$

10.2 Almost conventional reflectometry

measurement scheme This mode corresponds to the conventional TOF reflectometry, where the beam divergence and footprint size are defined by slits. The angle of incidence and the divergence are constant for the duration of one pulse. Using the *Selene* guide the footprint is defined by the virtual source. For adjusting the divergence one slit (the aperture) behind the last guide element is sufficient.

Due to the analogy with conventional TOF reflectometers, the data collection, normalisation and further treatment for one angle of incidence follow exactly the procedure used there.

An additional feature when using a wide divergence cut down by a narrow aperture is that by moving this aperture in between measurements, one can change θ without rotating the sample.

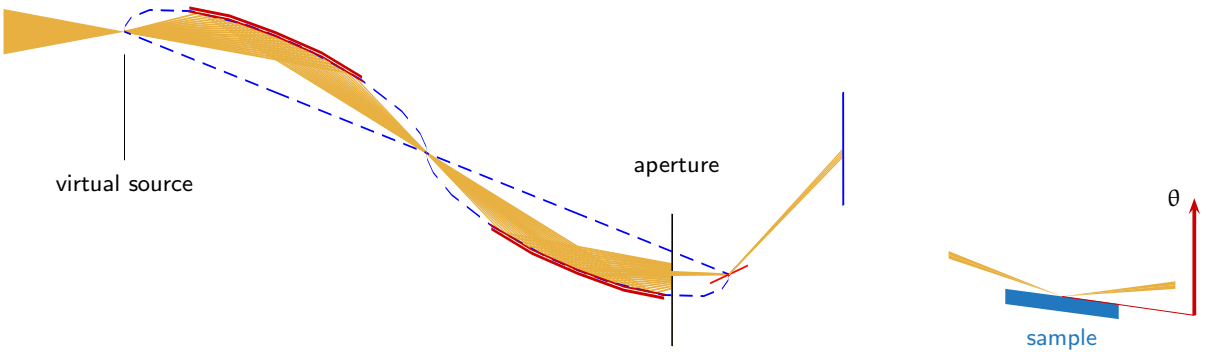

Figure 10.1: Sketch to illustrate the operation scheme: the beam (gold) is transported with the full divergence and without chopping to the end of the guide system. There an aperture (black) defines Δθ, and its position together with the sample orientation ω also the angle of incidence θ. The beam footprint on the sample is defined by size and orientation of the virtual source.

10.2.1 Data acquisition

The width of the q_z-range covered in one measurement with constant θ is rather small (given by $\lambda_{max}/\lambda_{min} = 1.88$). Thus in most cases several sample orientations are needed, which results in longer measurement times due to the movement of the detector. A possible combination of angles of incidence θ with 4% overlap is given in table 10.1.

The wide divergence of the incoming beam opens the opportunity to cover the first 4 angles by moving the aperture rather than by rocking sample and detector. The actual counting times will stay the same, but the switching between the settings is much faster (a few pulses might be lost by repositioning the aperture).

q_z / Å^{-1}	θ / deg	ω / deg	ω / deg	offset / deg
0.005 → 0.009	0.21	−1.04	−0.40	−0.64
0.009 → 0.017	0.39	−0.86		−0.46
0.016 → 0.030	0.69	−0.56		−0.16
0.029 → 0.055	1.25	0.00		+0.40
0.052 → 0.099	2.25	1.00		
0.094 → 0.178	4.05	2.80		
0.170 → 0.320	7.29	6.04		
0.306 → 0.575	13.12	11.87		
0.551 → 1.036	23.62	22.37		

Table 10.1: q_z-ranges covered with one sample orientation. The third column gives the corresponding angle of incidence θ and the forth column the sample tilting with respect to the long half axis of the *Selene* guide, ω. The wide divergence of the beam incident on the aperture allows within limits for changing θ by moving the aperture. This is illustrated in columns 5 (ω) and 6 (offset of the aperture). The limit for the offset is ±0.75°.

10.2.2 Discussion

This is the method of choice if off-specular scattering is to be measured, or in cases when the background caused by off-specular or diffuse scattering has to be separated or reduced.

The performance of *Estia* in this mode is expected to be very close to other concepts since the beam intensity and thus the measurement times are essentially given by the brilliance transfer of the guide.

The instrument-intrinsic resolution $\Delta\lambda/\lambda$ varying from 2% to 4% between 9.4 Å and 5 Å leads to a saw-tooth-like shape of the resolution function of the full measurement (see figure 11.3 d). For all measurements requiring moderate to low resolution (which is the by far largest fraction) this is completely fine [→10.5.3]. For higher resolution the λ-θ-encoding mode described in the next section has to be chosen.

10.3 λ-θ-encoding reflectometry

The strengths of the λ-θ-encoding are the wider q_z-range accessible with one angular setting, a possible constant $\Delta q/q$, and eventually the *nicer* off-specular area, compared to the almost conventional mode.

the measurement scheme There are (at least) two possibilities to obtain a λ-θ-encoding: either by using the pulsed structure and varying the angle of incidence θ with time - and thus with λ. Or to spectraly analyse the beam (no pulsed beam is needed) e.g. by reflecting on a multilayer monochromator, or by refraction using a prism [32].

scanning aperture The divergence-defining aperture behind the guide exit scans across the convergent beam in the direction of the sample normal for each pulse and thus creates a λ-θ-encoding. Figure 10.2 shows the principle. The aperture position defines $\theta(\lambda \propto t)$. For covering a wide q_z-range it should be located at the high-θ edge at the time the 5 Å neutrons arrive and at the low-θ edge for 9.4 Å. The aperture opening defines Δθ. Thus a variation of the slit-width Δy with time can be used to realise $\Delta\theta/\theta = \text{const}$, or more sophisticated, $\Delta q/q = \sqrt{(\Delta\lambda/\lambda)^2 + (\Delta\theta/\theta)^2} = \text{const}$, where $\Delta\lambda = \text{const} \approx 0.2$ Å here.[6]

As long as both blades forming the aperture are in one plane, the resolution $\Delta\lambda/\lambda$ is not affected. By separating the blades along the flight direction x one can realise a set-up analogue to the blind double chopper concept by Ad van Well [33]. Looking at one neutron trajectory (and assuming a continuous beam for the beginning), the two blades create a pulse with $\Delta\lambda/\lambda = \Delta x_a/x_{ad} = \text{const}$, where x_{ad} is the distance from the aperture mid-point to the detector, and Δx_a is the separation of the blades. The same is true for any trajectory as long as the edges of the blades are exactly in line with the sample at all times. I.e. they move with slightly different speeds. With the continuous beam this is a TOF set-up with time-zero varying with angle of incidence θ. With the pulsed beam and coupling θ to λ the band-width of the beam arriving at the aperture is restricted

[6] Solving this equation for Δθ gives (l is the slit-sample distance):

$$\begin{aligned}
\Delta\theta(t) &= \theta(t)\sqrt{\left(\frac{\Delta q}{q}\right)^2 - \frac{\Delta\lambda^2}{(\lambda_{min} + (\lambda_{max} - \lambda_{min})(\theta(t) - \omega + \epsilon)/\Delta\theta_{beam})^2}} \\
&\approx \arctan\frac{\Delta y(t)}{l} \\
\theta(t) &= \omega + \epsilon + \frac{\Delta\theta_{beam}}{2} + \frac{\lambda(t) - \lambda_{min}}{\lambda_{max} - \lambda_{min}}\Delta\theta_{beam} \\
&= \omega + \arctan\frac{y(t)}{l}
\end{aligned}$$

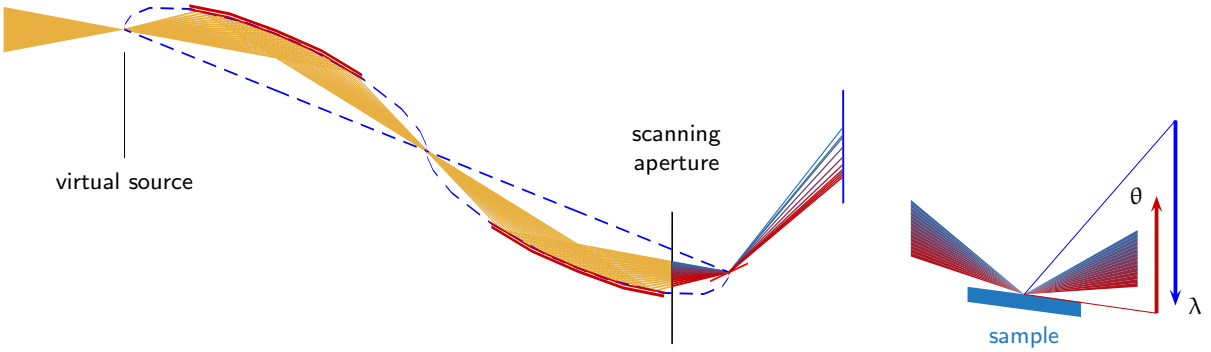

Figure 10.2: Sketch to illustrate the operation scheme: the beam (gold) is transported with the full divergence and without chopping to the end of the guide system. As in the conventional mode [→10.2], a slit (black) defines $\Delta\theta$ and together with the sample orientation ω also the angle of incidence θ. But the opening and position change during the passing of each pulse. This way high θ can be related to low λ and vice versa.

to $\Delta\lambda = 0.2\,\text{Å}$, which is the resolution of the encoding. The latter affects only the off-specular resolution of the measurement.

Given the intrinsic resolution of $\leq 4\%$, a constant $\Delta\lambda/\lambda$ is only useful for 1% or 2%, which corresponds to a separation $\Delta x_a = 84\,\text{mm}$, or 168 mm, respectively.

spectral analysis using a multilayer A ML monochromator at or before the virtual source encodes the wavelengths of the neutrons in the final angle of the monochromator.[7] For small θ one gets $\theta \propto \lambda$. The specular reflectivity from the sample then leads to a diagonal streak in $I(\lambda, \theta)$ on the detector, so that off-specular scattering can be measured. Figure 10.3 shows *snap-shots* of the beam-distribution within the guide and at the sample.

The resolution in q_z is essentially given by the ML monochromator and can reach 2%, while the TOF resolution influences Δq_x. So this mode could be realised without any chopper.

The guide geometry, its coating and the wavelength-range define $\Delta\theta$ [→6.1], i.e. for $\lambda \in [5, 9.4]\,\text{Å}$ and $\Delta\theta = 1.5°$ one gets $m \approx 3.4$ with $\theta \in [1.7°, 3.2°]$. A plateau of total reflection ($m \leq 1$) results in $\theta \leq 1°$ for the same λ-range. Thus totally reflected neutrons do not reach the guide.

A ML monochromator leads to an illumination of the *off-specular region* on the detector by diffuse and off-specular scattering at the multilayer, but also by specular scattering away from the Bragg condition. This can be seen in figure 2.8. The off-specular contribution can be suppressed by the virtual source diaphragm if the monochromator is located before it. An additional scanning aperture the sample (see above) can be used to filter the unwanted specular intensity from the monochromator. This combination allows for a clean beam and a high and constant resolution.

10.3.1 Data acquisition

Also the data acquisition follows the scheme of the almost conventional reflectometry. Only the number of q_z-ranges is reduced, and the counting times are increased. Table 10.2 gives a set of possible orientations ω and the related θ- and q_z-ranges.

ω / deg	θ_{min} / deg	θ_{max} / deg	$q_{z\,min}$ / Å^{-1}	$q_{z\,max}$ / Å^{-1}
−0.4	0.1	1.6	0.003	0.068
1.7	2.2	3.7	0.052	0.160
5.0	5.5	7.0	0.128	0.305
10.0	10.5	12.0	0.253	0.522

Table 10.2: Sample orientations ω and related θ- and q_z-ranges as used for the simulations shown below.

[7] In principle one could use the monochromator itself as the virtual source: It has to have the shape and orientation of the sample or smaller for under-illumination. But in this case all scattering from the monochromator, specular and off-specular, is focused to the sample and results in background in the off-specular signal from the sample.

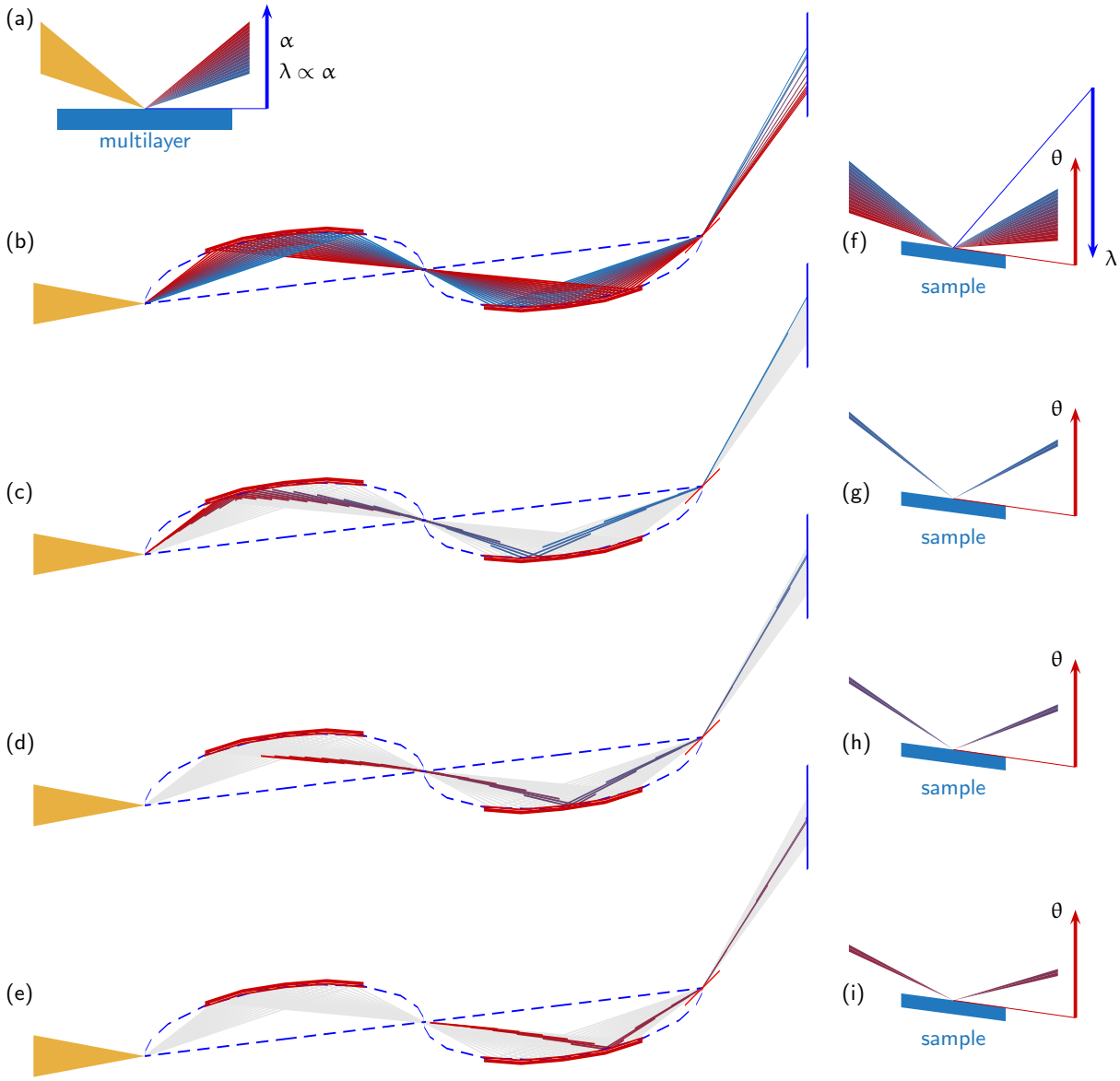

Figure 10.3: Illustration of the principle of the λ-θ-encoding. A convergent white (pulsed) beam is spectral analysed by a ML monochromator (a). The beam then propagates to the sample keeping the relation between λ and θ (b). For a pulsed beam at any time an almost monochromatic beam is impinging on the sample, where θ and $\lambda \sim \theta$ vary with time. The sketches (c) to (e) show snap-shots of the beam within the *Selene* guide system and after the sample. In (f) to (i) the corresponding situation on the sample is shown.

Figure 10.4 shows a simulated $I(\lambda, \theta)$-map for $\omega = 5°$. The sample is a Ni/Ti multilayer with artificial off-specular scattering[8] The diagonal specular streak is clearly visible. Its width is given by the opening of the scanning aperture. The Bragg peaks show the resolution for the specular intensity to be oriented along lines originating from $(\lambda = 0, \theta = 0)$. The visible off-specular Bragg-sheets are inclined with respect to these.

[8] The specular reflectivity was simulated with EDXR [34] The off-specular signal is *generated* by convolution of the specular reflectivity $R(q_z)$ with 2 Gaussian functions $R(q_x, q_z) = R(q_z) * (g_1(q_x) + g_2(q_x))$. with a cut-off at the sample horizon. A bending of the Bragg sheets, Yoneda wings and the low-intensity region between Yoneda and horizon are not produced this way. Within McStas this folding is achieved by randomly adding a q_{xy} component, but with a Gaussian probability distribution centred at $q_{xy} = 0$.

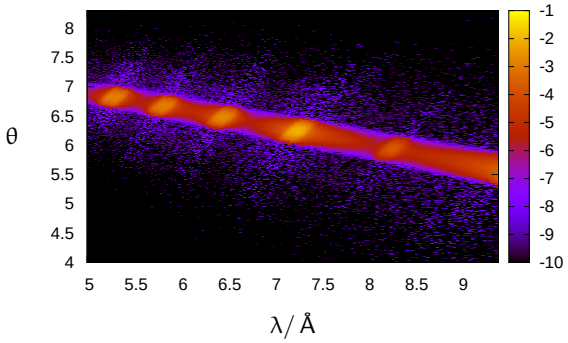

Figure 10.4: Intensity-map $\log_{10}[I(\lambda,\theta)]$ of the NiTi multilayer for $\omega = 5°$. The map is already corrected for $I(\lambda)$ of the incoming beam.

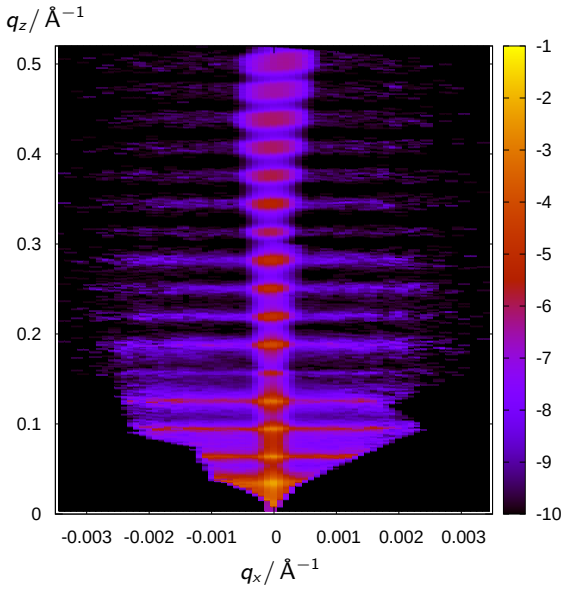

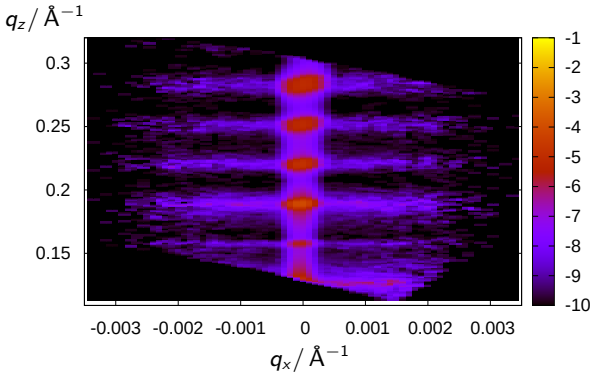

Figure 10.5: Intensity-maps $\log_{10}[I(q_x, q_z)]$ of the NiTi multilayer for $\omega = 5°$ (top), and for all sample orientations given in table 10.2, obtained by summation over the individual maps (left). There is no total reflection plateau visible, here. This is a result of the insufficient computing statistics of the presented map.

10.3.2 Normalisation and integration

Normalisation for the off-specular region is a bit more complicated than discussed in the general part for specular reflectometry because there is no reference sample with a well-known high-intensity off-specular scattering.

Most likely one has to use the specular reference to also scale the off-specular region, taking inhomogeneities of the detector into account. An alternative, but time-consuming approach is to perform an ω-scan with the reference sample. After illumination correction this mimics an off-specular signal with specular intensity, and the latter is known.

Here, for normalising the simulations a perfect reference sample was assumed, and the *measurement* was repeated without the scanning aperture. Figure 10.5 shows the $I(q_x, q_z)$-maps obtained for the four ω orientations, and figure 10.6 the resulting $R(q_z)$ curves.

10.3.3 Discussion

The λ-θ-encoding mode allows to cover the most often used q_z-ranges with 2 to 4 sample orientations. With the encoding performed by a co-planar scanning aperture the off-specular region up to $q_x \approx \pm 3 \cdot 10^{-3}\,\text{Å}^{-1}$ is accessible. The varying resolution from 2% to 4% for each range results in a mismatch in the overlapping regions. For a consistent data treatment the individual measurements should be convoluted to constant 4% before merging and comparison to a simulated curve.

The main outcome of the simulation is that a good separation of specular and off-specular reflectivity can be reached with the λ-θ-encoding. The number of angular settings to cover $q_z \in [0.01, 0.5]\,\text{Å}^{-1}$ is reduced to 4 relative to the conventional mode needing 7 settings (with 10% overlap).

The next step will be to use an aperture with shifted blades, allowing for a constant high resolution (for the cost of longer counting time).

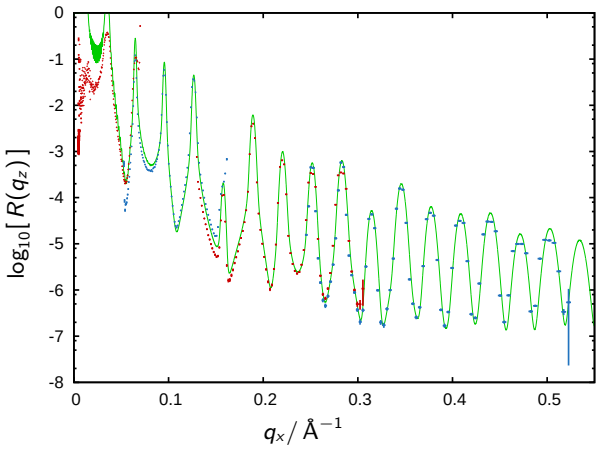

Figure 10.6: $R(q_z)$ of the NiTi multilayer, obtained from the maps shown in figure 10.5 with a binning of $\Delta q/q = 1\%$. The green line is the initial reflectivity convoluted to $\Delta q/q = 2\%$. The data set for $\omega = -0.4°$ clearly shows the insufficient computational statistics. The other data points show a systematic tilt to lower intensities for small q_z. This originates from an improper choice of the Gaussian, widening the specular intensity in q_x direction. This width is larger than the 2% resolution used for data analysis, and thus part of the specular intensity is missing.

10.4 High-intensity specular reflectometry

the measurement scheme The full beam leaving the *Selene* guide is directed to the sample. The reflected beam is measured with an area-sensitive detector, who's distance and resolution defines the angular resolution $\Delta\theta$ (see figure 10.7). Each intensity curve obtained by integrating over the detector normal to the scattering plane for a given position along the scattering vector (i.e. a certain θ) corresponds to one TOF measurement. This is illustrated in figure 10.8.

The increase of specularly reflected intensity is about an order of magnitude with respect to the conventional set-up, or with the λ-θ-encoding. The price to be payed is that the off-specular resolution gets completely lost. The off-specular scattering corresponding to one θ-channel forms a background for all other channels. Most likely there is no way to de-convolve the specular and the off-specular signals.

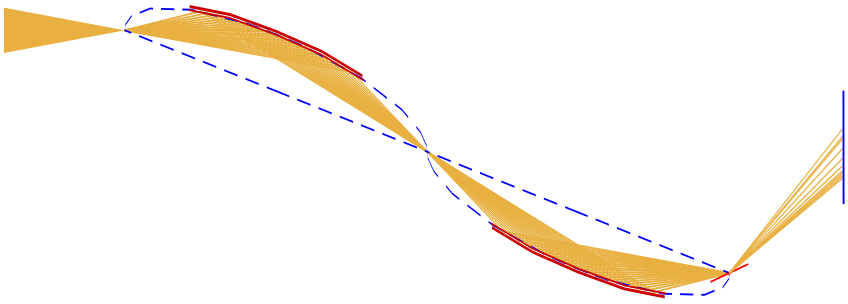

Figure 10.7: Sketch to illustrate the high-intensity specular reflectivity operation mode.

10.4.1 Simulation

Data acquisition and reduction is shown below for a simulated experiment. The corresponding real life experiment is discussed in section 12.3.

the sample The sample used for this simulations is a multilayer of the composition

Si(179 Å) / Fe(12 Å) / Cu(462 Å) / Si-substrate

The ideal reflectivity was simulated using EDXR [34], where the SLD for magnetic Fe was chosen to be $14.096 \cdot 10^{-6}$ Å^{-2} for Fe$^{|+\rangle}$, and $2.096 \cdot 10^{-6}$ Å^{-2} for Fe$^{|-\rangle}$, respectively. No off-specular or incoherent scattering was assumed. The binning is $\Delta q = 4.4 \cdot 10^{-4}$ Å^{-1}. The substrate area is 5×5 mm^2.

The sample for this example was inspired by work of B. Wiedemann, TUM, who investigates the magnetic behaviour of thin iron films during growth. According in-situ measurements were performed at REFSANS, MLZ, and on Amor, PSI, using the *Selene* prototype [→12.3]. Feasibility studies for the latter were performed with a sample similar to the one used in these simulations, but with a larger area.[9] Figures 12.11 and 12.12 show the experimental raw-data, the reduced $I(\lambda, \theta)$-map and the resulting reflectivity curves.

[9] For the off-situ experiments the Fe-layer was prevented from oxidation by covering it with the Si-layer.

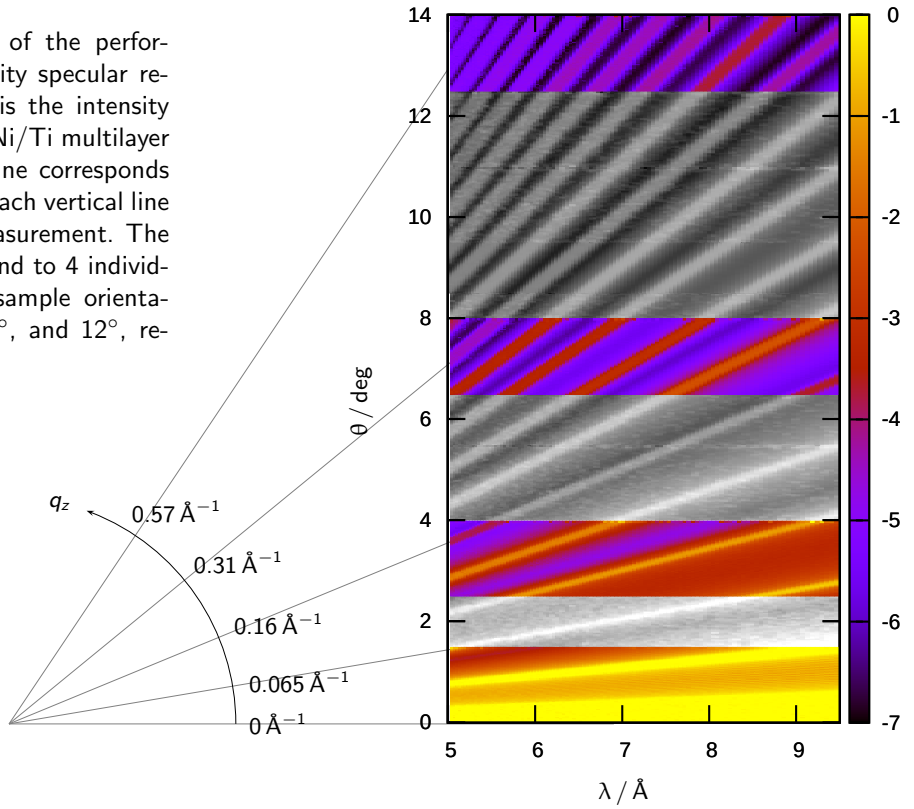

Figure 10.8: Illustration of the performance of the high-intensity specular reflectivity mode. Shown is the intensity map $\log_{10}[I(\lambda,\theta)]$ for a Ni/Ti multilayer on Si. Each horizontal line corresponds to a TOF measurement, each vertical line to an angle-dispersive measurement. The 4 coloured areas correspond to 4 individual measurements with sample orientations $\omega = -0,5°$, 2°, 6°, and 12°, respectively.

10.4.2 Data acquisition

To cover $q_z \in [0.01, 1]\,\text{Å}^{-1}$ there are 6 angular settings necessary (with a large overlap of 20%). The following table gives the sample tilt ω, and the corresponding θ-range and q_z-range.

ω / deg	θ_{min} / deg	θ_{max} / deg	$q_{z\,min}$ / Å^{-1}	$q_{z\,max}$ / Å^{-1}
−0.3	0.2	1.7	0.005	0.074
1.8	2.3	3.8	0.054	0.166
5.0	5.5	7.0	0.128	0.305
10.0	10.5	12.0	0.253	0.522
17.5	18.0	19.5	0.412	0.834
30.0	30.5	32.0	0.677	1.102

Table 10.3: Sample orientations ω and related θ- and q_z-ranges for the simulations. The time t is determined by the highest relative error of 14% after re-binning to 2.5%.

Figure 10.9 (a) shows the $I(\lambda,\theta)$-map for $\omega = -0.3°$. For normalisation here an ideal supermirror ($R(q_z) = 1 \forall q_z$) was assumed. The corresponding intensity map is shown in figure 10.9. It can be seen there that the highest intensity occurs at low λ and high θ. The first finding results from the choice of the λ-range [→2.3.1]. The second finding results from the increasing projected sample area for larger θ.

Figure 10.9 (e) shows the simulated $R(q_z)$ data points obtained by projection of $\mathbf{R}(\lambda,\theta)$ onto q_z.

The complete procedure was repeated for all ω settings mentioned in table 10.3, and the resulting individual reflectivity curves as well as the merged curve are shown in figure 10.10.

10.4.3 Discussion

counting time The gain of the high-intensity mode over the λ-θ-encoding mode in the present case is a factor 20 for the lowest ω and decreases for increasing ω. The reason is that in the encoding mode $\Delta\theta$ and thus the slit-opening are proportional to θ. At $\omega \approx 30°$ ($\theta \in [30, 5°, 32°]$) the aperture opening corresponds to half the full divergence. The time-gain there is only about a factor 2.

The average reduction in counting time for a moderate q_z-range (up to $\approx 0.5\,\text{Å}^{-1}$) is one order of magnitude.

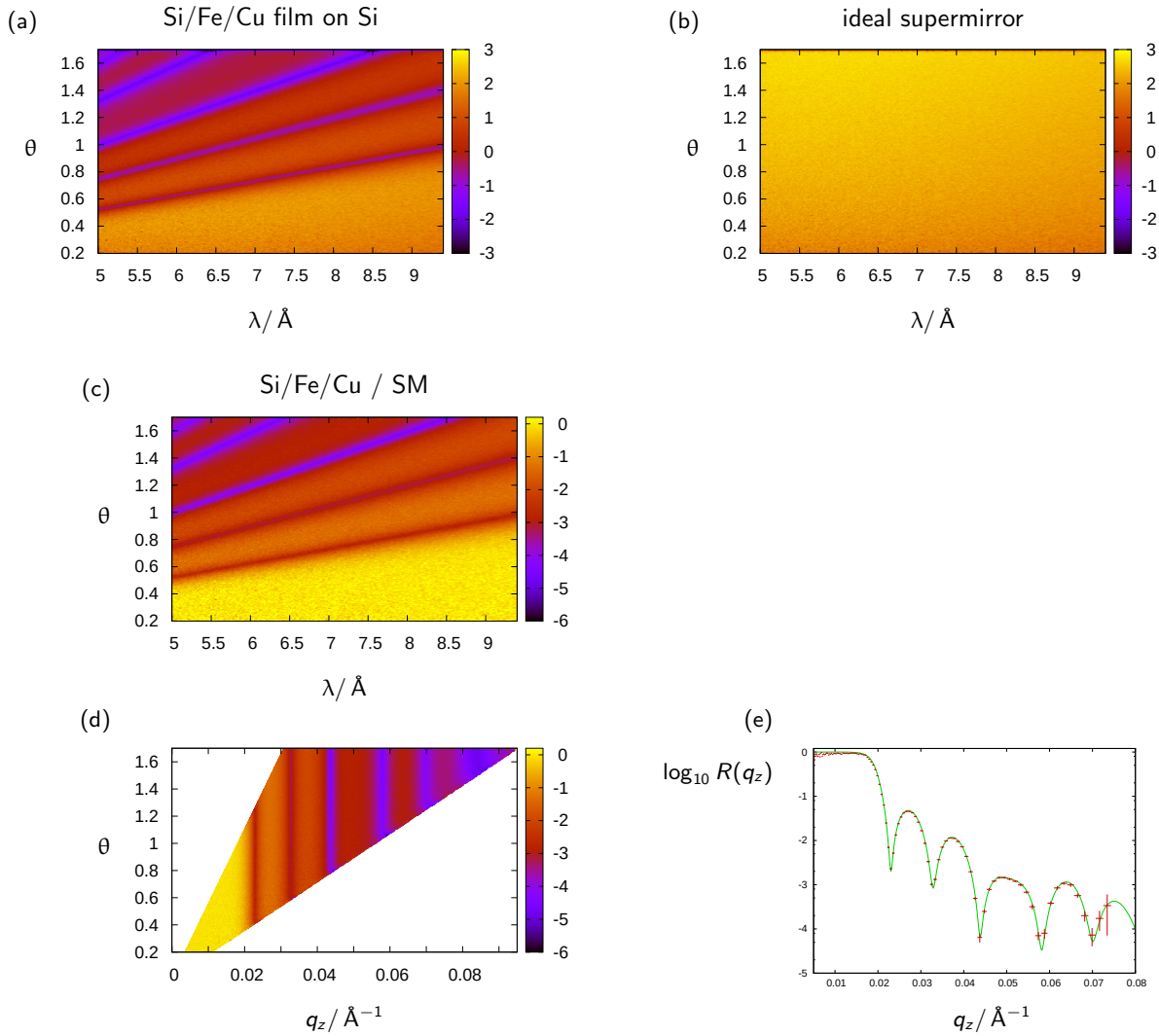

Figure 10.9: Simulated intensity-maps $I(\lambda, \theta)$ for a sample with the composition (a) Si (179 Å) / Fe (12 Å) /Cu (462 Å) / Si and a size of $5 \times 5\,\mathrm{mm}^2$, and for a perfect supermirror with the sample shape (b), respectively. Map (c) is obtained by pixel-wise division of maps (a) and (b). For map (d) λ was converted to q_z. Integration along θ and re-binning to $\Delta q/q = 2.5\%$ lead to the red marks in diagram (e). The green line is obtained by convolving the initial $R(q_z)$ used for the simulations with $\Delta q/q = 2.5\%$.

For larger samples, relaxed resolution (binning) requirements, or lower counting statistics it is possible to reach the split-second time-scale for time-resolved measurements. The q_z-range one can cover in one shot e.g. spans from 0.01 Å^{-1} to 0.085 Å^{-1}.

resolution Even though the resolution function is quite complex, the final $R(q_z)$ curve follows the simulated curve convoluted with 2.5% resolution up to high q_z. So even without a data treatment as suggested in section 10.5.3 a reasonable result is achievable in the high-intensity mode. This is in agreement with the experimental findings obtained with the *Selene* prototype.

dynamic range The dynamic range of 8 orders of magnitude obtained in the simulations is not realistic. The simulations ignored all background from the sample itself, from the sample environment, and from the detector. And the sample was assumed to show no off-specular or diffuse scattering.

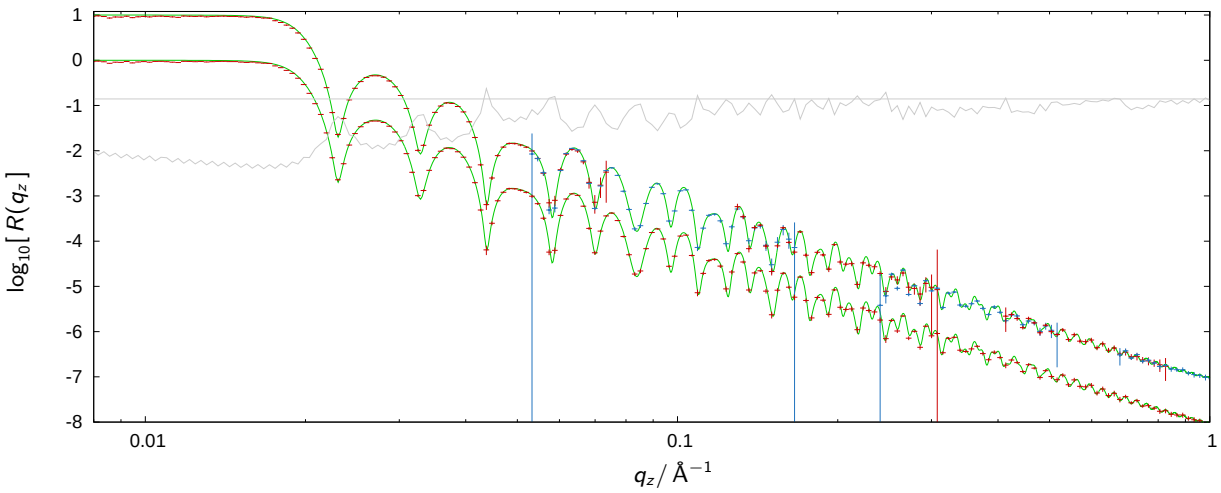

Figure 10.10: Specular reflectivity $R(q_z)$ of the multilayer Si (179 Å) / Fe (12 Å) /Cu (462 Å) / Si. The green curves correspond to the ideal reflectivity, convoluted with $\Delta q/q = 2.5\%$, the upper red and blue data points were obtained by simulations in the high-intensity specular mode for various sample orientations ω [→10.4.2]. These are scaled by 10 for clarity. The lower red data points were obtained by merging the individual *measurements*. The binning has a width of $\Delta q/q = 2.5\%$. The gray curve gives the relative error of the merged $R(q_z)$, the straight gray line is at 0.14.

10.5 Aspects on the data reduction

10.5.1 Raw-data and intensity-maps

Each neutron detected on the position sensitive detector has the associated parameters t, y and z for the time-of-flight and the position on the detector. The detector spatial resolution gives the constant values Δy and Δz, the pulse length sets an upper limit for $\Delta t <= \tau$. The latter one might be reduced by choppers.

From these basic parameters and the instrument parameters X (source detector distance) and θ_{detector} one can calculate the neutron wavelength [→8.3.1]

$$\lambda = \frac{h}{m_n}\frac{t}{X} \tag{10.5.1}$$

and the final angle after reflection

$$\theta_f = \epsilon + \omega - \arctan z \tag{10.5.2}$$

where ω is the inclination of the sample surface relative to the long axis of the last ellipse of the *Selene* guide, z is the position on the detector if that one is located at $\theta_{\text{detector}} = \epsilon + 2\omega$.

Discretisation in λ and θ_f of a large ensemble of events gives the intensity-map $I(\lambda, \theta_f)$ with the error-map $E(\lambda, \theta_f) \approx \sqrt{I(\lambda, \theta_f)}$. The approximation is valid for more than 10 counts per bin. For less counts a correcting factor has to be taken into account. Zero counts is also a measured quantity and has to have an error. This topic has to be investigated further!

It is also possible to extract $I(q_z)$, $E(q_z)$ or $I(q_z, q_x)$, $E(q_z, q_x)$, instead.

10.5.2 Normalisation

The measured intensity-map $I(\lambda, \theta)$ is not only a function of $R(q_z)$ of the sample, but also of the intensity $I_{\text{sample in}}(\lambda, \theta, x, y)$ incident on it. This quantity could ideally be measured with a reference sample with $R(q) = 1$ and exactly the same shape and position as the sample. Non-perfect reflectivity can be corrected for as long as $R_{\text{reference}}(q)$ is known and homogeneous. One could e.g. use a supermirror-coated reference with $m = 10$ (and low reflectivity) to correct up to $q_z = 0.22\,\text{Å}^{-1}$.

For higher q_z this approach is unrealistic. On the other side the projected sample height is larger, which leads to an averaging over beam inhomogeneities. So it might be possible to use a calculated or simulated reference. The quality of the calculation or simulation can be checked by comparison to the reference below $q_z = 0.22\,\text{Å}^{-1}$.

integration normal to the scattering plane The normalisation can be performed after integrating in y direction on the detector, i.e. normal to the scattering plane. This is justified by

$$\begin{aligned} I(t,y,z) &= I(t,z)\cdot g(y) \\ \frac{\int I(t,y,z)\,\mathrm{d}y}{\int I_0(t,y,z)\,\mathrm{d}y} &= \frac{\int I(t,z)\,g(y)\,\mathrm{d}y}{\int I_0(t,z)\,g(y)\,\mathrm{d}y} \\ &= \frac{I(t,z)\int g(y)\,\mathrm{d}y}{I_0(t,z)\int g(y)\,\mathrm{d}y} \\ &= R(t,z) \end{aligned}$$

where $g(y)$ gives the intensity distribution in y direction. By using a single detector or a 1D position sensitive detector this integration is already realised. This is the case in many conventional reflectometers.

10.5.3 Resolution

In most cases the resolution function $f(q_z)$ with $R_e(q_z) = R(q_z) * f(q_z)$ will neither be constant nor proportional to q_z. It is thus dangerous to add several data sets, e.g. data obtained with various ω.

summation of data sets with different resolution The summation of data sets $R_i(q_z)$ with weight a_i and individual resolution function $f_i(q_z)$ is possible, but it leads to a complicated (i.e. not single-Gaussian) resolution function f_Σ:

$$\begin{aligned} R_\Sigma &= \sum_i a_i R_i \quad , \quad \sum_i a_i = 1 \\ &= \sum_i a_i R * f_i \\ \mathcal{F}[R_\Sigma] &= \mathcal{F}\left[\sum_i a_i R * f_i\right] \\ &= \sum_i a_i \mathcal{F}[R * f_i] \\ &= \sum_i a_i \mathcal{F}[R]\cdot\mathcal{F}[f_i] \\ &= \mathcal{F}[R]\cdot\mathcal{F}\left[\sum_i a_i f_i\right] \\ &= \mathcal{F}\left[R * \left(\sum_i a_i f_i\right)\right] \\ R_\Sigma &= R * \left(\sum_i a_i f_i\right) \\ &:= R * f_\Sigma \end{aligned}$$

Simulation or fitting of $R(q_z)$ is possible when $f_\Sigma(q_z)$ can be estimated, and when it is taken into account in the simulation software.

Such a reflectivity profile might not be suited for publication because the abrupt changes in $f_\Sigma(q_z)$ at the joints can lead to significant features in R_Σ.

convolution to $\Delta q/q = \text{const}$ In cases when the experimental resolution function $f_e(q)$ of one data set $R_e(q) = R(q) * f_e(q)$ is known, one can convolve $R_e(q)$ with a resolution $f_c(q)$ in a way to get $R_p(q)$ with $\sigma_p \propto q$, i.e. $\Delta q/q = \text{const} := p$. For Gaussian functions

$$f_{e/c}(q) = \frac{1}{\sqrt{2\pi}\,\sigma_{e/c}}\,\exp\left[-\frac{(q-q_{e/c})^2}{2\sigma_{e/c}^2}\right] \tag{10.5.3}$$

the relation

$$\begin{aligned} f_p(q) &= f_e(q) * f_c(q) \\ &= \frac{1}{\sqrt{2\pi}\,\sigma_p} \exp\left[-\frac{(q-q_p)^2}{2\sigma_p^2}\right] \qquad \text{with} \quad \sigma_p^2 = \sigma_e^2 + \sigma_c^2, \quad q_p = q_e + q_c \end{aligned} \tag{10.5.4}$$

holds. σ_p is related to the full-width-at-half-maximum Δq via

$$\exp\left[-\frac{(\Delta q/2)^2}{2\sigma_p^2}\right] = 0.5 \tag{10.5.5}$$

$$\begin{aligned} \Delta q &= \sqrt{8\ln 2}\,\sigma_p \qquad (10.5.6) \\ &\approx 2.3548\,\sigma_p \\ \sigma_p &= (8\ln 2)^{-1/2}\,\Delta q \\ &= (8\ln 2)^{-1/2}\,p\,q \qquad (10.5.7) \end{aligned}$$

and thus

$$\sigma_c(q) = \sqrt{\sigma_p^2(q) - \sigma_e^2(q)} \tag{10.5.8}$$

$$= \sqrt{\frac{p\,q}{8\ln 2} - \sigma_e^2(q)} \tag{10.5.9}$$

So when $\sigma_e(q)$ is known one can get the *correcting Gaussian*.

Avoiding $\sigma_c <= 0$ leads to the constraint

$$p > \sqrt{8\ln 2}\,\frac{\sigma_e(q)}{q} \quad \forall q$$

The resulting *corrected* reflectivity curve is then

$$\begin{aligned} R_p(q) &= R_e(q) * f_c(q) \\ &= \int_{\bar{q}=q_{\min}}^{q_{\max}} R_e(q-\bar{q}) \cdot \frac{1}{\sqrt{2\pi}\,\sigma_c(\bar{q})} \exp\left[-\frac{\bar{q}^2}{2\sigma_c(\bar{q})^2}\right] \mathrm{d}\bar{q} \end{aligned} \tag{10.5.10}$$

Thisnow allows to merge several data sets after bringing them to the same resolution for each q in the overlapping region. Information is of course lost by lowering the resolution, but the resulting $R_p(q)$ and eventually a merged $R_\Sigma(q)$ have the appearance expected by standard software, most of the users, and almost all readers of publications.

11 McStas Simulations on Reference Sample

Most part of the design and optimisation of the *Selene* guide and of the full instrument *Estia* is based on analytic calculations [→6]. Only for the fine-tuning and to explore the influence of non-perfect guides and eventual mis-alignments the Monte Carlo simulations were performed. Here exclusively McSats [26, 27] was used.

To allow for a comparison among the various instrument concepts for the ESS and with existing instruments, the proposers and the STAP agreed on one standard sample and a set of parameters for data reduction and presentation. In detail these are:

common standard sample The sample is a silicon waver with an oxide layer, to be measured against air:

material	thickness	area
air		
SiO_2	15 Å	
Si-substrate		$10 \times 10\,\mathrm{mm}^2$

The synthetic $R(q_z)$ curve was supplied by H. Wacklin within $q_z \in [0, 001, 0.7]\,\text{Å}^{-1}$.

resolution All data of the following examples are re-binned to $\Delta q/q = c = \text{const}$, where the actual bin-width is 1%, here. This leads to a q_z-grid with bin n covering

$$q_{z\,n} \in \left[q_0 \cdot (1+c)^n\,,\; q_0 \cdot (1+c)^{n+1} \right[$$

The lower q_z limit for this binning (for positive n) is Œ defined here to be $q_0 = 0.001\,\text{Å}^{-1}$.

counting time The counting time per individual measurement (for one sample orientation ω) is chosen in a way that in specular reflectivity the (used) bin with the lowest signal contains 50 counts.[1] This corresponds to a relative error of $\sigma = 1/\sqrt{50} \approx 14\%$.

simplifications To reduce the computing time and the complexity of the instrument file a series of simplifications were made relative to the *real* instrument. The most prominent are:

- gravity is ignored: this leads to a decrease in measurement time for long wavelengths of a few percent;
- no aluminium windows (better the attenuation due to these) were taken into account;
- the complete flight path was assumed to be evacuated;
- the moderator was assumed to be homogeneous, without *hot area* close to the target;
- the detector efficiency was set to 100%.

background No real background is simulated, i.e. the McStas sample is a mirror which either reflects specularly or absorbs. No diffuse or off-specular scattering is simulated. To still get a realistic counting time for a high dynamic range, an artificial background is added to the simulated intensity before data reduction, and subtracted after normalisation. The dynamic range of the measurement is not affected this way, but the error (and thus the measuring time) increases below a certain reflectivity threshold. Here a background of 10^{-7} of the ideally reflected beam ($R = 1$) is assumed.

[1] This definition is problematic because it punishes measurement schemes covering a wide q_z-range simultaneously. It might be favourable to measure at more angles of incidence with a wider overlap to shorten the measurement time - sacrificing the design criterion to cover a wide q-range with one angle (e.g. for time-resolved studies or for liquid surfaces). This could partially be compensated by adding some time for sample and detector movement.

normalisation For all measurements a reference measurement was performed with a sample of the same shape and orientation, but with a perfect reflectivity $R(q_z) = 1 \forall q_z$. It was assumed that the error of the reference measurement can be neglected compared to the Si/SiO_2 sample.

data processing Each McStas simulation leads to one data string $\mathbf{i}(t, y, z)$ where each entry corresponds to one ray reaching the detector.[2] The raw data are the time t of arrival, the coordinates on the detector y and z, and the simulated probability that a neutron arrives within one second. These data are binned with $\Delta t/t = 0.5\%$, $\Delta y = 0.5\,\text{mm}$ (scattering plane), $\Delta z = \infty$ (integration over sample plane) to give the intensity matrix $\mathbf{I}(t, y)$. For each sample orientation ω two simulations are performed, one with the Si/SiO_2 sample, and one with a perfectly reflecting sample for reference. This leads to the matrices

$$\begin{aligned} \mathbf{I}^{\text{s}}(t,y) &: I^{\text{s}}_{t,y} \quad \text{Si/SiO}_2 \text{ sample} \\ \mathbf{I}^{\text{r}}(t,y) &: I^{\text{r}}_{t,y} \quad \text{reference} \end{aligned}$$

The background is added to the sample simulation.

$$\mathbf{I}^{\text{s,bg}}(t,y) : I^{\text{s,bg}}_{t,y} = I^{\text{s}}_{t,y} + 10^{-7} I^{\text{r}}_{t,y}$$

The intensity is multiplied by the counting time t^{s} to give counts per detector and time channel. Here this matrix is called a *measurement*.

$$\begin{aligned} \mathbf{C}^{\text{s,bg}}(t,y) &: C^{\text{s,bg}}_{t,y} = I^{\text{s,bg}}_{t,y}\, t^{\text{s}} \\ \Delta\mathbf{C}^{\text{s,bg}}(t,y) &: \Delta C^{\text{s,bg}}_{t,y} = \sqrt{C^{\text{s,bg}}_{t,y}} \\ \mathbf{C}^{\text{r}}(t,y) &: C^{\text{r}}_{t,y} = I^{\text{r}}_{t,y}\, t^{\text{r}} \end{aligned}$$

The data are normalised element-wise (neglecting the error of the reference) to give the reflectivity matrix $\mathbf{R}$:

$$\begin{aligned} \mathbf{R}^{\text{s,bg}}(t,y) &: R^{\text{s,bg}}_{t,y} = \frac{t^{\text{r}}}{t^{\text{s}}} \frac{C^{\text{s,bg}}_{t,y}}{C^{\text{r}}_{t,y}} = \frac{I^{\text{s,bg}}_{t,y}}{I^{\text{r}}_{t,y}} \\ \Delta\mathbf{R}^{\text{s,bg}}(t,y) &: \Delta R^{\text{s,bg}}_{t,y} = \frac{t^{\text{r}}}{t^{\text{s}}} \frac{\Delta C^{\text{s,bg}}_{t,y}}{C^{\text{r}}_{t,y}} = \sqrt{\frac{1\,\text{s}}{t^{\text{s}}}} \frac{\sqrt{I^{\text{s,bg}}_{t,y}}}{I^{\text{r}}_{t,y}} \end{aligned}$$

This procedure requires a non-zero (or better statistically robust) matrix element $I^{\text{r}}_{t,y} \forall t, y$, which leads to quite long computing times for the reference.[3] To account for the different counting times for sample and reference a scaling factor $t^{\text{r}}/t^{\text{s}}$ is used which cancels the effect of the counting time on the reflectivity, but not on its error. In a next step the coordinates t and y are transformed to

$$\begin{aligned} \lambda &= t \frac{h}{m\,\overline{\text{MD}}} \\ \Delta\lambda &= \tau \frac{h}{m\,\overline{\text{MD}}} \\ \theta &= \epsilon + \omega - \arctan \frac{y}{\overline{\text{SD}}} \\ \Delta\theta &= \arctan \frac{\Delta y}{\overline{\text{SD}}} \end{aligned}$$

with the neutron mass m, the moderator-to-detector distance $\overline{\text{MD}} = 58\,400\,\text{mm}$, and the sample-to-detector distance $\overline{\text{SD}} = 6\,200\,\text{mm}$. The detector centre is at $y = 0\,\text{mm}$. This gives

$$\begin{aligned} \mathbf{R}^{\text{s,bg}}(\lambda,\theta) &: R^{\text{s,bg}}_{\lambda,\theta} \\ \Delta\mathbf{R}^{\text{s,bg}}(\lambda,\theta) &: \Delta R^{\text{s,bg}}_{\lambda,\theta} \end{aligned}$$

[2] This is different compared to a real world experiement, where either a neutron arrives, or not. Thus the formalism presented here varies from the one in section 10.1.3.

[3] This computing time is not to be confused with the measurement time. A longer computing time leads to a lower error in the simulated probability that a neutron arrives within a defined parameter space.

Each matrix element is associated to a normal momentum transfer

$$\begin{aligned} q_{z\,\lambda,\theta} &= \frac{4\pi \sin\theta}{\lambda} \\ \Delta q_{z\,\lambda,\theta} &= \frac{4\pi \sqrt{\cos^2\theta\,\Delta\theta^2 + \sin^2\theta\,\Delta\lambda^2/\lambda^2}}{\lambda} \end{aligned}$$

In the next step the matrix elements of $\mathbf{R}^{\mathrm{s,bg}}(\lambda,\theta)$ are sorted into a q_z grid with $q_{z\,n} = (1+c)^n$, here a binning with $c = \Delta q_z/q_z = 1\%$.

$$\begin{aligned} \mathbf{R}^{\mathrm{s,bg}}(q_z) \;:\; R^{\mathrm{s,bg}}_{q_z\,n} &= \sum\nolimits_{\lambda,\theta:\, q_{z\,n} \le q_{z\,\lambda,\theta} < q_{z\,n+1}} p_{\lambda,\theta}\, R^{\mathrm{s,bg}}_{\lambda,\theta}\, M_{\lambda,\theta} \\ \Delta\mathbf{R}^{\mathrm{s,bg}}(q_z) \;:\; \Delta R^{\mathrm{s,bg}}_{q_z\,n} &= \sqrt{\sum\nolimits_{\lambda,\theta:\, q_{z\,n} \le q_{z\,\lambda,\theta} < q_{z\,n+1}} \left(p_{\lambda,\theta}\,\Delta R^{\mathrm{s,bg}}_{\lambda,\theta}\right)^2 M_{\lambda,\theta}} \end{aligned}$$

with the weights

$$p_{\lambda,\theta} = \frac{\frac{1}{\Delta R^{\mathrm{s,bg}}_{\lambda,\theta}}}{\sum_{\lambda,\theta:\ldots} \frac{1}{\Delta R^{\mathrm{s,bg}}_{\lambda,\theta}}}$$

and the mask

$$\mathbf{M}(\lambda,\theta) \;:\; M_{\lambda,\theta} = \begin{cases} 1 & \text{for} \quad \theta(\lambda) - \Delta\theta(\lambda)/2 \le \theta \le \theta(\lambda) + \Delta\theta(\lambda)/2 \\ 0 & \text{else} \end{cases}$$

The mask $\mathbf{M}(\lambda,\theta)$ guarantees that the summation is performed only over a defined range in the θ-λ-space where specular reflectivity is expected. $\theta(\lambda)$ is the nominal angle of incidence of the beam as a function of λ. For the conventional mode it is constant, and for the λ-θ encoding mode it is exactly the encoding relation. And finally for the high-intensity mode $\theta(\lambda) = \omega + \epsilon$ and $\Delta\theta(\lambda) = 1.5°$.

Thee errors in q_z, i.e. the resolution is treated like the errors $\Delta\mathbf{R}q_z$:

$$\Delta\mathbf{q_z}(q_z) \;:\; \Delta q_{z\,n} = \sum\nolimits_{\lambda,\theta:\, q_{z\,n} \le q_{z\,\lambda,\theta} < q_{z\,n+1}} p_{\lambda,\theta}\,\Delta q_{z\,\lambda,\theta}$$

The resolution $\Delta\mathbf{q_z}(q_z)$ obtained this way is only an approximation and should be handled with care. The dominating contribution is the finite pulse length leading to a resolution of at most 4%.

Finally the known background of 10^{-7} is subtracted from the reflectivity curve (the error to the normalisation is marginal):

$$\mathbf{R}^{\mathrm{s}}(q_z) \;:\; R^{\mathrm{s}}_{q_z\,n} = R^{\mathrm{s,bg}}_{q_z\,n} - 10^{-7}$$

The full $R(q_z)$ curve is obtained by merging the individual $\mathbf{R}^{\mathrm{s}}(q_z)$ and $\Delta\mathbf{q_z}(q_z)$ vectors. In the following for each principle operation mode the $\mathbf{R}^{\mathrm{s}}(q_z)$ for all ω, the merged data set, and the errors $\Delta\mathbf{R}(q_z)$ (statistical accuracy) and $\Delta\mathbf{q_z}(q_z)$ (resolution) are presented.

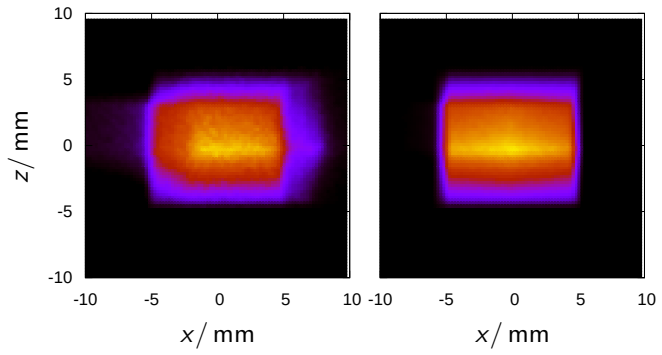

Figure 11.1: Footprint of the neutron beam on the sample plane for $\omega = -0.3°$ (left) and for $\omega = 5.6°$ (right), simulated in the high-intensity specular reflectometry mode. The intensity is encoded in the colour with black = zero and yellow = maximum. x points along the neutron flight path, z is vertical. The virtual source was set to the sample size of $10 \times 10\,\mathrm{mm}^2$.

footprint One requirement for the comparison was that the sample should not be overilluminated. This is realised by the size and orientation of the virtual source. Figure 11.1 shows the footprint in the sample plane for several sample orientations. For small angles a tiny fraction of the total intensity (below 0.1%) misses the sample surface, for larger ω it is even less. The reduction of the intensity in z-direction away from the centre displays the reduced brilliance transfer of the guide system.

λ-θ-diagram Figure 11.2 shows the volumes of the λ-θ-space $\mathbf{R}^{\omega}(\lambda, \theta)$ specularly *illuminated* in the three operation modes for $\omega = -0.3°$. The aperture was chosen to give $\Delta\theta/\theta = 4\%$, which explains why the λ-θ-encoding streak gets narrower at high λ.

The volumes covered in the conventional mode and in the λ-θ-encoding mode are similar, but since in the latter case the intensity is distributed over a wider q_z-range, the measurements take longer to reach the same statistics within one q_z-bin of the same width.

For this extreme case (low q_z) the difference in the volumes between conventional or λ-θ-encoding on one side and the high-intensity mode on the other side is more than a factor 30. This factor reduces for higher angles of incidence because the maximum divergence of 1.5° is fix for the high-intensity mode, while it increases with θ for the other two modes.

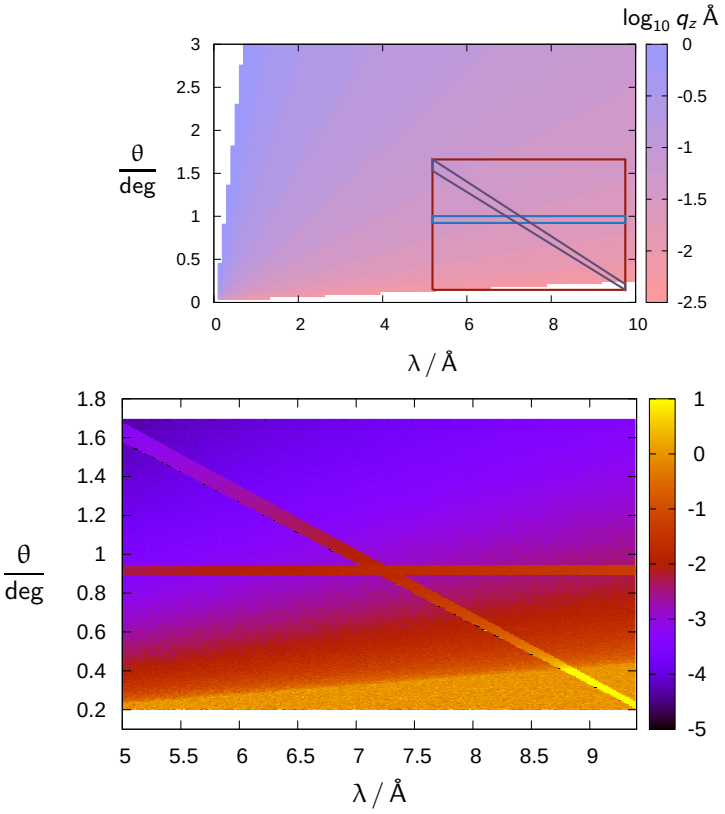

Figure 11.2: (bottom) $\log_{10}$ Intensity maps of the matrices $\mathbf{R}^{\omega}(\lambda, \theta)$ for $\omega = -0.3°$ for the high-intensity mode (large rectangular coloured area), almost conventional mode (narrow horizontal streak), and λ-θ-encoding mode (diagonal streak). The latter two have an intensity off-set of 1. The triangle at low θ opening with increasing λ corresponds to the total reflection plateau, i.e. $\log_{10} R = 0$. The upper graph shows the contours of the three $\mathbf{R}^{\omega}(\lambda, \theta)$ volumes projected on a $q_z(\lambda, \theta)$ map to illustrate the q_z-range covered with the various modes.

11.1 Almost conventional mode

An aperture behind the *Selene* guide limits $\Delta\theta$ with $\Delta\theta/\theta = 4\%$. The beam has at most the footprint shown in figure 11.1.

ω / deg	θ_{min} / deg	θ_{max} / deg	$q_{z\,min}$ / Å^{-1}	$q_{z\,max}$ / Å^{-1}	t / s
−1.05	0.20	0.21	0.0047	0.0088	2
−0.89	0.36	0.37	0.0085	0.016	6
−0.60	0.65	0.68	0.015	0.029	20
−0.08	1.17	1.22	0.027	0.052	50
0.85	2.1	2.2	0.050	0.093	100
2.55	3.8	4.0	0.09	0.17	200
5.65	6.9	7.2	0.16	0.30	1 200
11.05	12.3	12.8	0.29	0.54	15 000
20.85	22.1	23.0	0.52	0.97	
			0.005	0.35	16 578

Table 11.1: Sample orientations ω and related θ and q_z-ranges. The counting time t was obtained by keeping the relative error below $1/\sqrt{50}$.
The required q_z-range is covered with 8 sample orientations ω, with an overlap of 4.5%. The first 4 settings could be realised with $\omega = -0.5$ and moving the aperture in between the measurements.
Smaller overlap and an increased lower q_z limit would allow to cover the range up to 0.35 Å^{-1} with 7 settings.

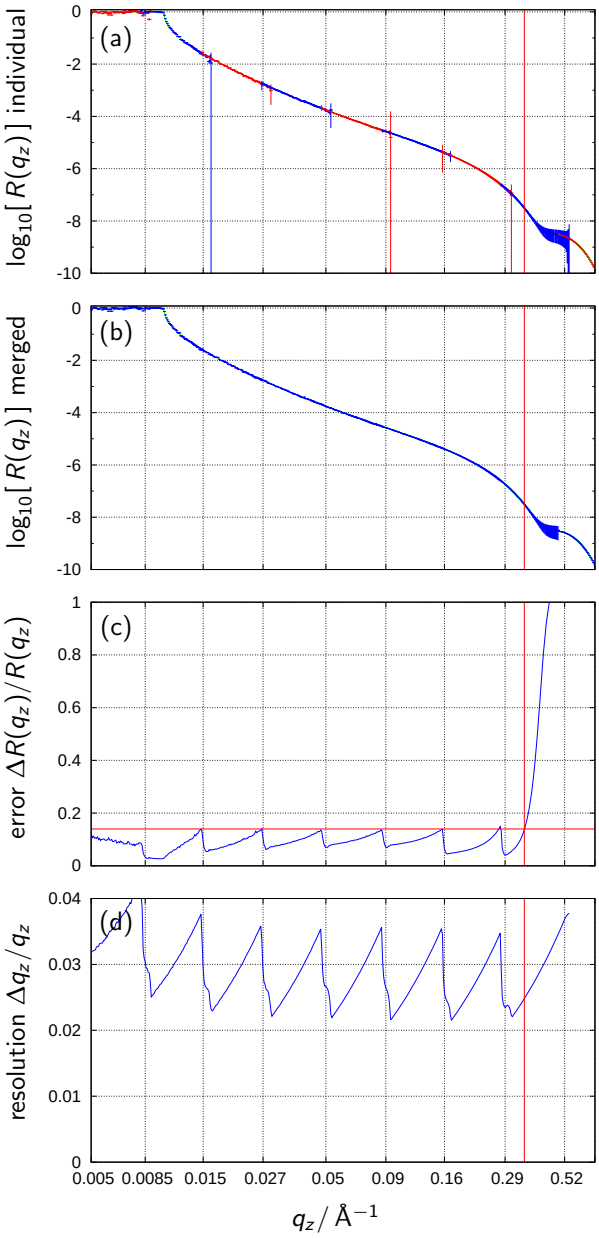

Figure 11.3: Simulated reflectivity of a Si/SiO_2 surface in the almost conventional reflectivity mode. (The low statistics for the smallest ω are due the limited computing time available.)

(a) Individual measurements for $\omega = -1.05°$, $-0.89°$, $-0.60°$, $-0.08°$, $0.85°$, $2.55°$, $5.65°$, $11.05°$, and $20.85°$ in alternating colours red and blue. Details are given in table 11.1

(b) The merged $R(q_z)$ obtained from these on a $\Delta q/q = 1\%$ grid.

(c) The relative error $\Delta R(q_z)/R(q_z)$ for the merged curve for the counting times given in table 11.1. The red line is the required error threshold of $1/\sqrt{50}$. The increase of the error towards the upper interval boundaries is caused by the strong decrease of the reflectivity is cot completely compensated for by the increase of flux for $1/\lambda$.

(d) The corresponding resolution $\Delta q_z/q_z$ as obtained with the approximation mentioned above. The saw-like shape originates from the resolution varying from 4% to 2% with λ, where the overlap in g_z leads to a reduced variation. For smallest q_z the spatial detector resolution has a sizeable influence.

11.2 λ-θ encoding mode

The aperture behind the *Selene* guide is scanned across the beam during each pulse. Its opening is chosen to give $\Delta\theta/\theta = 4\%$.

ω / deg	θ_{min} / deg	θ_{max} / deg	$q_{z\,min}$ / Å^{-1}	$q_{z\,max}$ / Å^{-1}	t / s
−0.3	0.2	1.7	0.0047	0.075	100
2.1	2.6	4.1	0.060	0.18	200
5.6	6.1	7.6	0.14	0.33	1 000
11.0	11.5	13.0	0.27	0.57	25 000
19.3	19.8	21.3	0.45	0.91	
			0.005	0.35	26 300

Table 11.2: Sample orientations ω and related θ and q_z-ranges. The counting time t was obtained by keeping the relative error below $1/\sqrt{50}$.
The required q_z-range is covered with 4 sample orientations ω, with an overlap of 20%.

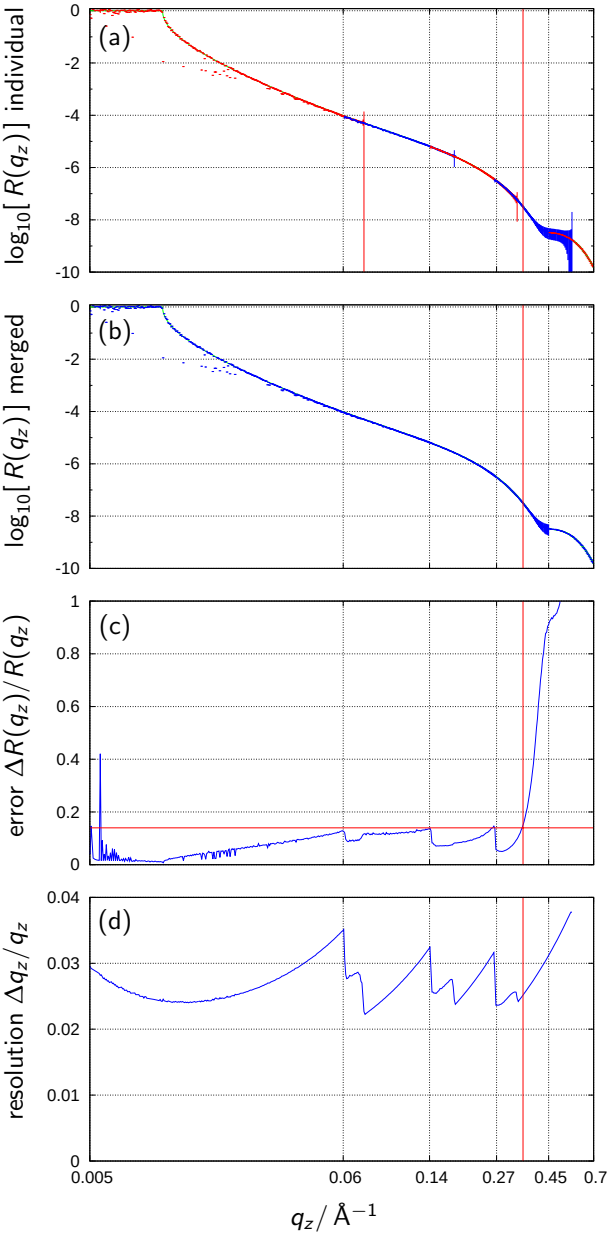

Figure 11.4: Simulated reflectivity of a Si/SiO_2 surface in the λ-θ-encoding reflectivity mode. (The low statistics for the smallest ω are due the limited computing time available.)

(a) Individual measurements for $\omega = -0.3°$, 2.1°, 5.6°, 11.0°, 19.3° in alternating colours red and blue. Details are given in table 11.2

(b) The merged $R(q_z)$ obtained from these on a $\Delta q/q = 1\%$ grid.

(c) The relative error $\Delta R(q_z)/R(q_z)$ for the merged curve for the counting times given in table 11.2. The red line is the required error threshold of $1/\sqrt{50}$. The increase of the error towards the upper interval boundaries is caused by the strong decrease of the reflectivity is cot completely compensated for by the increase of flux for $1/\lambda$.

(d) The corresponding resolution $\Delta q_z/q_z$ as obtained with the approximation mentioned above. The saw-like shape originates from the resolution varying from 4% to 2% with λ, where the summation and the overlap in q_z lead to averaging.

11.3 High-intensity specular reflectivity mode

The divergence-defining aperture behind the guide is fully open, which means that the beam has the full divergence of 1.5° at all times.

ω / deg	θ_{min} / deg	θ_{max} / deg	$q_{z\,min}$ / Å^{-1}	$q_{z\,max}$ / Å^{-1}	t / s
−0.3	0.2	1.7	0.0047	0.075	10
2.1	2.6	4.1	0.060	0.18	27
5.6	6.1	7.6	0.14	0.33	200
11.0	11.5	13.0	0.27	0.57	6 500
19.3	19.8	21.3	0.45	0.91	
			0.005	0.35	6 737

Table 11.3: Sample orientations ω and related θ and q_z-ranges. The counting time t was obtained by keeping the relative error below $1/\sqrt{50}$.
The required q_z-range is covered with 4 sample orientations ω, with an overlap of 20%. The total counting time of almost 2 h is completely dominated by the last range with a reflectivity reaching below the artificial background of 10^{-7}.

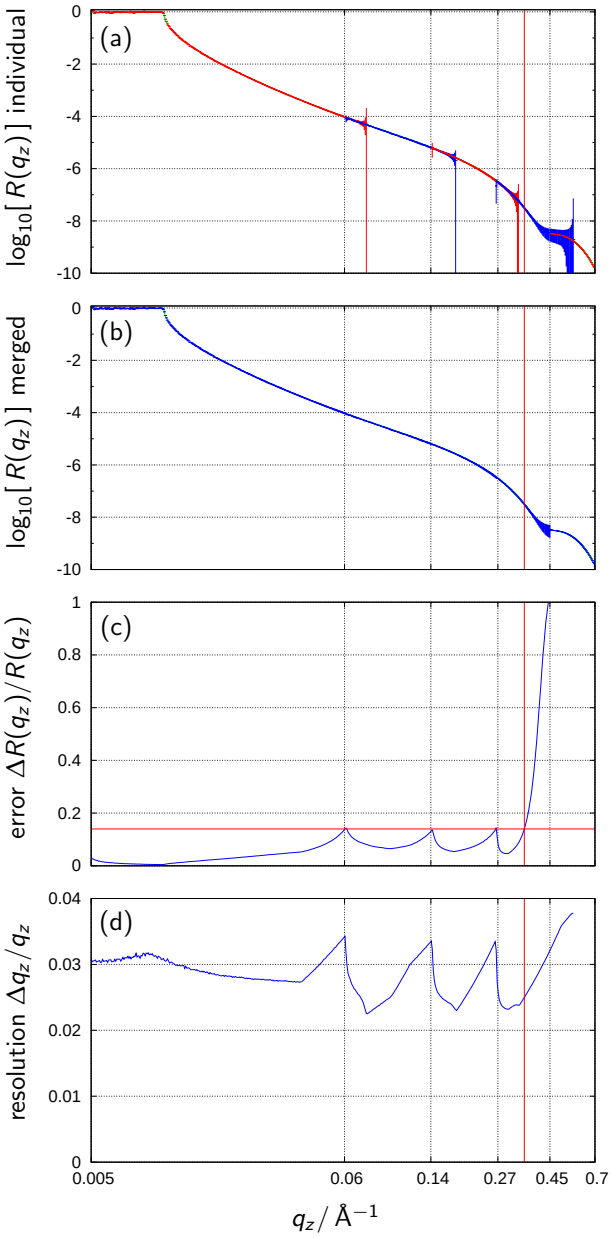

Figure 11.5: Simulated reflectivity of a Si/SiO_2 surface in the height-intensity specular reflectivity mode.

(a) Individual measurements for $\omega = -0.3°$, 2.1°, 5.6°, 11.0°, 19.3° in alternating colours red and blue. Details are given in table 11.3

(b) The merged $R(q_z)$ obtained from these on a $\Delta q/q = 1\%$ grid.

(c) The relative error $\Delta R(q_z)/R(q_z)$ for the merged curve for the counting times given in table 11.3. The red line is the required error threshold of $1/\sqrt{50}$. The increase of the error towards the interval boundaries is explained by the smaller area of the λ-θ diagram corresponding to these q_z values. [→fig. 11.2]

(d) The corresponding resolution $\Delta q_z/q_z$ as obtained with the approximation mentioned above. The saw-like shape originates from the resolution varying from 4% to 2% with λ, where the summation along g_z leads to averaging and thus to a reduced variation.

11.3.1 . . . with large q_z-overlap

The counting time in this mode is dominated by the borders of the q_z-range. A small overlap thus means a few sample settings, but a relatively long counting time. By increasing the overlap, here a doubling of the sample orientations, the actual counting time drops by an order of magnitude for $q_z < 0.4\,\text{Å}^{-1}$.

ω / deg	θ_{min} / deg	θ_{max} / deg	$q_{z\,min}$ / Å^{-1}	$q_{z\,max}$ / Å^{-1}	t / s
−0.3	0.2	1.7	0.0047	0.075	1
1.0	1.5	3.0	0.035	0.13	3
2.1	2.6	4.1	0.060	0.18	4
3.5	4.0	5.5	0.092	0.24	12
5.6	6.1	7.6	0.14	0.33	35
8.1	8.6	10.1	0.20	0.44	150
11.0	11.5	13.0	0.27	0.57	4000
19.3	19.8	21.3	0.45	0.91	
			0.005	0.35	4205

Table 11.4: Sample orientations ω and related θ and q_z-ranges. The counting time t was obtained by keeping the relative error below $1/\sqrt{50}$.
The required q_z-range is covered with 7 sample orientations ω, with an overlap of $> 50\%$. The total counting time of some 1.2 h is completely dominated by the last range with a reflectivity reaching below the artificial background of 10^{-7}.

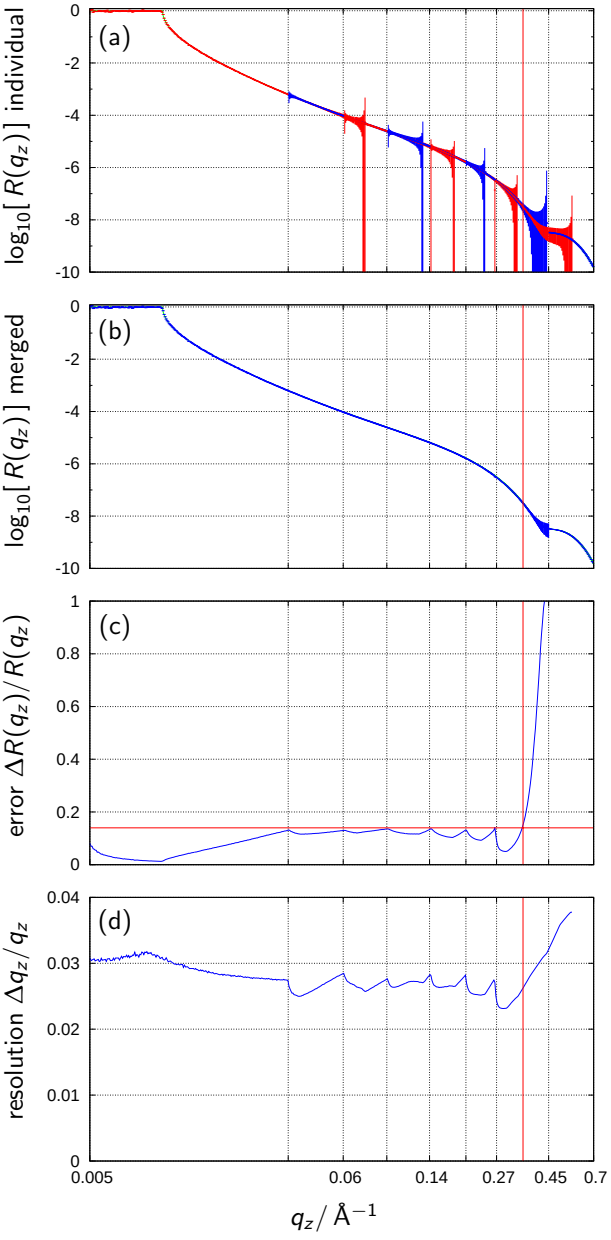

Figure 11.6: Simulated reflectivity of a Si/SiO_2 surface in the height-intensity specular reflectivity mode.

(a) Individual measurements for $\omega = -0.3°$, 1.0°, 2.1°, 3.5°, 5.6°, 8.1°, 11.0°, 19.3° in alternating colours red and blue. Details are given in table 11.3

(b) The merged $R(q_z)$ obtained from these on a $\Delta q/q = 1\%$ grid.

(c) The relative error $\Delta R(q_z)/R(q_z)$ for the merged curve for the counting times given in table 11.3. The red line is the required error threshold of $1/\sqrt{50}$.

(d) The corresponding resolution $\Delta q_z/q_z$ as obtained with the approximation mentioned above. Due to the larger overlap the resolution variation is damped and varies between 2.5% and 3.2%.

11.4 Discussion

The outcome of these simulations is not really surprising because most of the information obtained at the end was put in earlier, or could have been obtained analytically. The only new information is the time-scale needed for the measurements in case the simplifications made are not too severe.

The requested high statistical accuracy and high q_z-resolution can be obtained within several seconds for small q_z. For reflectivities below the artificial background level of 10^{-7} the counting time grows dramatically, so that the total counting time is completely dominated by that part.

almost conventional mode The required q_z-range can be measured with 8 sample settings, where switching between the first 4 only requires a repositioning of the aperture. This means 4 detector movements of 22° (2.4 m) in total have to be added to the pure measurement time of 4.6 h.

The aperture was chosen to give $\Delta\theta/\theta = 4\%$. This does not have an influence on the resolution of the measurement, which is given by $\Delta\lambda = 0.2\,\text{Å}$ and the detector resolution corresponding to 0.0046°. But it affects the off-specular resolution and the contamination of the specular signal with off-specular or diffuse scattering. Both were not included in these simulations. Opening the aperture leads to a linear decrease in counting time.

λ-θ-encoding The counting time in the λ-θ-encoding mode is expected to take slightly longer than in the conventional mode because the not ideally matched distribution of counting time and reflectivity. I.e. the point with the worst statistics determines the counting time, no matter how wide the q_z-range is. Using several ranges as in the conventional mode allows for relaxed counting times in the other regions. At the same time the intensity is *concentrated* more, leading to a reduced counting time also in the critical q_z-regions.

By just looking on the measurement time (7.3 h in total) the extension of the q_z-range obtained by scanning the aperture is counterproductive. But it reduces the sample settings to 4, where the last one covers a narrow window of interest only, the rest of its q_z-coverage is at higher q_z and thus lost for the statistics. For this last bit with the highest errors (due to the artificial background) one could reverse the scanning direction and this way compress the q_z-range covered within one angular setting. This way one could use all the pulse to concentrate on the region just below $q_z = 0.35\,\text{Å}^{-1}$, and thus the measurement time would drop even compared to the conventional mode.

high-intensity mode Due to the much higher accepted incident intensity, the measurement time is reduced by more than an order of magnitude compared to the λ-θ-encoding, using the same angular settings.

By using a larger overlap the number of angular settings increases, but the total counting time is reduced to 1.2 h, which is less than a third of the conventional time. Especially for $q_z < 0.3\,\text{Å}^{-1}$ the counting time drops to 4% of the one needed in the conventional mode.

realistic measurement times on Estia The parameters defined for the reference simulations allow to compare the various instruments, but they are not realistic in a sense that they would not be used in a real world measurement.

In most present day cases, the dynamic range is restricted to some 6 orders of magnitude by the time available. This corresponds roughly to a maximum $q_z = 0.3\,\text{Å}^{-1}$. With the intrinsic instrument resolution being about 4%, one would bin the data to 2%. For the Si/SiO_2 sample an even lower resolution would be fine. With the same statistics requirement ($\Delta R/R \leq 14\%$) the measurement would take about half an hour in the λ-θ-encoding mode, 2 min in the high-intensity mode with 3 angular settings, and less than 0.5 min with 5 settings (neglecting the detector movement).

For most inorganic samples, and for periodic organic multilayers much more structure of the reflectivity curve can be expected with locally much higher $R(q_z)$ (e.g. Bragg-peaks). The time needed to characterise these samples is even shorter and thus high q_z can be measured in a reasonable time, provided the (sample-intrinsic) background is sufficiently small.

12 Prototype

A down-scaled prototype of a *Selene* guide was build and tested at PSI. The main reasons for this were to check the concept in reality and to prove that it is possible to reach the necessary accuracy. The testing phase gave a lot of feed-back for improvements (essentially for the support system and the shielding) and triggered further innovations like the slit system for the virtual source and the polariser. In addition a full scheme for data reduction was established. Finally the device turned out to be a very useful add-on for the TOF neutron reflectometer Amor at PSI.

12.1 Design considerations

The prototype was designed to operate in a λ- and θ-range close to what can be expected for a reflectometer at the ESS, paying respect to the beam characteristics and spacial constraints at the instruments BOA and Amor (12.3.1) at the spallation source SINQ at PSI.

- length of the focusing section ($= 4c$): The available space at BOA is some 9 m. About 3 m are needed to get an acceptable angular resolution on the detector ($\Delta\theta \approx 0.04°$). Another 1.5 m before the first focal point are required for the ml-monochromator, the chopper and eventually further equipment. This led to $4c = 4$ m.
- divergence: The divergence was chosen to be slightly larger than what is available at BOA or Amor, i.e. $\Delta\theta = 1.8°$.
- ellipse parameters: The effective length was defined to $\xi = 0.60$, leading to $b/a = 0.021480$.
- λ-range: The λ-range was selected based on the considerations made in (2.3.1) to be $\lambda \in [3.8, 12]$ Å. This results in a coating with $m = 4$.
- sample size: For $c = 1$ m and the typical $b/a \approx 0.02$ the maximum spot size with only small influence of coma aberration is 1×1 mm^2. Larger spots are possible, but the footprint then is no longer homogeneous.
- chopper speed and pulse length: To cover the required λ-range in time-of-flight with a possible chopper-detector distance of some 8 m one needs a frequency of $\approx 60\,\mathrm{s}^{-1}$. The chopper opening-to closing time ratio is the same as for the ESS pulses, i.e. 0.04.

12.2 Devices

Most of the following devices were designed, constructed and fabricated at PSI. The exceptions are the X95 elements, the precision slit and the guide elements.

12.2.1 Pulse chopper

The reduced length of the set-up compared to the ESS dimensions with about the same λ-range leads to shorter repetition rate and pulse length for the test set-up. The pulse chopper will operate with up to 60 Hz, its open/closed time ratio is about 5% (to be determined exactly). The chopper disc has 2 openings.

The much reduced dimension of the beam relative to conventional set-ups leads to a disc diameter of $\varnothing =$ 160 mm. The absorbing material is 2.2 mm of an Al :^{10}B alloy, followed by 2 mm Cd. The absorbing region is 10 mm wide. Figure 12.1 shows on the left side the pulse chopper after assembling, before testing.

The pulse chopper is equipped with a laser-based trigger for the TOF data acquisition. Since this system detects each gap opening of the chopper, no correction for the second gap and eventually a phase error is needed.

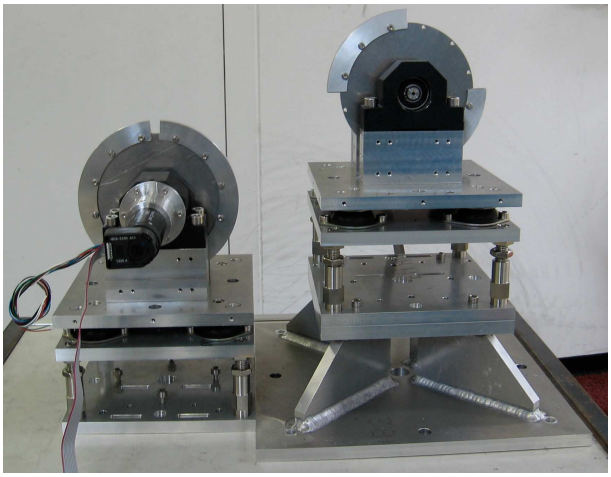

Figure 12.1: Pulse chopper (left) and frame overlap chopper (right) for the *Selene* prototype.

12.2.2 Frame-overlap chopper

The frame overlap chopper has similar dimensions as the pulse chopper, but a open/close time ratio of 50%. Its position is at or close to the intermediate focal point of the *Selene* guide system. The frequencies and phases of pulse- and frame-overlap-choppers can be locked. The frame overlap chopper is the left device in figure 12.1.

12.2.3 Precision slit

The small dimensions of the prototype results in a down-scaling of the sample and thus of the slit at the first focal point. The beam cross-section is of the order $0.1 \times 1\,\mathrm{mm}^2$. This will be realised with a precision x-ray slit system, equipped with BorAl and Cd absorbers. The slit is custom made by ACS and based on their system STT-100-20.

During the experiments on BOA the slit failed several times. In the end it could not be used other than for defining a fix opening of approximately $0.5 \times 1\,\mathrm{mm}^2$.

12.2.4 Double multilayer monochromator

The double multilayer monochromator consists of 2 borcron glass substrates, coated with a Ni/Ti multilayer with a first order peak at $m = 3$ with $\Delta q/q = 7\%$. The surfaces are mounted parallel face to face with a gap of 6.5 mm. The first substrate is 305 mm long, the second 119 mm. In x direction there is a 5 mm gap in between both. The design is optimised for a slit positioned 43 mm behind the end of the device. The acceptance is $\Delta\theta = 1.8°$ for $\lambda \in [4, 10]$ Å.

The device was tested and characterised on Amor. Since the divergence available for this test was only of the order of 0.3°, the full angular range was reached by tilting the monochromator in discrete steps. Figure 12.2 shows the resulting $I(\theta, \lambda)$ map. The width of the intensity streak shown here is limited by the measurement range, not by the device.

To characterise $\Delta\lambda/\lambda$ and the off-specular scattering, measurements were also performed with a well collimated beam (slits of 1 mm opening, 100 mm and 2200 mm from the entrance of the device). The $I(\lambda)$ curves for various θ are shown in figure 12.3.

Figure 12.4 shows the off-specular scattering for $\lambda = 6.3$ Å with various slit positions and openings behind the device. The slits before the ml-monochromator are 1 mm each. Surprisingly there is the same broad diffuse background with an exponential decay for all measurements. The origin most likely is a feature of the detector [→9.2.1].

12.2.5 Sample holder

The sample holder is simply an Al cuboid with grooves and slits to insert (glue) the sample and some absorbing sheets. It is mounted on a y and z translation stage.

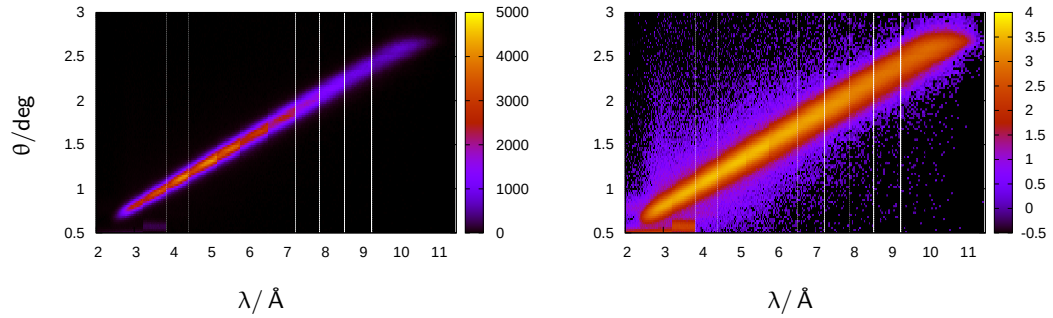

Figure 12.2: $I(\lambda, \theta)$ on linear (left) and logarithmic scale (right) obtained with the ml-monochromator on Amor. The maps are stitched together from 11 measurements since the incoming divergence was limited to 0.3°.

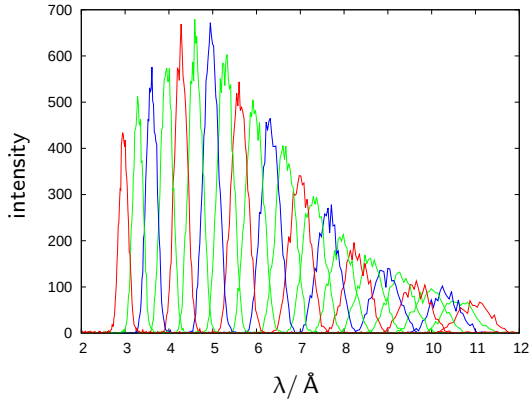

Figure 12.3: $I(\lambda)$ for $\theta = 0.5°, 0.6°, \ldots 3.0°$. The varying height of the individual scans reflects the λ-dependence of the intensity of the incoming beam.

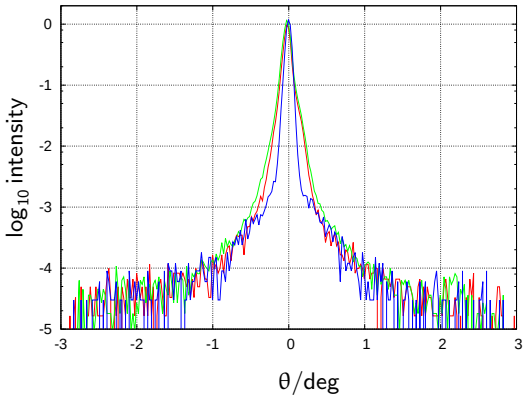

Figure 12.4: $\log_{10}[\, I(\theta)\,]$ without aperture behind the device (green), with a 0.5 mm aperture at 50 mm (red), and with a 1 mm aperture at 1 300 mm (blue).

12.2.6 Guide support

The guide support system is assembled from X95 profiles and joints, motorised and manual translation tables and manual tilting stages. Figure 12.5 shows the mounting frames for the single guide elements (figure 12.7), the height and tilt-adjustments and the X95 bar where upon the guide elements are mounted. This bar is positioned on tilting- and translation stages, which are to be mounted to the lower rotation stages of the BOA tables 3 and 4, respectively.

12.2.7 Guide system

The *Selene* guide system in this case consists of 2 sections focusing elliptically in two dimensions (i.e. in y and in z), where each section consists of 2 mirror-inverted elements of 600 mm length. Figure 12.7 shows one guide element before mounting.

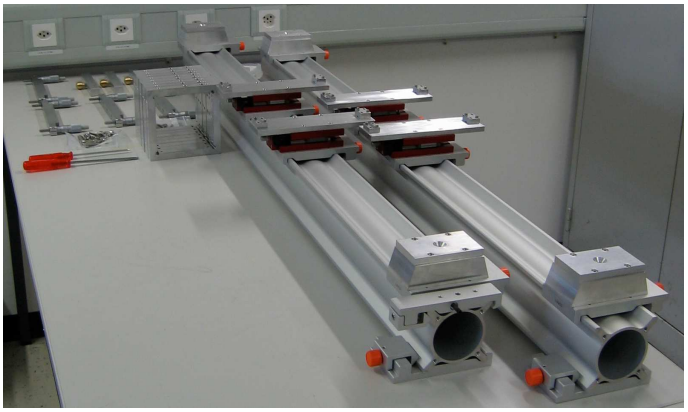

Figure 12.5: Parts of the guide support before mounting the guide elements.

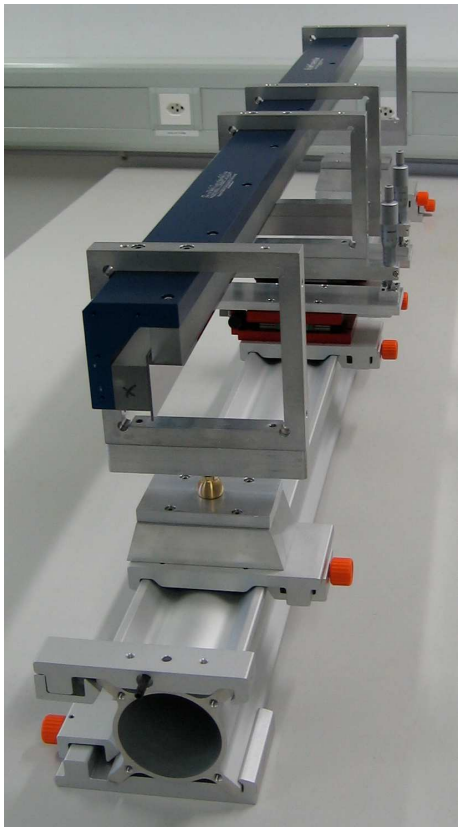

Figure 12.6: Guide support with 2 guide elements mounted. Shown is the second guide of the *Selene* set-up, reflecting left and downwards. The guides are not yet adjusted, the knife blade slit is missing.

Figure 12.7: Single guide element (half a guide section). The blue part is an L-shaped Al bar on which the glass substrates are screwed. The Al frames are for mounting the elements on the support and alignment system.

The device was constructed and build by SwissNeutronics according to the measures

$$
\begin{aligned}
c &= 1000.000\,\text{mm} \\
a &\approx 1000.231\,\text{mm} \\
b &\approx 21.485\,\text{mm} \\
b/a &= 0.021480 \\
\xi &= 0.6 \\
\Delta\theta &= 1.8^\circ \\
\epsilon &= 1.5^\circ
\end{aligned}
$$

The coating is a Ni/Ti supermirror with $m = 4$. The horizontally reflecting glass substrate has a constant height of 46 mm. The vertically reflecting glass has one straight edge along the optical axis, and one elliptically curved edge, fitting the horizontal reflectors shape. The vertical reflector has a minimum width of 21 mm.

12.3 Experiment on Amor

Over the past years several test measurements with the components mentioned above were performed on Amor. With each iteration the data quality got better, the equipment was improved and completed, and a data analysis algorithm was developed and implemented. Finally in November 2013 the prototype *Selene* guide set-up including the polariser [→7.1] and an RF spin-flipper was used successfully by an external user group on Amor. Here the technical aspects, the measurements and the data processing to $R(q_z)$ curves is presented. For details about the sputter chamber or the science case please contact the experimental team: B. Wiedemann, W. Kreuzpaintner, and P. Böni from the Technical University Munich, Germany. The project is entitled *In-situ polarised reflectometry of an Fe-film on Cu, grown by magnetron sputtering* and has the PSI proposal number 20130579.

The challenge for this experiment was to perform polarised neutron reflectometry on a sample mounted inside a sputter chamber. The idea was to characterise the depth profile for the pure substrate, and after each deposition process of nominally one atomic layer of Fe. Figure 12.8 shows a picture of the sputter chamber and part of the associated equipment. The chamber was built very compact with dimensions of $1.6 \times 1 \times 1.5\,\mathrm{m}^3$ ($\mathrm{L} \times \mathrm{B} \times \mathrm{H}$) with a footprint of $1 \times 1\,\mathrm{m}^2$ in the demounted state. Moreover, the sputtering system is fully mobile, so that most of the components are fixed at the chamber or its frame. Deinstallation and installation time is about 5 h, respectively.

For the measurement, the sample table can be translated parallel to the beam (x-direction) as well as vertically to the sample surface (z-direction), and rotated around the horizontal axis (ω) to change the angle of incidence. The sample table is mounted on the left flange with a rotary feedthrough and with x and y stepping motors. Three sputter guns for $2''$ targets are located on top of the chamber. The top flange as well as each gun itself are tilted by 20° to provide the maximum spacing between the guns to prevent cross contamination. The guns are rotatable, so that always one gun is located above the sample. Consequently, one can change the deposition material without breaking the vacuum. Each gun can be operated for DC sputtering or RF sputtering. The total chamber can be lifted for a rough alignment to the neutron beam, while the exact alignment is done by the sample table.

12.3.1 Set-up on Amor

Amor is a neutron reflectometer at SINQ, PSI [36], which allows for a wide range of set-ups The scattering geometry is vertical so that liquid surfaces are accessible. Most components are positioned on an 8 m long optical bench which allows to play with the resolution, or to test exotic set-ups like the prism approach by R. Cubitt [31] or the *Selene* concept. In general Amor is operated in time-of-flight mode (realised by a double chopper), but it is also possible to run it with a monochromator.

The chopper is positioned in a housing, some cm behind the end of the neutron guide. It consists of 2 discs, 490 mm apart, each with 2 openings of 13.6°. In general it is operated in a way to give $\Delta\lambda/\lambda = \text{const.}$[33] For the experiment shown below a pulse frequency of $33.\overline{3}$ Hz (corresponding to $1000\,\mathrm{min}^{-1}$) was used.

The chopper housing limits the maximum incoming divergence because it leads to a minimum distance of 1 500 mm between the end of the guide to the first diaphragm. This diaphragm is defines the virtual source at the first focal point of the *Selene* guide.

For this experiment all standard stages (slits, frame-overlap mirror, polariser, and sample) on the optical bench up to the detector were removed. Instead the *Selene* guide was installed, directly followed by the

Figure 12.8: Photo of the sputtering system with the sputtering chamber in the middle, the gas rack on the left, and the electronic rack and the computer on the right. (Source:[35])

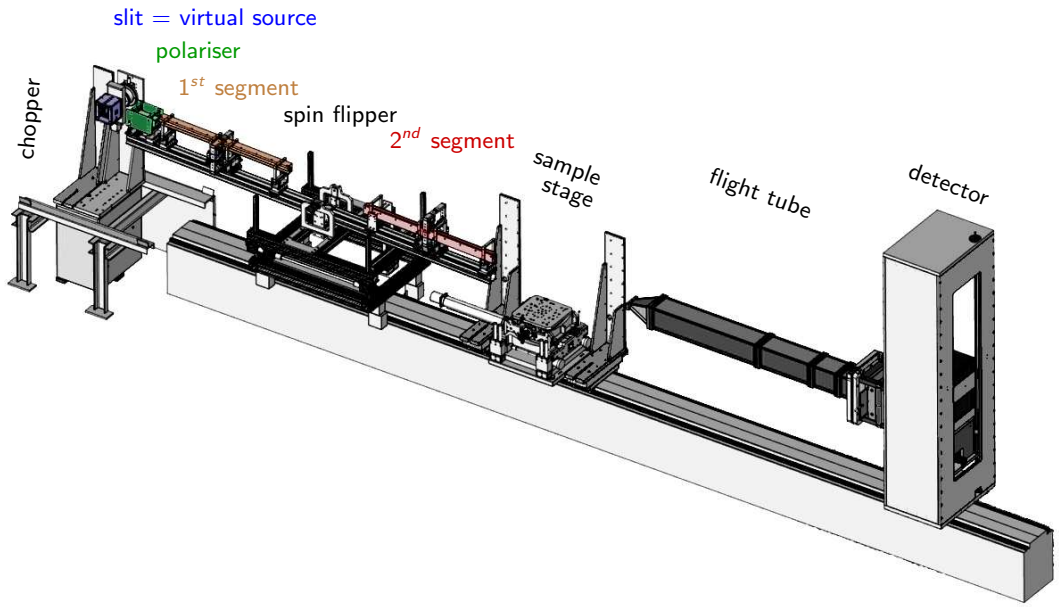

Figure 12.9: Set-up of the *Selene* guide on Amor including the polariser.

sputter chamber and the detector with flight tube. Figure 12.9 shows the set-up without the chamber. On the support for the guide also the polariser and the RF spin flipper are mounted. This support system allows for lifting the guide to the correct height, for a manual horizontal translations, for manual horizontal inclination, and for a motorised tilting. A photo of the complete set up including the sputter chamber is shown in figure 12.10.

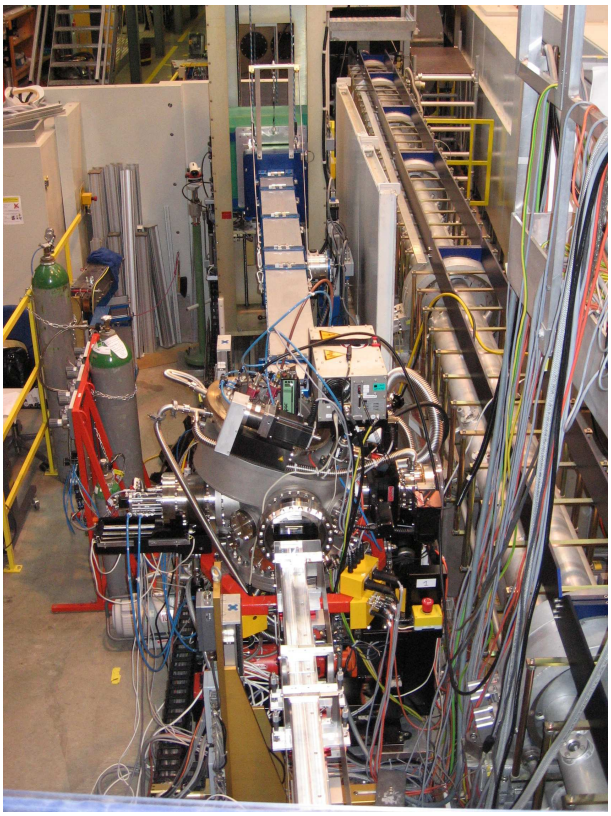

Figure 12.10: Picture of the set-up on Amor taken from atop the chopper housing. The sputter chamber is located in the centre, followed by a flight-tube and the detector (with the green housing at the top). The shiny aluminium beam pointing from the bottom towards the sputtering chamber is the supporting backbone of the (second part of the) Selene guide. The infrastructure for the sputter chamber (electronic racks, control computer and cooling) are located on the gallery above the instrument, visible on the right.

12.3.2 Measurements in the high-intensity specular reflectometry mode

The measurement time for one reflectivity curve had to be *as short as possible* essentially because of possible oxidation of the film in between two sputter processes. Also the huge number of measurements (both spin states for the pure silicon substrate, the same with the Cu layer, and after each deposition of nominally one atomic layer of Fe) demands for a short counting time. Thus the high-intensity specular reflectivity mode [→10.4] has been chosen.

In a first measurement series each set of measurements, i.e. both spin states, two sample orientations, took 5 h. This is already much faster than the previous measurements on REFSANS at MLZ, but it was not clear if the film is still clean after this time. Thus in a second measurement the counting time was reduced to 10 min per spin state and only one sample orientation. For technical reasons the sputter process required also some 10 min (Each sputter process required the reorientation of the sample, a movement of the sputter target and

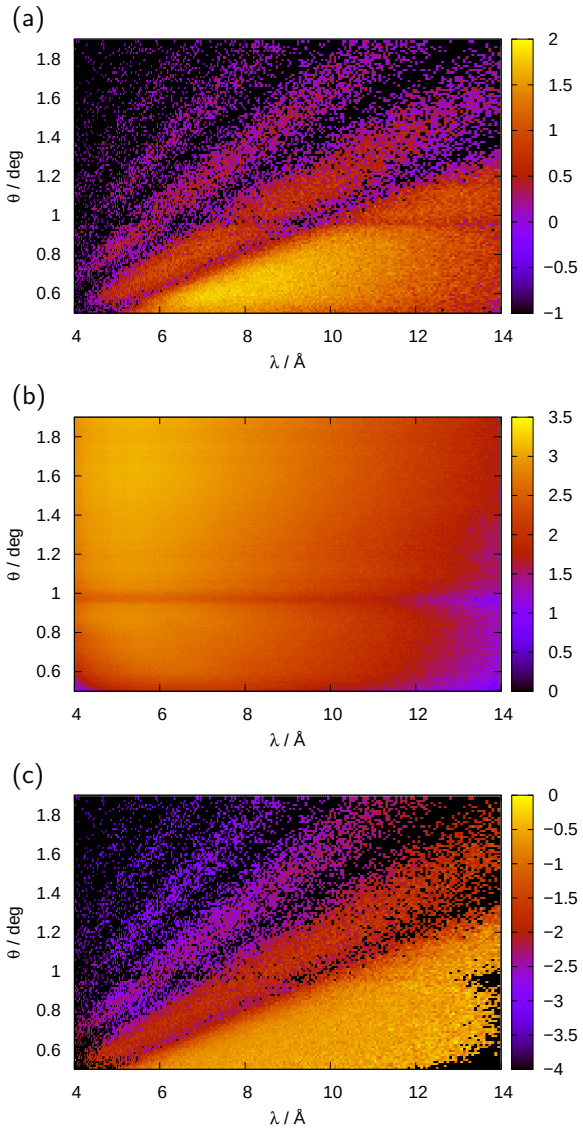

Figure 12.11: Intensity maps $\log_{10} I(\lambda, \theta)$ obtained for the sample prior to the Fe deposition (a) and for a supermirror with $m = 5$ (b). The latter was used for normalisation to obtain $R(\lambda, \theta)$ (c).

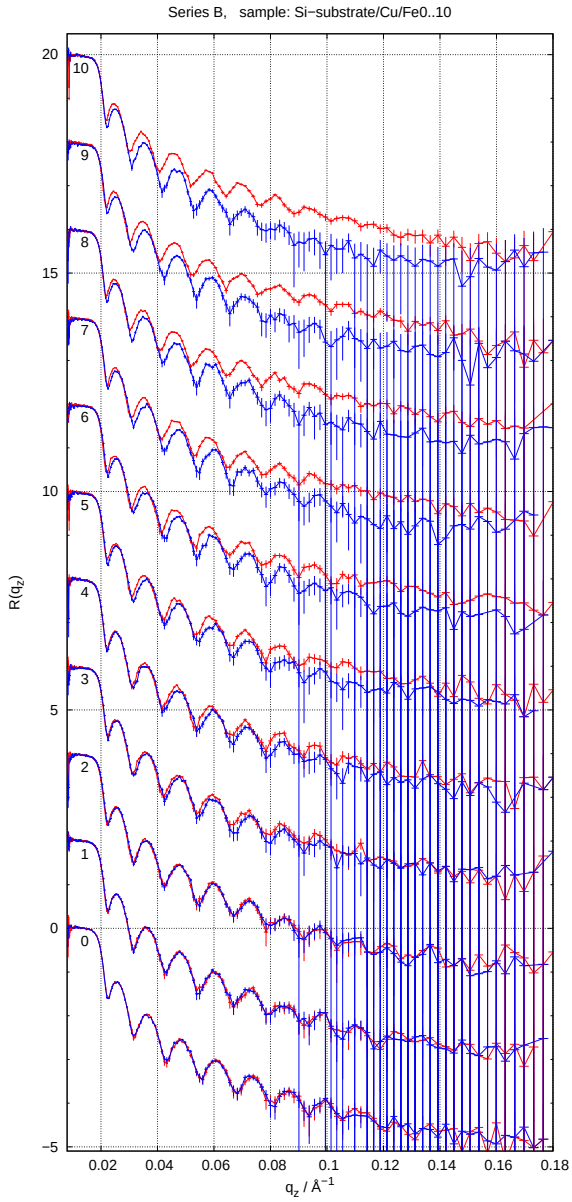

Figure 12.12: Reflectivity curves $\log_{10} R(q_z)$ for spin up (red) and spin down (blue) for the Cu-film on silicon without Fe (0) and with growing Fe-layer, where the index n gives the nominal number of atomic layers. For clarity the curves are scaled by 10^{2n}.

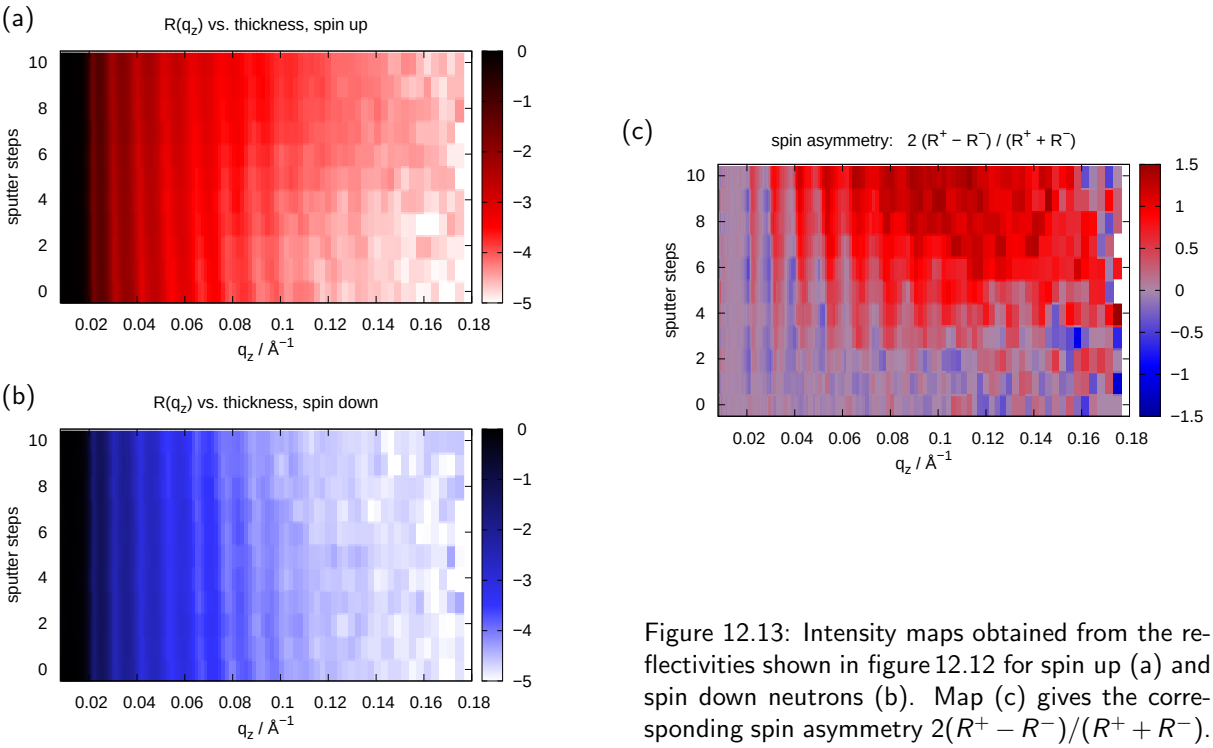

Figure 12.13: Intensity maps obtained from the reflectivities shown in figure 12.12 for spin up (a) and spin down neutrons (b). Map (c) gives the corresponding spin asymmetry $2(R^+ - R^-)/(R^+ + R^-)$.

a pre-sputter time. The actual deposition time was 2 s, only.) Thus shorter counting times would not have reduced the problem of oxidation.

In the following the full *long* measurements are presented, followed by one example of a fast measurement.

Figure 12.11 shows the $I(\lambda, \theta)$-maps for the sample prior to the Fe deposition (a) and for the reference, a $m = 5$ supermirror (b). The map (c) was obtained from (a) and (b) by pixel-wise division (with a low-statistics threshold of 20 counts in the reference). Each pixel can be assigned to $q_z = 4\pi \sin\theta/\lambda$. The map is converted into a reflectivity curve by filling all pixels in a q_z-grid with $\Delta q_z/q_z = \text{const}$. Figure 12.12 shows the reflectivities obtained this way for both spin states and all Fe-layer thicknesses. After each set of measurement (both spin-states and two sample orientations $\omega = 1.1°$ and $2.6°$) a growth-step of the Fe-layer of nominally one atomic layer was performed. Each set of measurements took about 5 h counting time.

To get a qualitative picture of the evolution of the magnetic induction with Fe thickness, the reflectivity curves were plotted as colour maps with R versus q_z and nominal Fe-layer thickness. The resulting maps are shown in figure 12.13 together with the spin asymmetry $2(R^+ - R^-)/(R^+ + R^-)$.

One can see the shift of the Kiessig fringes towards lower q_z for increasing Fe-layer thickness in maps (a) and (b). In addition there is an increase / decrease of intensity at $q_z \approx 0.12$ for spin up / down for more than 6 layers. The spin asymmetry reveals more details: no magnetic effect is visible for up to 2 layers of Fe. Then a spin asymmetry sets in resulting in an increase of the spin-up signal and a shift of the peaks relative to spin down. This *phase shift* of the Kiessig fringes results in the narrow stripe-pattern for more than 2 Fe-layers. The Bragg-peak associated to the magnetic Fe-layer can be seen as a split of the two reflectivity curves rather than a shift. This splitting increases, and its maximum also moves to smaller q_z.

A second set of measurements with reduced counting times (20 min per layer) was performed to check whether the film degraded during the rather long intervals between two deposition processes. One example for 6 Fe layers is shown in figure 12.14. It looks like there is no degradation, but a detailed analysis of the data has not yet been performed.

12.3.3 Discussion

Though initially designed to demonstrate and verify the performance of the *Selene* guide, the prototype proved to be a very useful add-on for Amor. The presented example illustrates this: the geometrical constraints of the sputter chamber make it difficult to install diaphragms close to the sample. The truly focused beam does not

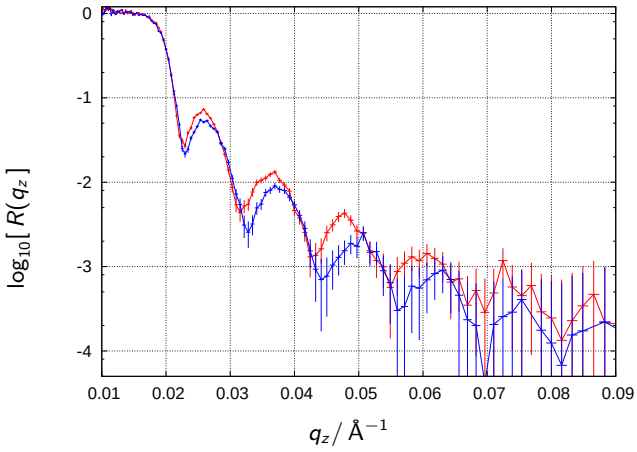

Figure 12.14: $\log_{10}[R(q_z)]$ for spin up (red) and spin down (blue) neutrons, measured on the sample Si/Cu/Fe(6 layers) within 10 min, each.

need such an aperture and thus opens more flexibility in designing the sputter chamber. The reduction of the time in between two deposition steps to less than half an hour is only possible by using the *new* high-intensity mode.

Being only a demonstration unit, the *Selene* prototype guide has rather small dimensions. This allows for its operation on Amor (and other existing instruments), but it dramatically reduces the maximum footprint. In the presented case the sample had a surface area of $20 \times 20\,\text{mm}^2$, where only a stripe of $2 \times 20\,\text{mm}^2$ was illuminated. A full-scale guide would result in a 10 mm wide footprint and thus give a gain-factor 5.

Another factor 5 would be gained in this case by making the existing bent straight guide of Amor obsolete, because that has a rather low transmittance of only some 20% (measured with gold foil activation).

Also the complete *Selene* guide was in air, which lead to the reduction of the beam incident on the sample of 40% (the flight-path behind the sample was filled with Ar).

The *Selene* guide leads to a horizontal parallel offset of the beam of 106 mm. At the time the measurements were performed, the detector could not be shifted horizontally, so the guide had to be inclined and thus accepted only half or less of the beam divergence.

Considering these losses, a full scale *Selene* guide for Amor (with moderator and sample as initial and final focal points) would allow to reduce the counting time for the presented experiment by about 2 orders of magnitude! I.e. both curves shown in figure 12.14 can be collected in 12 s.

The expected gain on *Estia* is almost another two orders of magnitude due to the much higher brilliance of the ESS source compared to SINQ. Figure 12.14 could be obtained with 2 to 3 pulses. Thus it would be possible to measure really *in-situ* during the continuous deposition process.

outlook The *Selene* prototype will be further improved and used in the future as an add-on on Amor. Besides this it is available for the neutron scattering community for tests, either on Amor or BOA, or at other institutes. The improvements are:

- modification of the aluminium backbone to allow for an individual alignment of the two mirrors forming one building block of 600 mm length;
- addition of a precision slit to allow for exact 3-dimensional footprint definition (operational 4. 2014);
- design/construction of some housing enabling an Ar atmosphere along the beam path to avoid attenuation by air scattering;
- modification of the optical bench of Amor to enable a horizontal movement of the detector (operational 4. 2014). This is necessary to compensate for the horizontal beam off-set of 106 mm by the *Selene* guide. This measure increases the accepted (and transmitted) divergence and thus the intensity at the sample.

References

[1] J. Stahn, U. Filges, and T. Panzner. Focusing specular neutron reflectometry for small samples. *The European Physical Journal Applied Physics*, 58, 4 2012.

[2] Phillip M. Bentley, Shane J. Kennedy, Ken H. Andersen, Damian Martin Rodriguez, and David F. R. Mildner. Correction of optical aberrations in elliptic neutron guides. *N.I.M. A*, 693:268–275, 2012.

[3] L. D. Cussen, D. Nekrassov, C. Zendler, and K. Lieutenant. Multiple reflections in elliptic neutron guide tubes. *Nuclear Instruments & Methods in Physics Research Section A-Accelerators Spectrometers Detectors and Associated Equipment*, 705:121–131, MAR 21 2013.

[4] D. Pantel, S. Goetze, D. Hesse, and M. Alexe. Reversible electrical switching of spin polarization in multiferroic tunnel junctions. *Nature Materials*, 11:289293, 2012.

[5] Sang-Wook Cheong and Maxim Mostovoy. Multiferroics: a magnetic twist for ferroelectricity. *Nature Materials*, 6(1):13–20, JAN 2007.

[6] R. Ramesh and Nicola A. Spaldin. Multiferroics: progress and prospects in thin films. *Nature Materials*, 6(1):21–29, JAN 2007.

[7] J. Hoppler, J. Stahn, Ch. Niedermayer, V. K. Malik, H. Bouyanfif, A. J. Drew, M. Roessle, A. Buzdin, G. Cristiani, H. U. Habermeier, B. Keimer, and C. Bernhard. Giant superconductivity-induced modulation of the ferromagnetic magnetization in a cuprate-manganite superlattice. *Nature Materials*, 8(4):315–319, APR 2009.

[8] B. J. Kirby, D. Kan, A. Luykx, M. Murakami, D. Kundaliya, and I. Takeuchi. Anomalous ferromagnetism in $TbMnO_3$ thin films. *Journal of Applied Physics*, 105(7), APR 1 2009. 53rd Annual Conference on Magnetism and Magnetic Materials, Austin, TX, NOV 11-14, 2008.

[9] J. S. White, M. Bator, Y. Hu, H. Luetkens, J. Stahn, S. Capelli, S. Das, M. Döbeli, Th. Lippert, V. K. Malik, J. Martynczuk, A. Wokaun, M. Kenzelmann, Ch. Niedermayer, and C. W. Schneider. Strain-induced ferromagnetism in antiferromagnetic $lumno_3$ thin films. *Phys. Rev. Lett.*, 111:037201, Jul 2013.

[10] H Schmidt, M Gupta, and M Bruns. Nitrogen diffusion in amorphous silicon nitride isotope multilayers probed by neutron reflectometry. *Physical Review Letters*, 96(5), FEB 10 2006.

[11] H. Schmidt, U. Geckle, and M. Bruns. Simultaneous diffusion of Si and N in silicon nitride. *Physical Review B*, 74(4), JUL 2006.

[12] E. Hueger, H. Schmidt, J. Stahn, B. Braunschweig, U. Geckle, M. Bruns, and A. Markwitz. Atomic transport in metastable compounds: Case study of self-diffusion in Si-C-N films using neutron reflectometry. *Physical Review B*, 80(22), DEC 2009.

[13] Sujoy Chakravarty, Harald Schmidt, Ursula Tietze, Dieter Lott, N. P. Lalla, and Ajay Gupta. Self-diffusion and defect annihilation in nanocrystalline Fe films probed by neutron reflectometry. *Physical Review B*, 80(1), JUL 2009.

[14] E. Hueger, U. Tietze, D. Lott, H. Bracht, D. Bougeard, E. E. Haller, and H. Schmidt. Self-diffusion in germanium isotope multilayers at low temperatures. *Applied Physics Letters*, 93(16), OCT 20 2008.

[15] E. Hueger, J. Rahn, J. Stahn, T. Geue, and H. Schmidt. Diffusivity determination in bulk materials on nanometric length scales using neutron reflectometry. *Physical Review B*, 85(21), JUN 4 2012.

[16] Erwin Hueger, Lars Doerrer, Johanna Rahn, Tobias Panzner, Jochen Stahn, Gerhard Lilienkamp, and Harald Schmidt. Lithium Transport through Nanosized Amorphous Silicon Layers. *Nano Letters*, 13(3):1237–1244, MAR 2013.

[17] A Ohtomo, DA Muller, JL Grazul, and HY Hwang. Artificial charge-modulation in atomic-scale perovskite titanate superlattices. *Nature*, 419(6905):378–380, SEP 26 2002.

[18] A Ohtomo and HY Hwang. A high-mobility electron gas at the $LaAlO_3/SrTiO_3$ heterointerface. *Nature*, 427(6973):423–426, JAN 29 2004.

[19] J. Mannhart, D. H. A. Blank, H. Y. Hwang, A. J. Millis, and J. M. Triscone. Two-Dimensional Electron Gases at Oxide Interfaces. *MRS Bulletin*, 33(11):1027–1034, NOV 2008.

[20] Pavlo Zubko, Stefano Gariglio, Marc Gabay, Philippe Ghosez, and Jean-Marc Triscone. Interface Physics in Complex Oxide Heterostructures. In Langer, JS, editor, *Annual Review of Condensed Matter Physics, VOL 2*, volume 2 of *Annual Review of Condensed Matter Physics*, pages 141–165. 2011.

[21] Marta Gibert, Pavlo Zubko, Raoul Scherwitzl, Jorge Iniguez, and Jean-Marc Triscone. Exchange bias in $LaNiO_3$-$LaMnO_3$ superlattices. *Nature Materials*, 11(3):195–198, MAR 2012.

[22] C. F. Majkrzak and N. F. Berk. Phase sensitive reflectometry and the unambiguous determination of scattering length density profiles. *Physica B*, 336:27–38, 2003.

[23] M. Montel. X-ray microscopy with catamegonic roof mirrors. *X-ray microscopy and microradiography*, pages 177–185, 1957.

[24] M. Russina, F. Mezei, and G. Kali. First Implementation of Novel Multiplexing Techniques for Advanced Instruments at Pulsed Neutron Sources. In *5th European Conference on Neutron Scattering*, volume 340 of *Journal of Physics Conference Series*, Dirac House, Temple Back, Bristol BS1 6BE, England, 2012. European Nucl Scattering Assoc, IOP Publishing Ltd. 5th European Conference on Neutron Scattering (ECNS), Prague, Czech Republic, JUL 17-21, 2011.

[25] R. Georgii, G. Brandl, N. Arend, W. Haeussler, A. Tischendorf, C. Pfleiderer, P. Boeni, and J. Lal. Turnkey module for neutron scattering with sub-micro-ev resolution. *Applied Physics Letters*, 98:073505, 2011.

[26] P.O. Astrand, K. Lefmann, E. Farhi, and et al. New features in mcstas, version 1.5. *Applied Physics A*, 74:S1511–S1513, 2002.

[27] K. Lefmann and K. Nielsen. Mcstas, a general software package for neutron ray-tracing simulations. *Neutro News*, 10:20, 1999.

[28] Frédéric Ott and Alain Menelle. Refocus: A new concept for a very high flux neutron reflectometer. *Nuclear Instruments and Methods in Physics Research A*, 586(1):23 – 30, 2008. Proceedings of the European Workshop on Neutron Optics - NOP '07.

[29] F. Ott and A. Menelle. New designs for high intensity specular neutron reflectometers. *European Physical Journal - Special Topics*, 167:93–99, 2009.

[30] M. Schneider, J. Stahn, and P. Böni. Focusing of cold neutrons: Performance of a laterally graded and parabolically bent multilayer. *Nuclear Instruments and Methods in Physics Research Section A: Accelerators, Spectrometers, Detectors and Associated Equipment*, 610(2):530 – 533, 2009.

[31] R. Cubitt. *N.I.M. A*, 558:547–550, 2006.

[32] R. Cubitt and J. Stahn. Neutron reflectometry by refractive encoding. *Eur. Phys. J. Plus*, 126:111, 2011.

[33] A.A. van Well. Double-disk chopper for neutron time-of-flight experiments. *Physica B: Condensed Matter*, 180-181(2):959 – 961, 1992.

[34] P. Mikulík. *EDXR — X-ray and neutron reflectivity calculation program*. mikulik@physics.muni.cz, 2001.

[35] Thomas Mairoser. *In-Situ Neutronen-Reflektometrie und Untersuchungen von EuO-Filmen*. PhD thesis, Universitt Augsburg, Lehrstuhl fr Experimentalphysik VI, Augsburg, Germany, 2013.

[36] M. Gupta, T. Gutberlet, J. Stahn, P. Keller, and D. Clemens. Amor - the time-of-flight neutron reflectometer at SINQ/PSI. *Pramana-Journal of Physics*, 63:57–63, 2004.